Experimental and Computational Studies on the Design of Dyes for Water-splitting Dye-sensitized Photoelectrochemical Tandem Cells

by

Dalvin D. Méndez-Hernández

A Dissertation Presented in Partial Fulfillment
of the Requirements for the Degree
Doctor of Philosophy

Approved April 2014 by the
Graduate Supervisory Committee:

Ana L. Moore, Co-Chair
Vladimiro Mujica, Co-Chair
Devens J. Gust
Ian Gould

ARIZONA STATE UNIVERSITY

May 2014

ABSTRACT

Solar energy is a promising alternative for addressing the world's current and future energy requirements in a sustainable way. Because solar irradiation is intermittent, it is necessary to store this energy in the form of a fuel so it can be used when required. The light-driven splitting of water into oxygen and hydrogen (a useful chemical fuel) is a fascinating theoretical and experimental challenge that is worth pursuing because the advance of the knowledge that it implies and the availability of water and sunlight. Inspired by natural photosynthesis and building on previous work from our laboratory, this dissertation focuses on the development of water-splitting dye-sensitized photoelectrochemical tandem cells (WSDSPETCs). The design, synthesis, and characterization of high-potential porphyrins and metal-free phthalocyanines with phosphonic anchoring groups are reported. Photocurrents measured for WSDSPETCs made with some of these dyes co-adsorbed with molecular or colloidal catalysts on TiO_2 electrodes are reported as well.

To guide in the design of new molecules we have used computational quantum chemistry extensively. Linear correlations between calculated frontier molecular orbital energies and redox potentials were built and tested at multiple levels of theory (from semi-empirical methods to density functional theory). Strong correlations (with r^2 values > 0.99) with very good predictive abilities (rmsd < 50 mV) were found when using density functional theory (DFT) combined with a continuum solvent model. DFT was also used to aid in the elucidation of the mechanism of the thermal relaxation observed for the charge-separated state of a molecular triad that mimics the photo-induced proton coupled electron transfer of the tyrosine-histidine redox relay in the reaction center of

Photosystem II. It was found that the inclusion of explicit solvent molecules, hydrogen bonded to specific sites within the molecular triad, was essential to explain the observed thermal relaxation. These results are relevant for both advancing the knowledge about natural photosynthesis and for the future design of new molecules for WSDSPETCs.

DEDICATION

This dissertation is dedicated to Limari, Daniela and Oriol. Thank you for all your love.

ACKNOWLEDGMENTS

To my advisors, Professors Ana Moore, Vladimiro Mujica, Tom Moore and Devens Gust for your guidance, support and kindness. Thank you for making this learning experience enjoyable and productive.

To Dr. Jackson Megiatto, Dr. Pilarisetty Tarakeshwar, Dr. Gerdenis Kodis, Dr. Anne-Lucie Teillout, Dr. Manuel J. Llansola-Portoles, Dr. Paul Liddell, Dr. Yuichi Terozano, Dr. Smitha Pillai, Dr. Catia Ornelas, Dr. Graeme Copley, Dr. Matthieu Koepf, Dr. Julio Palma, Dr. Daniel Finkelstein-Shapiro, and Dr. Maxime Fournier for being great scientists and role models. I learn a lot from each of you.

To my peers, John Tomlin, Jaro Arero, Katie WongCarter and Antaeres' Antoniuk-Pablant for all the time spent since the beginning of this journey. Thank you for everything that you taught me and for all the times that we shared and that you made me laugh.

To my senior graduate students, Dr. Bradley Brennan, Dr. Benjamin Sherman, Dr. Jesse Bergkamp, Michael Vaughn, Dr. Brian Watson, Dustin Patterson, Dr. Chris Madden and Jim Bridgewater, to my junior graduate students, Marely Estefania, Chelsea Brown, Ian Pahk, Bobby Schmitz, Shobeir Seddigh, Reza Vatan, Micah Wimmer, Daniel Meritz, Angelo Di Bernardo, Luis Gonzalez and visiting graduate students Amir Kaplan, Nico Kaeffer and Nino Arrigo. Thanks for sharing your knowledge, optimism and passion for research.

To our collaborators Dr. Jason Gillmore, Dr. Tijana Rahj, Dr. Oleg Poluektov, Laura Hernández, Robert Godin, Dr. Rodrigo Palacios, Dr. Ernesto Mariño, and Dr.

Gonzalo Cosa, John Swierk, Nicholas McCool, Nella Vargas-Barbosa and Dr. Tom Mallouk. Thanks for constructive collaborations and invaluable feedback.

To Luis Montano, Monica Trejo, Francisco Flores and Ramon Bocanegra. Thanks for helping me become me a better teacher.

To my undergraduate advisors and professors, Dr. Juan Arratia, Dr. Lymari Fuentes-Claudio, Dr. Daniel Bacelo, Dr. Gladys Bonilla, Dr. Melanie Cooper and Dr. Antek Wong-Foy and Dr. Adam Matzger. Thanks for inspiring me to get a Ph.D.

To my parents, Wilma and Daniel for being great parents and role models and to my friends Emmanuel, Maytee, Angel, Arlene, Jose, Odalys. Thanks for all the good times.

Thanks to the National Science Foundation and the Department of Energy for their financial support.

TABLE OF CONTENTS

Page

LIST OF TABLES

LIST OF FIGURES

Figure Page

CHAPTER 1

INTRODUCTION

Making fuels from sunlight and water is an old human desire, as it will greatly benefit humanity[1-10]. Many artificial photosynthetic cells have been reported[9,11-22], but achieving a system that is scalable, efficient and robust is still a big challenge[23-28].

Water-splitting dyes-sensitized photoanodes (WSDSPAs), where a dye and a catalyst are co-adsorbed on the surface of a semiconductor, have been recently demonstrated to work when supplied with an small external bias[15-17,19,20,29,30] and are considered to be a possible practical approach in the conversion of solar energy to chemical energy[24,29,31]. Water-splitting dye-sensitize photoelectrochemical tandem cells (WSDSPETCs) can be made by connecting blue-absorbing WSDSPAs and red-absorbing dye-sensitized solar cells (DSSCs) in series to a proton reduction catalyst (Figure 1). The DSSC provides the extra bias required by the WSDSPAs for the reduction of protons to hydrogen gas (an useful chemical fuel).

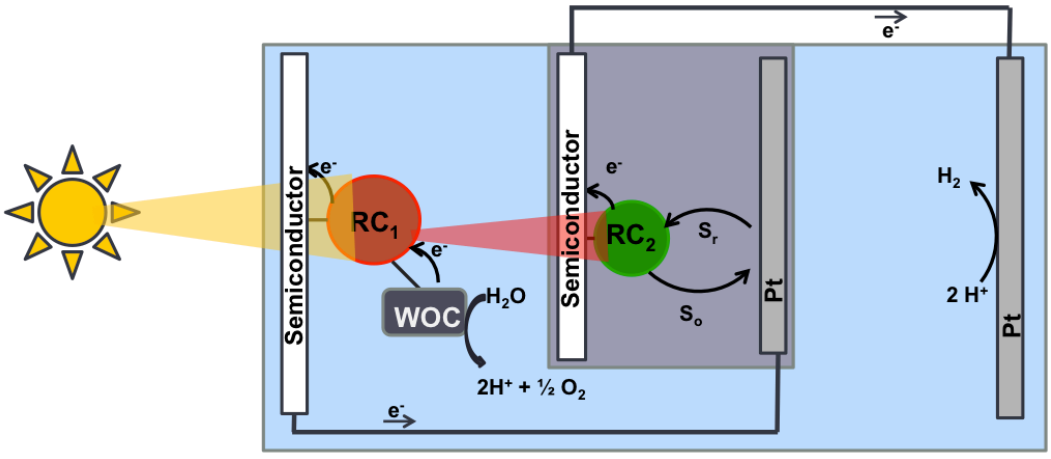

Figure 1. Scheme of the components of the WSDSPETCs used in this project. RC = Reaction Center; WOC = Water Oxidation Catalyst; S_r = reduced redox mediator, and S_o

= oxidized redox mediator. TiO_2 nanoparticles were used as the semiconductor and platinum was used as a catalyst for reduction of H^+ to H_2.

The synthesis and characterization of high-potential porphyrins for WSDSPAs and red-absorbing dyes for DSSCs are described in Chapter 2. The performance of DSSCs made with two of the red absorbing dyes is reported as well.

Photocurrents obtained for WSDSPETCs made with different combinations of dyes and catalysts are reported in Chapter 3. WSDSPETCs containing a bio-inspired redox relay that mimics the tyrosine-histidine pairs of Photosystem II were shown to produce photocurrents without the need of an applied external bias. WSDSPETCs were demonstrated to work although WSDSPAs were found to limit the cells' efficiencies.

In Chapter 4, with the intention of using computational chemistry to aid in the design of new dyes for WSDSPETCs, tools for the design of molecules capable of charge transfer are developed and tested. Correlations between frontier molecular orbital energies and redox potentials[32,33] were explored as an alternative the use of the Born-Haber thermodynamic cycle[34,35] for the estimation of redox potentials. The correlation's dependence on the presence of a continuum-based solvent model and the level of theory of the calculations was explored. A large variety of molecules were investigated and the best resulting correlations were tested with a series of molecules with known reduction potentials.

Lastly, the thermal relaxation observed by high-frequency electron-paramagnetic resonance for the charge-separated state of a triad that mimics the proton coupled electron transfer process of the histidine-tyrosine redox relay in the reaction center of

Photosystem II (PS-II) was investigated[36]. This thermal relaxation was previously observed by Faller *et al.* in 2003[37] for a PS-II depleted of its oxygen-evolving complex and have not been replicated in artificial system before. Computational chemistry was used to help elucidate the relaxation mechanism and the results are discussed in Chapter 5. A mechanism that was not considered by Faller *et al.* and that is consistent with the current crystallographic information of PS-II[38] since it involves explicit solvent molecules hydrogen bonded to the proton donor and acceptor sites is suggested.

CHAPTER 2

SYNTHESIS AND CHARACTERIZATION OF DYES

Porphyrins and phthalocyanines are attractive compounds for WSDSPECTCs because it is possible to adjust their redox and spectroscopic properties with relative ease, allowing access to the potentials required to drive the corresponding catalysts for the oxidation of water and the reduction of protons to hydrogen gas. Also, because of the ability to delocalize the positive charge upon oxidation, porphyrins are less susceptible to nucleophilic attack by water molecules than the ruthenium dyes previously used, which upon oxidation localize the charge on the ruthenium atom changing its oxidation state from Ru(II) to Ru(III)[15].

The normalized absorption spectra of two examples of the tetrapyrolic dyes made in this dissertation are shown in Figure 2. In general, the porphyrins (blue line) have the highest absorption at 420 nm and can absorb up to 650 nm. The phthalocyanines and naphthalocyanine-phthalocyanine hybrids reported herein have the highest absorption at wavelengths above 650 nm and can absorb up to 900 nm. Thus these dyes have complementary absorption profiles. This is important for tandem devices because the component that can absorb the lower energy photons can perform well behind the component that absorb the higher energy photons, thus minimizing the surface area required.

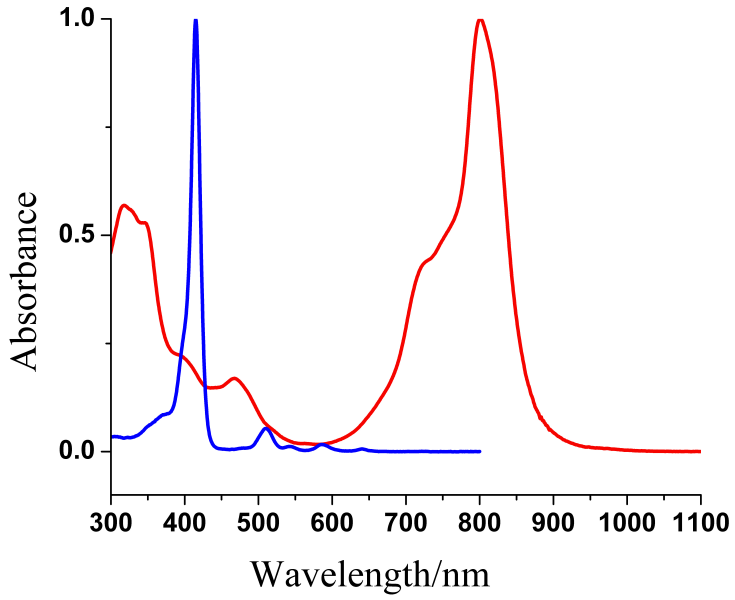

Figure 2. Normalized UV-Vis absorption spectra of compounds **1** and **6** in dichloromethane. Blue curve corresponds to **1**; maximum absorbance at 415 nm and Q-bands at 509, 541, 585, and 641 nm. Red curve corresponds to **6**; maximum absorbance at 815 nm.

A series of high-potential porphyrins capable of driving the oxidation of water by a catalyst and containing anchoring groups capable of binding to metal oxides were designed and synthesized. The synthetic procedures and characterization of these compounds are presented in Chapter 2.1. A series of red to near-infrared absorbing phthalocyanine derivates containing phosphonic acid anchoring groups directly attached to the dye macrocycle were design and synthesized. The synthetic procedures and characterization of these compounds are presented in Chapter 2.2.

2.1 Synthesis of high-potential porphyrins

The structures of the high-potential porphyrins made are shown in Figure 3. The main feature of these porphyrins is that they have very positive oxidation potential (1.26 V vs. SCE; Table 1). This is due to the electron withdrawing ability of the pentafluorophenyl groups. The porphyrins also have an anchoring group (phosphonic or carboxylic) for attachemnet to semi-conductor. A general scheme for the synthesis of porphyrins **1-3** is shown in Figure 4. A general scheme for the synthesis of porphyrins **4** and **5** is shown in Figure 5.

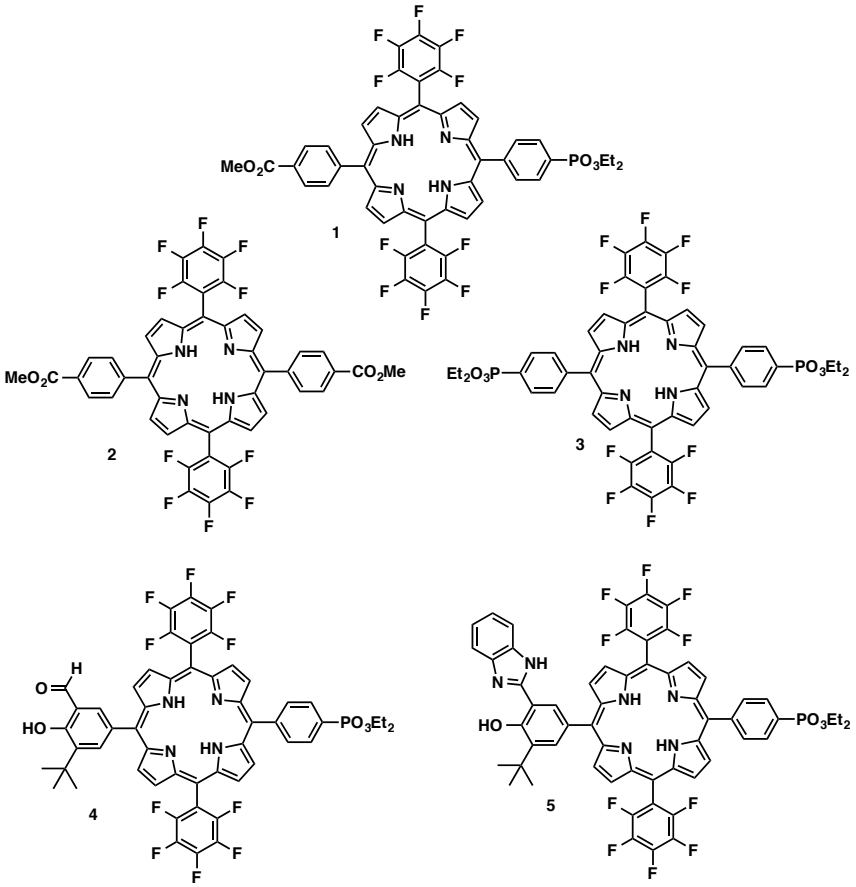

Figure 3. Structures of the high-potential porphyrins synthesized.

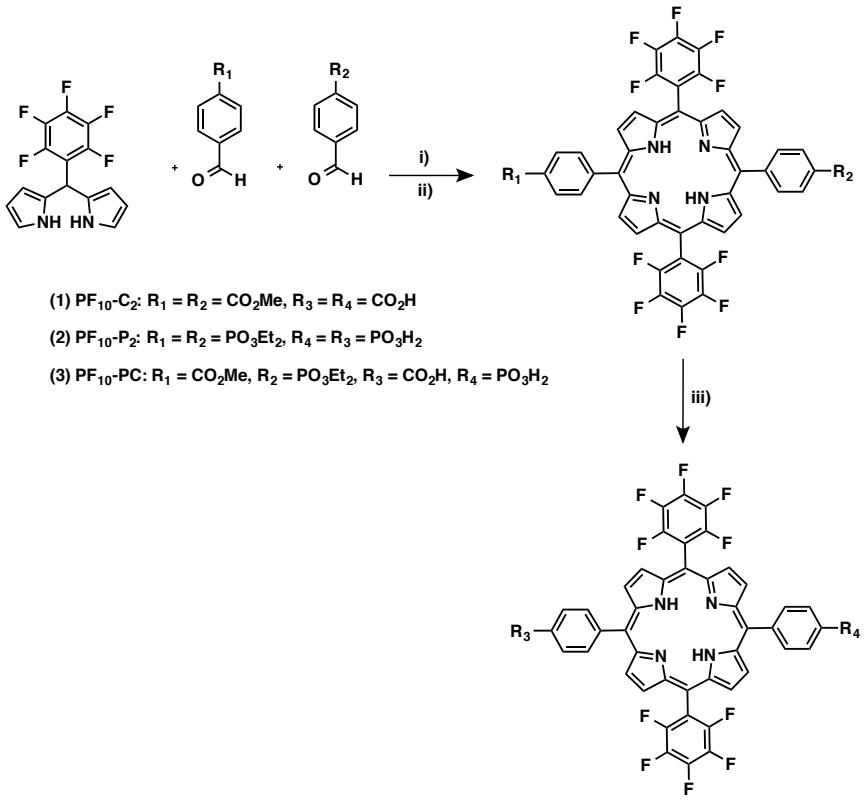

Figure 4. Synthetic scheme for high-potential porphyrins **1-3** and the corresponding acid derivates. i) trifluoroacetic acid in chloroform, 1 h, ii) 2,3-dichloro-5,6-dicyanobenzoquinone (DDQ), RT, overnight, iii) $Si(CH_3)_3Br$ in dichloromethane, RT, overnight or conc. HCl/TFA (2:1), reflux, 48 h.

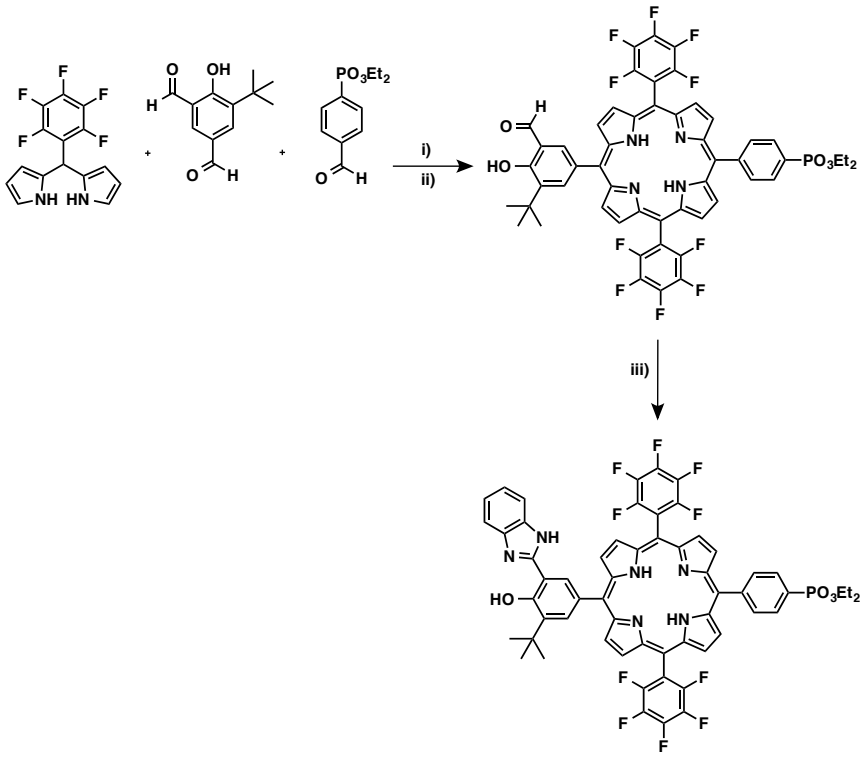

Figure 5. Synthetic scheme for high-potential porphyrins **4** and **5**. i) trifluoroacetic acid in dry chloroform under argon for 1 h, ii) 2,3-dichloro-5,6-dicyanobenzoquinone (DDQ), RT, overnight, iii) *o*-phenylenediamine, reflux in nitrobenzene overnight.

Experimental details and characterization:

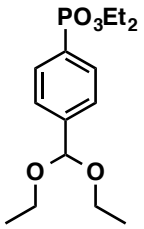

4-(Diethoxyphosphoryl)benzaldehyde diethyl acetal: Following a procedure form the literature[39], a portion of 2.85 g of 4-bromobezaldehyde diethyl acetal, 1.86 g of diethylphosphite, and 530 mg of tetrakis-(triphenylphosphine)Pd(0) were dissolved in 5 mL of a dry toluene/trietylamine (1:1) mixture. The mixture was heated at 80 ºC for 20 h.

A white precipitate was formed. The reaction was filtered, washed with ethyl acetate, filtered and solvent was removed under reduced pressure. The crude was purified by column chromatography with a gradient of ethylacetate/hexanes (20:80) to methanol/ethylacetate (2:98). After removing the solvent under reduced pressure and drying in a desiccator under reduced pressure 0.98 g (29 % yield) of a clear oil was obtained. ^{1}H NMR (400 MHz, CDCl3, δ ppm): 7.81 (m, 2H, ArH); 7.58 (m, 2H, ArH); 5.53 (s, 1H, -CH); 4.12 (m, 4H, -C<u>H</u>$_2$-CH$_3$); 3.58 (m, 4H, -C<u>H</u>$_2$-CH$_3$); 1.32 (t, J = 8.0 Hz, 6H, -CH$_2$-C<u>H</u>$_3$); 1.25 (t, J = 8.0 Hz, 6H, -CH$_2$-C<u>H</u>$_3$).

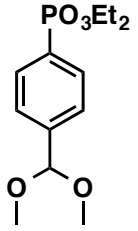

4-(Diethoxyphosphoryl)benzaldehyde dimethyl acetal: Following a procedure form the literature[39], a portion of 5.00 g of 4-bromobezaldehyde dimethyl acetal, 4.25 g of diethylphosphite, and 1.3 g of tetrakis-(triphenylphosphine)Pd(0) were dissolved in 10 mL of a dry toluene/trietylamine (1:1) mixture. The mixture mas heated at 80 ºC for 20 h. A white precipitate was formed. The reaction was filtered, washed with ethyl acetate, filtered and the solvent was removed under reduced pressure. The crude was distilled under reduced pressure and 4.56 g (73 % yield) of a clear oil was obtained. ^{1}H NMR (400 MHz, CDCl$_3$, δ ppm): 7.77 (m, 2H, ArH); 7.50 (m, 2H, ArH); 5.36 (s, 1H, -CH); 4.05 (m, 4H, -O-C<u>H</u>$_2$-CH$_3$); 3.27 (s, 6H, -O-CH$_3$); 1.26 (t, J = 8.0 Hz, 6H, -O-CH$_2$-C<u>H</u>$_3$).

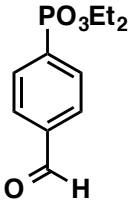

4-(Diethoxyphosphoryl)benzaldehyde: A portion of a solution of 4-(diethoxyphosphoryl)benzaldehyde dimethyl acetal (1.00 g) in dichloromethane (30 mL) and 6M hydrochloric acid (50 mL) left stirring for 1 h at room temperature. The organic phase was extracted, neutralized with sodium bicarbonate, washed with water, and then dried with magnesium sulfate. The solvent was removed under reduced pressure to obtain 800 mg (95 % yield) of a clear oil. ^{1}H NMR (400 MHz, CDCl3, δ ppm): 10.11 (s, 1H, CHO); 8.00 (m, 4H, ArH); 4.17 (m, 4H, - C$\underline{H}_2$-CH_3); 1.35 (t, J = 8.0 Hz, 6H, -CH_2-C$\underline{H}_3$).

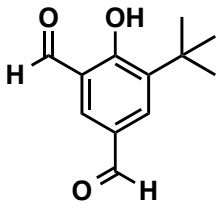

5-Formyl-3-tert-butyl-2-hydroxybenzaldehyde: Following a procedure form the literature[40], a portion of 6.00 g of 2-tert-butylphenol and 14.0 g of hexamethylenetetramine were dissolved in 40 mL of trifluoroacetic acid and heated at 115 ºC for 14 h. The reactionwas quenched while hot with 20 mL of 33% H_2SO_4. The crude product was extracted with dichloromethane, neutralized with a saturated aqueous solution of sodium bicarbonate and washed with water. The organic phase was separated and dried over sodium sulfate and concentrated under reduced pressure. Column chromatography was done using a gradient of hexanes to ethylacetate/hexanes (9:1). The blue fluorescing band was collected and dried under reduced pressure. 3.06 g (37% yield)

of a yellow oil (which turn into a yellow solid after placed in the refrigerator) were obtained. ^{1}H NMR (400 MHz, CDCl3, δ ppm): 12.41 (s, 1H, OH); 10.00 (s, 1H, CHO); 9.93 (s, 1H, CHO); 8.08 (d, J = 2.0 Hz, 1H, ArH); 8.00 (d, J = 2.0 Hz, 1H, ArH); 1.46 (s, 9H, $C(CH_3)_3$).

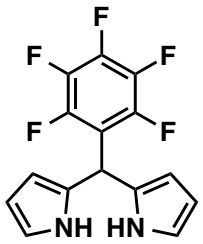

5-(Pentafluorophenyl)dipyrromethane: Following a procedure from the literature[41], a portion of 2 mL of pentafluorobenzaldehyde in 50 mL of freshly distilled pyrrole was degassed with a stream of argon for 10 min before adding 120 μL of trifluoroacetic acid. The mixture was stirred for 30 min at room temperature, diluted with 400 mL of dichloromethane, and then washed with 400 mL of 0.1 M NaOH. The organic phase was washed with water and dried over Na_2SO_4. A short silica pad column was run with a mixture of triethylamine/ethylacetate/hexanes (1:20:80) and after removing the solvent under reduced pressure the product was recrystallized with dichloromethane/hexanes to obtained 3.00 g of a white solid. ^{1}H NMR (400 MHz, $CDCl_3$, δ ppm): 8.11 (s, 2H, NH); 6.72 (td, 2H, ArH); 6.15 (q, 2H, ArH); 6.01 (q, 2H, ArH); 5.89 (s, 1H, CH).

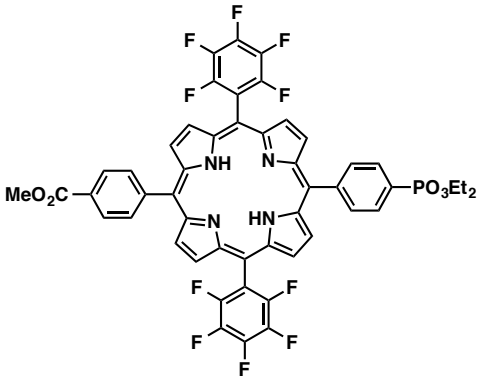

5,15-Bis(pentafluorophenyl)-10-(4-diethoxyphosphorylphenyl)-20-(4-methoxycarbonylphenyl)porphyrin (1):

A portion of 2.0 g of 5-(pentafluorophenyl)dipyrromethane was mixed with 1.00 g of 4-(diethoxyphosphoryl)benzaldehyde diethyl acetal and 525 mg of methyl-4-formylbenzoate in chloroform and a catalytic amount of trifluoroacetic acid (TFA) for 2 h, followed by oxidation of the cyclic porphyrinogen with 2,3-dichloro-5,6-dicyanobenzoquinone (3 equivalents per dipyrromethane dipyrromethane, overnight, RT). This mixture can be separated with column chromatography due to the polarity difference of the methyl ester and diethylphosphonate groups. Three red-fluorescent bands were collected. The solvent of the middle band was removed under reduced pressure to give 253 mg of **1** (8% yield). ^{1}H NMR (400 MHz, CDCl3, δ ppm): 8.90 (4H, d, J = 4.8 Hz, H2, H8, H12 and H18), 8.83 (4H, d, J= 4.8 Hz, H3, H7, H13 and H17), 8.46 (2H, d, J= 8.0 Hz, H3'), 8.29 (6H, m, H2', H5'and H6'), 4.40 (m, 4H, -C$\underline{H}_2$-CH$_3$); 4.12 (3H, s, COOCH3), 1.53 (t, J = 7.2 Hz, 6H, -CH$_2$-C$\underline{H}_3$); -2.87 (2H, s, NH). MALDI-TOF 988.31 (experimental); 988.19 calculated for $C_{50}H_{31}F_{10}N_4O_5P$.

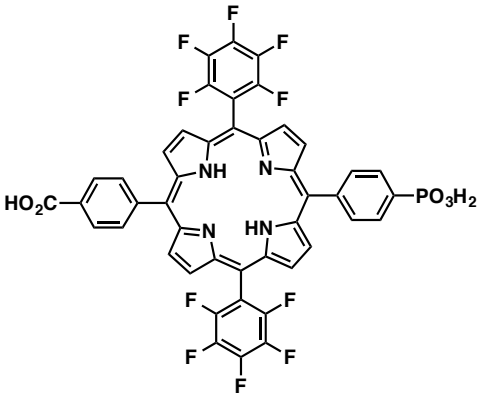

5,15-Bis(pentafluorophenyl)-10-(4-phosphorylphenyl)-20-(4-carboxyphenyl)porphyrin: A portion of 30 mg of **1** was dissolved in 5 mL trifluoroacetic acid and 10 mL of concentrated hydrochloric acid and stirred at 90 ºC. After 48 h, the reaction was cooled to room temperature, diluted with dichloromethane, washed with water, neutralized with sodium bicarbonate solution, and washed with water again. The organic phase was dried and the product recrystallized with hexanes and dichloromethane and 23 mg (82% yield) of a purple solid were obtained. MALDI-TOF 918.34 (experimental); 918.11 calculated for $C_{45}H_{21}F_{10}N_4O_5P$.

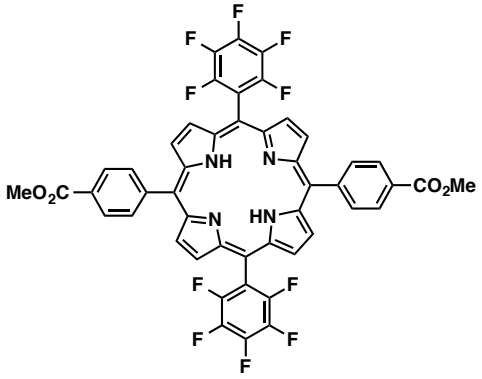

5,15-Bis(pentafluorophenyl)-10,20-bis(4-methoxycarbonylphenyl)porphyrin (2)[42]: A portion of 2.00 g of 5-(pentafluorophenyl)dipyrromethane was mixed with 1.00 g of 4-(diethoxyphosphoryl)benzaldehyde diethyl acetal and 525 mg of methyl-4-

formylbenzoate in chloroform and a catalytic amount of trifluoroacetic acid (TFA) for 2 h, followed by oxidation of the cyclic porphyrinogen with 2,3-Dichloro-5,6-dicyanobenzoquinone (3 equivalents per dipyrromethane, overnight, RT). This mixture can be separated with column chromatography due to the polarity difference of the methyl ester and diethylphosphonate groups. Three red-fluorescent bands were collected. The solvent of the first band was removed under reduced pressure to give 175 mg of **2** (6% yield). ^{1}H NMR (400 MHz, CDCl3, δ ppm): 8.90 (4H, d, J = 4.8 Hz, H2, H8, H12 and H18), 8.83 (4H, d, J= 4.8 Hz, H3, H7, H13 and H17), 8.47 (4H, d, J= 8.0 Hz, H3' and H5'), 8.30 (4H, d, J= 8.0 Hz, H2'and H6'), 4.13 (6H, s, COOCH3), -2.86 (2H, s, NH). MALDI-TOF 910.38 (experimental); 910.16 calculated for $C_{48}H_{24}F_{10}N_4O_4$.

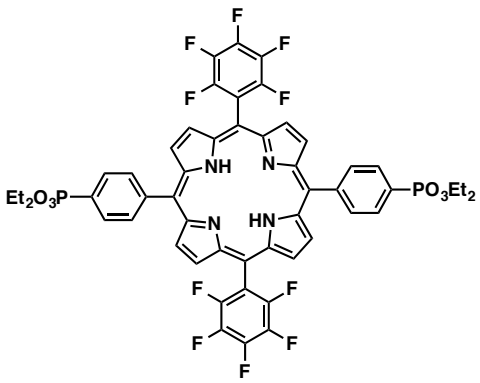

5,15-Bis(pentafluorophenyl)-10,20-bis(4-diethoxyphosphorylphenyl)porphyrin (3): A portion of 2.00 g of 5-(pentafluorophenyl)dipyrromethane was mixed with 600 mg of 4-(diethoxyphosphoryl)benzaldehyde diethyl acetal in chloroform under an argon atmosphere and a 500 μL of trifluoroacetic acid (TFA) was added. The reaction was left stirring for 24 h, followed by oxidation of the cyclic porphyrinogen with 2,3-dichloro-5,6-dicyanobenzoquinone (3 equivalents per dipyrromethane, overnight, RT) to form 340 mg of **3** (10% yield). ^{1}H NMR (400 MHz, CDCl3, δ ppm): 8.98 (4H, d, J = 4.8 Hz, H2,

H8, H12 and H18), 8.82 (4H, d, J= 4.8 Hz, H3, H7, H13 and H17), 8.32 (4H, m, H3' and H5'), 8.23 (4H, m, H2'and H6'), 4.39 (m, 8H, -C<u>H</u>$_2$-CH$_3$); 1.51 (t, J = 7.2 Hz, 12H, -CH$_2$-C<u>H</u>$_3$); -2.89 (2H, s, NH). MALDI-TOF 1066.69 (experimental); 1066.21 calculated for $C_{52}H_{38}F_{10}N_4O_6P_2$.

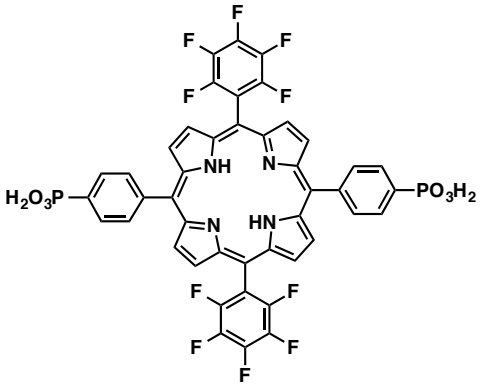

5,15-Bis(pentafluorophenyl)-10,20-bis(4-phosphorylphenyl)porphyrin: A portion of 30 mg of **3** was treated with 134 mg (32 eq.) of Si(CH$_3$)$_3$Br in dichloromethane under an argon atmosphere at room temperature. After 24 h, the solvent was removed under reduced pressure, methanol was added, and this solution was stirred for 1 h. The methanol was then removed under reduced pressure and the product recrystallized from dichloromethane and hexanes to get 26 mg (97% yield) of a purple solid. MALDI-TOF 954.29 (experimental); 954.09 calculated for $C_{44}H_{22}F_{10}N_4O_6P_2$.

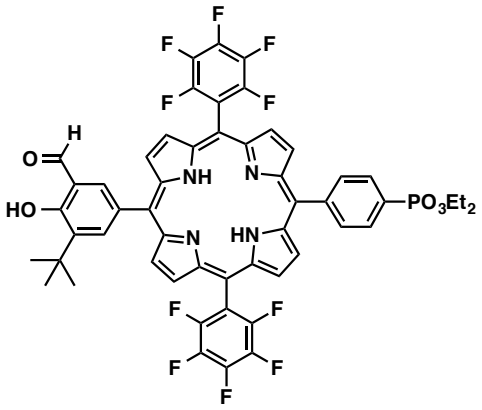

5,15-Bis(pentafluorophenyl)-10-(4-diethoxyphosphorylphenyl)-20-(3-formyl-4-hydroxy-5-tertbutylpheynyl)porphyrin (4): A portion of 810 mg of 5-(pentafluorophenyl)dipyrromethane was mixed with 270 mg of 5-formyl-3-tert-butyl-2-hydroxybenzaldehyde, 330 mg of 4-(diethoxyphosphoryl)benzaldehyde and 2 mL of ethanol in 325 mL of chloroform under an argon atmosphere. Then 125 μL of $BF_3{\cdot}OEt_2$ was added and the reaction was stirred for 1 h, followed by oxidation of the cyclic porphyrinogen with 740 mg of 2,3-dichloro-5,6-dicyanobenzoquinone. The crude was run trough a pad of silica with a gradient of chloroform to ethyl acetate/chloroform (1:5) and three fractions were collected. The second fraction contained the mayority of the desired product as confirmed by MALDI-TOF. Column chromatography was performed on this fraction with a gradient of dichloromethane to ethyl acetate in dichloromethane (5:95) and after drying the mayor band, 165 mg (12% yield) of **4** were obtained. ^{1}H NMR (400 MHz, $CDCl_3$, δ ppm): 12.24 (1H, s, OH), 10.14 (1H, s, CHO), 8.97 (2H, d, J = 5.0 Hz, Ar-porphyrin), 8.90 (2H, d, J = 5.0 Hz, H2 and H18), 8.85 (4H, t, H3, H7, H13 and H17), 8.42 (1H, d, J = 2.0 Hz, H2'), 8.33 (2H, br, H3" and H5"), 8.25 (3H, m, H6', H2" and H6"), 4.41 (4H, m, -C<u>H</u>$_2$-CH$_3$), 1.62 (9H, s, C(CH3)3), 1.54 (6H, t, J= 7.2 Hz, -CH$_2$-

C<u>H</u>$_3$), -2.82 (2H, s, NH). MALDI-TOF 1030.61 (experimental); 1030.23 calculated for $C_{53}H_{37}F_{10}N_4O_5P$.

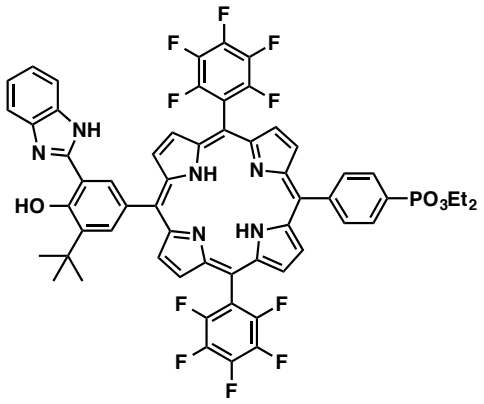

5,15-Bis(pentafluorophenyl)-10-(4-diethoxyphosphorylphenyl)-20-[2'-(3"-tert-butyl-2"-hydroxyphenyl)benzimidazole]porphyrin (5): A portion of 76 mg of 5,15-bis(pentafluorophenyl)-10-(4-diethoxyphosphorylphenyl)-20-(3-formyl-4-hydroxy-5-tertbutylpheynyl)porphyrin (4) was dissolved in 2 mL of nitrobenzene and 8 mg of 1,2-phenyldiamine were dissolved in 3 mL of nitrobenzene. The porphyrin solution was added to the amine solution drop wise. The solution was then heated at 210 ºC under an argon atmosphere. After 12 h under these conditions, the reaction was left to cool to room temperature and then the crude was transferred to a chromatography column (SiO_2 packed with hexanes). Nitrobenzene was eluted with hexanes and the target compound with a gradient of hexanes/dichloromethane (1:1), dichloromethane, and finally ethylacetate/dichloromethane (5:95). The red-fluorescent band obtained from the column was recrystallized with dichloromethane and hexanes, and then dried under reduced pressure to obtain 40 mg (49% yield) of **5**. MALDI-TOF 1118.32 (experimental); 1118.28 calculated for $C_{59}H_{41}F_{10}N_6O_4P$.

Cyclic voltammetry

In order to measure the redox potentials of porphyrins **1-3** (in the ester form), a 0.1M solution of tetrabutylammonium hexafluorophosphate ($TBAPF_6$) in 1.5 mL of anhydrous benzonitrile was prepared and multiple background cyclic voltammograms (CVs) of the solution were taken. Then ~2 mg of the porphyrin sample was added and the CVs measurements taken. The CV-curve of **2** is shown in Figure 6 and the data for dyes **1-3** are presented in Table 1. As expected, the oxidation of all three **PF_{10}** dyes is ca. 0.7 V more positive than the potential for the four-electron oxidation of water at neutral pH.

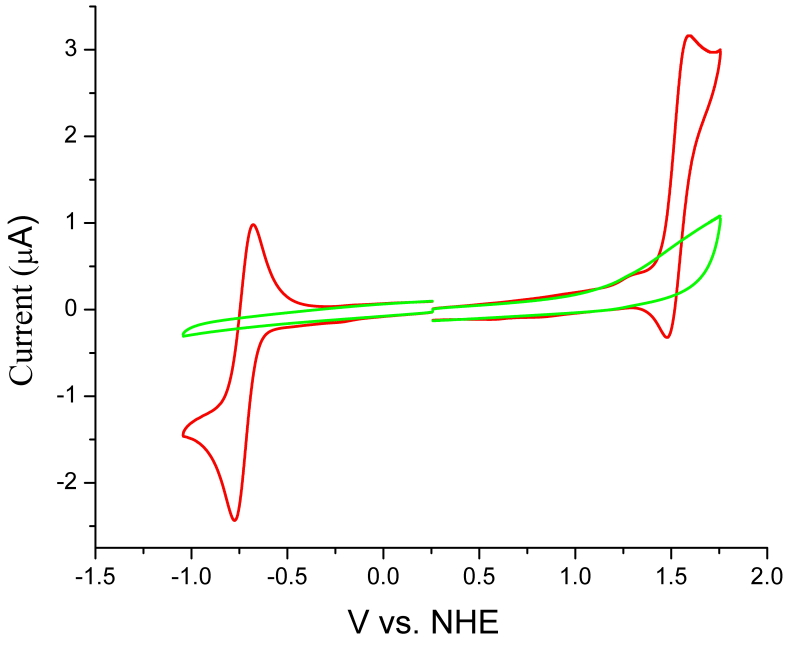

Figure 6. Cyclic voltammetry curve of **3**. Background curve (green line) and measurement with **3**, in a 0.1M $TBAPF_6$ solution in benzonitrile.

Compound	Oxidation potential (V vs NHE)	Reduction Potential (V vs NHE)
1	1.51	-0.76
2	1.51	-0.75
3	1.52	-0.76

Table 1. First oxidation and first reduction potentials (V vs NHE) for porphyrins **1-3** in a 0.1M $TBAPF_6$ solution in benzonitrile. Ferrocene/ferrocenium couple was used as an internal reference.

2.2 Synthesis of red-absorbing dyes

The structures of the phthalocyanines (**7-9**) and the naphthalocyanine-phthalocyanine hybrid (**6**) made in this work are shown in Figure 7. These dyes can be made in three steps and the general synthetic scheme is shown in Figures 8 and 9.

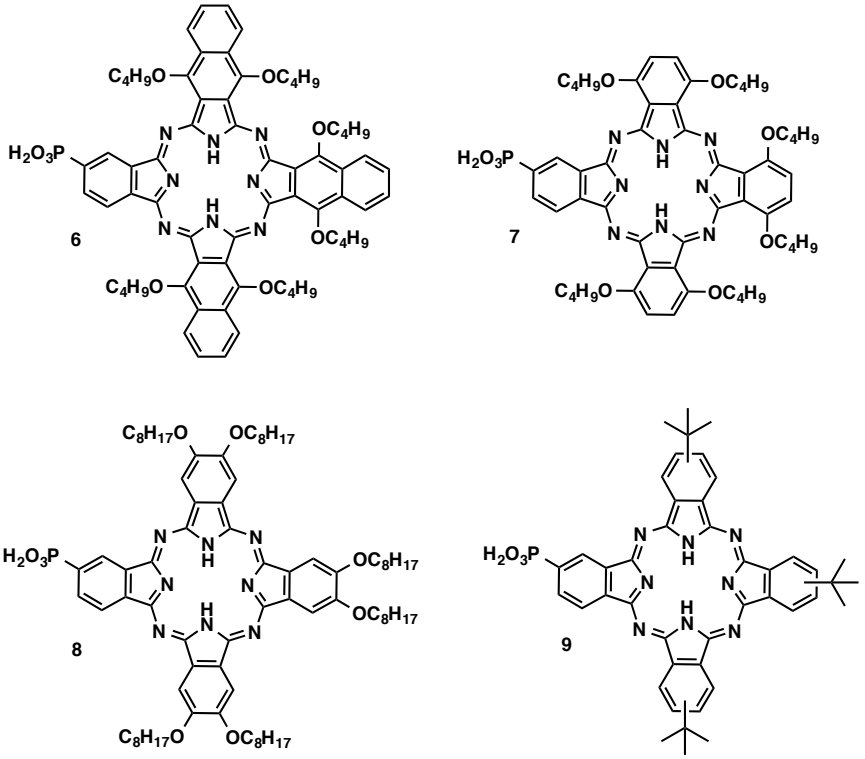

Figure 7. Structures of the red-absorbing dyes made.

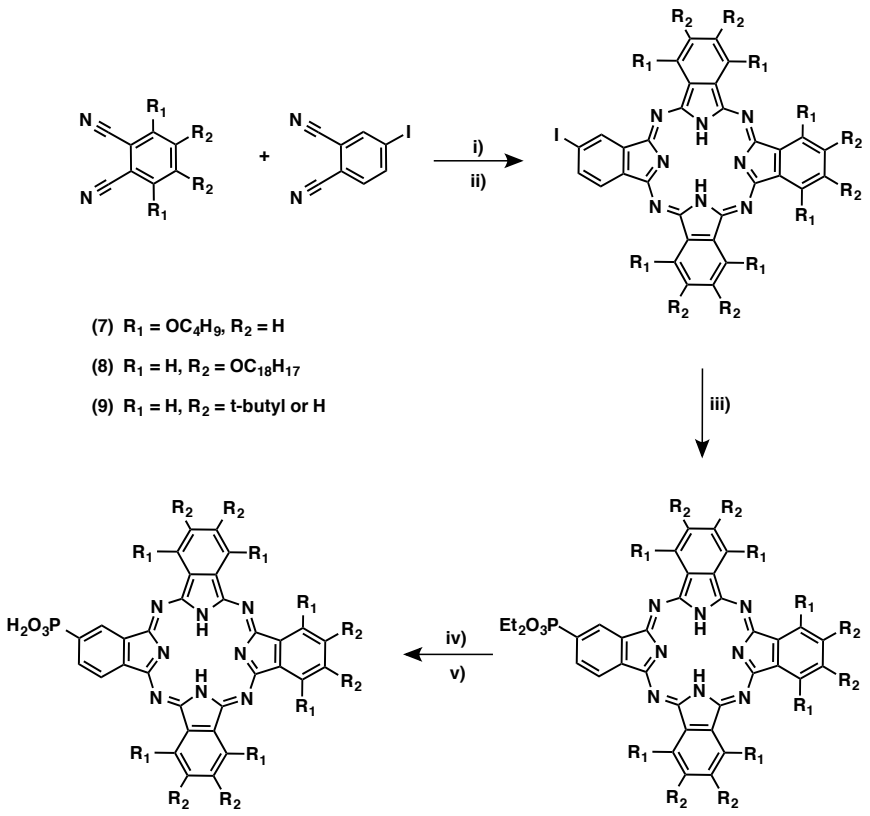

Figure 8. General synthetic scheme for phthalocyanines. i) Li, 1-butanol, reflux, 2 h; ii) acetic acid overnight; iii) diethylphosphite, Pd(0), dry toluene:TEA (1:1), overnight; iv) $Si(CH_3)_3Br$ in dichloromethane, 24-48 h; v) methanol or water.

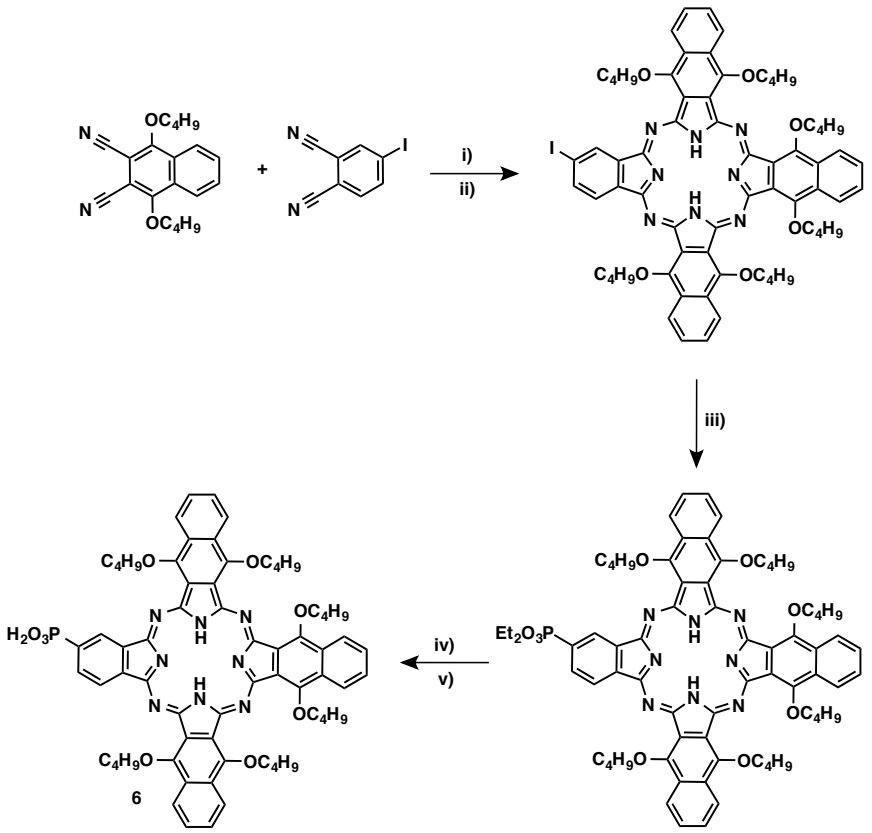

Figure 9. Synthetic scheme for compound **6**. i) Li, 1-butanol, reflux, 2 h; ii) acetic acid overnight; iii) diethylphosphite, Pd(0), dry toluene:TEA (1:1), overnight; iv) $Si(CH_3)_3Br$ in dichloromethane, 24-48 h; v) methanol or water.

Experimental details and characterization:

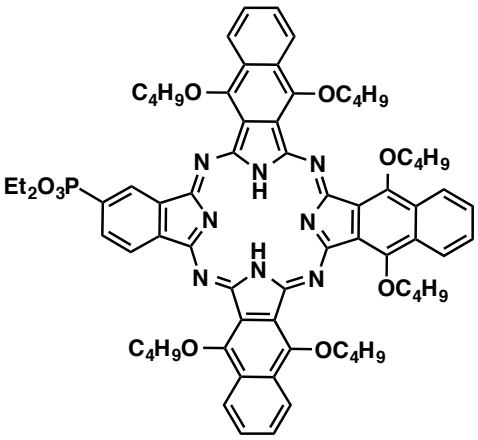

(α-OC_4H_9)$_6$-Nc_3Pc_1-PO_3Et_2 (6-ester): A portion 262 mg of 4-iodophthalonitrile and 1.00 g of 3,6-dibutoxy-1,2-naphthalodicarbonitrile were warmed in 10 mL of 1-butanol under an argon atmosphere until everything dissolved. Then 290 mg of lithium metal was added to the mixture, which turned blue immediately. The reaction was left to reflux for 2 h and then it was allowed to cool down to room temperature. Then the reaction was quenched with 10 mL of acetic acid. The resulting mixture was separated by column chromatography (SiO_2 with a gradient of hexanes and dichloromethane). A portion of 65 mg of the fraction with the highest concentration of the desired precursor (**(α-OC_4H_9)$_6$-Nc_3Pc_1-iodo**, determined with MALDI-TOF and TLC) was mixed with 10 mg of diethylphosphite, and 5 mg of tetrakis-(triphenylphosphine)Pd(0) in 2 mL of toluene/trietylamine (1:1) mixture and heated at 80 ºC. After 3 h, the reaction was left to cool down, filtered and the solvent was removed under reduced pressure. The resulting mixture was separated by column chromatography to obtain 44 mg (3% yield) of the desired product. ^{1}H NMR (400 MHz, $CDCl_3$, δ ppm): 9.83 (1H, d, J = Hz, ArH), 9.42 (1H, dd, J = Hz, ArH), 9.01 (2H, m, ArH), 8.91 (2H, m, ArH), 8.83 (2H, m, ArH), 8.57 (1H, dd, ArH), 7.96 (2H, m, ArH), 7.86 (4H, m, ArH), 5.15 (12H, m, -O-C$\underline{H_2}$-CH_2-CH_2-

CH_3); 4.38 (4H, m, -C<u>H</u>$_2$-CH_3), 2.54 (4H, m, -O-CH_2-C<u>H</u>$_2$-CH_2-CH_3); 2.40 (2H, s, NH); 2.20 (8H, m, -O-CH_2-C<u>H</u>$_2$-CH_2-CH_3); 1.94 (4H, m, -O-CH_2-CH_2-C<u>H</u>$_2$-CH_3); 1.64 (8H, m, -O-CH_2-CH_2-C<u>H</u>$_2$-CH_3); 1.50 (6H, t, J= 7.2 Hz, -CH_2-C<u>H</u>$_3$); 1.23 (6H, m, -O-CH_2-CH_2-CH_2-C<u>H</u>$_3$); 1.01 (12H, m, -O-CH_2-CH_2-CH_2-C<u>H</u>$_3$). MALDI-TOF 1232.45 (experimental); 1232.59 calculated for $C_{72}H_{81}N_8O_9P$.

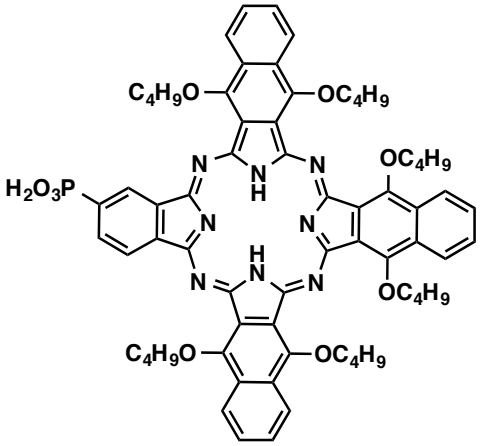

(α-OC_4H_9)$_6$-Nc_3Pc_1-PO_3H_2 (6): A portion of 25 mg of **6-ester** was treated with 150 μL of $Si(CH_3)_3Br$ in 5 mL of CH_2Cl_2 at room temperature. After 24 h, the solvent was removed under reduced pressure, methanol was added, and this solution was stirred for 1 h. The methanol was then removed under reduced pressure and the product recrystallized from dichloromethane and methanol to get 24 mg (100% yield) of **6**. MALDI-TOF 1176.71 (experimental); 1176.52 calculated for $C_{72}H_{81}N_8O_9P$.

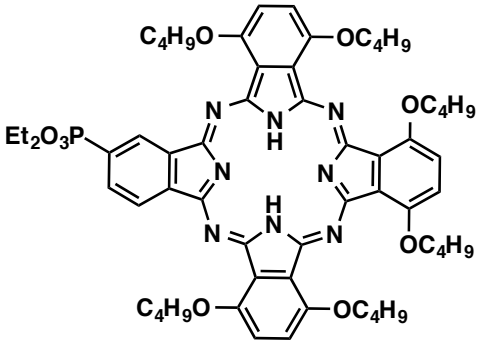

2-Diethoxyphosphoryl-8,11,15,18,22,25-hexabutoxy-29H,31H-phthalocyanine: A portion of 311 mg of 4-iodophthalonitrile and 1.00 g 3,6-dibutoxy-1,2-benzenedicarbonitrile were warmed in 8 mL of 1-butanol under an argon atmosphere until everything dissolved. Then lithium metal was added to the mixture, which turned green immediately. The reaction was left to reflux for 2 h and then allowed to cool down to room temperature. Then the reaction was quenched with 10 mL of acetic acid. The resulting mixture was separated by column chromatography. The fraction with the highest concentration of the desired precursor (2-iodo-8,11,15,18,22,25-hexabutoxy-29H,31H-phthalocyanine, determined with MALDI-TOF and TLC) was allowed to react with 1.2 eq. of diethylphosphite, and 0.1% mol of tetrakis-(triphenylphosphine)Pd(0) in a toluene/trietylamine (1:1) mixture at 80 ºC. After 20 h the reaction was filtered and the solvent was removed under reduced pressure. The resulting mixture was separated by column chromatography (gradient of ethyl acetate and toluene on SiO_2) to obtain 28 mg (2% yield) of the desired product. ^{1}H NMR (400 MHz, $CDCl_3$, δ ppm): 9.74 (1H, d, J = 13.6 Hz, ArH); 9.38 (1H, m, ArH); 8.60 (1H, m, ArH); 7.66 (6H, m, ArH); 4.87 (8H, m, -O-C$\underline{H}_2$-CH_2-CH_2-CH_3); 4.73 (4H, m, -O-C$\underline{H}_2$-CH_2-CH_2-CH_3); 4.36 (4H, m, -C$\underline{H}_2$-CH_3), 2.51 (4H, m, -O-CH_2-C$\underline{H}_2$-CH_2-CH_3); 2.17 (8H, m, -O-CH_2-C$\underline{H}_2$-CH_2-CH_3); 2.10 (4H, m, -O-CH_2-CH_2-C$\underline{H}_2$-CH_3); 1.68 (8H, m, -O-CH_2-CH_2-C$\underline{H}_2$-CH_3); 1.48 (6H, t, J= 7.2 Hz,

-CH_2-C<u>H</u>$_3$); 1.29 (6H, m, -O-CH_2-CH_2-CH_2-C<u>H</u>$_3$); 1.09 (12H, m, -O-CH_2-CH_2-CH_2-C<u>H</u>$_3$); 0.17 (2H, s, NH). MALDI-TOF 1082.70 (experimental), 1082.54 calculated for $C_{60}H_{75}N_8O_9P$.

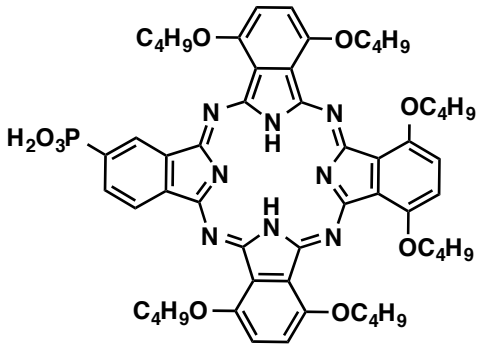

2-Phosphoryl-8,11,15,18,22,25-hexabutoxy-29H,31H-phthalocyanine (7): A portion of 10 mg of 2-diethoxyphosphoryl-8,11,15,18,22,25-hexabutoxy-29H,31H-phthalocyanine was treated with 16 eq. of $Si(CH_3)_3Br$ in CH_2Cl_2 at room temperature. After 24 h, the solvent was removed under reduced pressure, methanol was added, and this solution was stirred for 1h. The methanol was then removed under reduced pressure and the product recrystallized from dichloromethane and hexanes to get 8 mg (84% yield) of a green solid. MALDI-TOF 1026.55 (experimental), 1026.48 calculated for $C_{56}H_{67}N_8O_9P$.

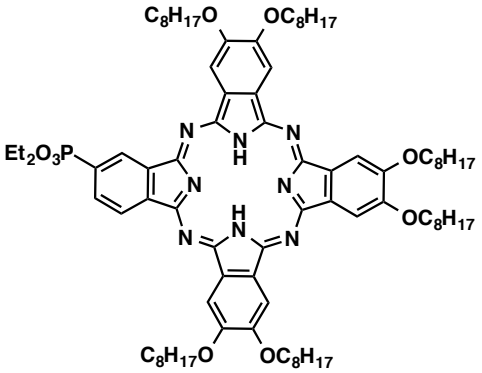

2-Diethoxyphosphoryl-9,10,16,17,23,24-hexakis(octyloxy)-29H,31H-phthalocyanine:

A portion of 221 mg of 4-iodophthalonitrile and 1.00 g of 4,5-dioctyloxy-1,2-benzenedicarbonitrile were warmed in 1-butanol under an argon atmosphere until everything dissolved. Then lithium metal was added to the mixture, which turned blue immediately. The reaction was left to reflux for 2 h and then allowed to cool down to room temperature. Then the reaction was quenched with 10 mL of acetic acid. The resulting mixture was separated by column chromatography. The fraction with the highest concentration of the desired precursor (2-iodo-9,10,16,17,23,24-hexakis(octyloxy)-29H,31H-phthalocyanine, determined with MALDI-TOF and TLC) was allowed to react with 1.2 eq. of diethylphosphite, and 0.1% mol of tetrakis-(triphenylphosphine)Pd(0) in a toluene/trietylamine (1:1) mixture at 80 ºC. After 20 h the reaction was filtered and the solvent was removed under reduced pressure. The resulting mixture was separated by column chromatography to obtain 39 mg (3% yield) of the desired product (green solid). ^{1}H NMR (400 MHz, $CDCl_3$, δ ppm): 9.65 (1H, d, J = 13.6 Hz, ArH); 8.988 (1H, s, ArH); 8.24 (7H, br, ArH); 4.49 (16H, m, -O-C$\underline{H}_2$-CH_{12}-CH_3 and -O-C$\underline{H}_2$-CH_3); 2.19 (12H, m, -O-CH_2-C$\underline{H}_2$-CH_{10}-CH_3); 1.79 (12H, m, -O-CH_4-C$\underline{H}_2$-CH_8-CH_3); 1.5 (54H, br, -O-CH_6-C$\underline{H}_8$- CH_3 and -O-CH_2-C$\underline{H}_3$); 0.95 (18H, m, -O-CH_{14}-C$\underline{H}_3$); -3.37 (2H, s, NH). MALDI-TOF 1419.15 (experimental), 1418.92 calculated for $C_{84}H_{123}N_8O_9P$.

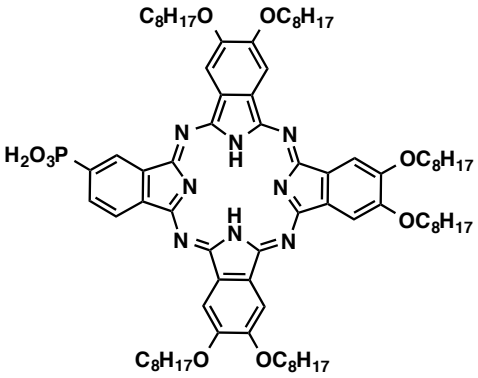

2-Phosphoryl-9,10,16,17,23,24-hexakis(octyloxy)-29H,31H-phthalocyanine (8): A portion of 8 mg of 2-diethoxyphosphoryl-9,10,16,17,23,24-hexakis(octyloxy)-29H,31H-phthalocyanine was treated with 40 μL of $Si(CH_3)_3Br$ in CH_2Cl_2 at room temperature. After 24 h, the solvent was removed under reduced pressure, methanol was added, and this solution was stirred for 1 h. The methanol was then removed under reduced pressure and the product recrystallized from dichloromethane and hexanes to get 7 mg (90% yield) of a green solid. MALDI-TOF 1362.91 (experimental), 1362.85 calculated for $C_{80}H_{115}N_8O_9P$.

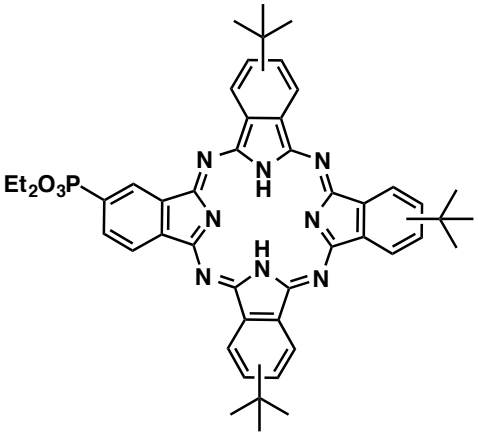

2-Diethoxyphosphoryl-9,16,23-tetra-tert-butyl-29H,31H-phthalocyanine: A portion of 230 mg of 4-iodophthalonitrile and 500 mg of 4-tert-butylphthalonitrile were warmed

in 1-butanol under an argon atmosphere until everything dissolved. Then lithium metal was added to the mixture, which turned blue immediately. The reaction was left to reflux for 2 h and then it was allowed to cool down to room temperature. Then the reaction was quenched with 10 mL of acetic acid. The resulting mixture was separated by column chromatography. The fraction with the highest concentration of the desired precursor (2-iodo-9,16,23-tetra-tert-butyl-29H,31H-phthalocyanine, determined with MALDI-TOF and TLC) was treated with 1.2 eq. of diethylphosphite, and 0.1%mol of tetrakis-(triphenylphosphine)Pd(0) in a toluene/trietylamine (1:1) mixture at 80 ºC. After 20 h the reaction was filtered and the solvent was removed under reduced pressure. The resulting mixture was separated by column chromatography to obtain 20 mg (3% yield) of the desired product. ^{1}H NMR (400 MHz, $CDCl_3$, δ ppm): 9.43 (2H, m, ArH); 9.0 – 7.8 (10H, m, ArH); 4.54 (4H, m, -O-C<u>H</u>$_2$-CH$_3$); 1.84 (27H, m, -C(CH$_3$)$_3$); 1.64 (6H, m, -O-CH$_2$-C<u>H</u>$_3$); -3.34 (2H, br, NH). MALDI-TOF 818.74 (experimental), 818.38 calculated for $C_{48}H_{51}N_8O_3P$.

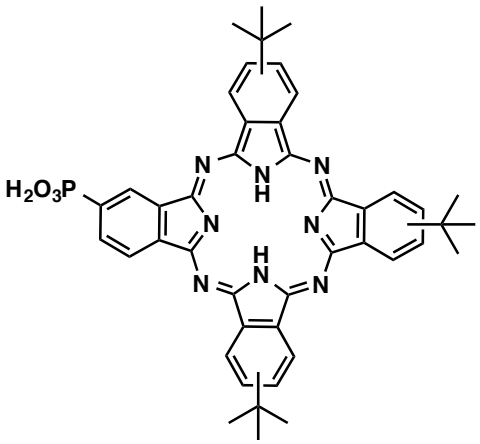

2-Phosphoryl-9,16,23-tetra-tert-butyl-29H,31H-phthalocyanine (9): A portion of 16 mg of 2-fiethoxyphosphoryl-9,16,23-tetra-tert-butyl-29H,31H-phthalocyanine was

treated with 100 μL of $Si(CH_3)_3Br$ in 2 mL of dry dichloromethane at room temperature. After 24 h, the solvent was removed under reduced pressure, methanol was added, and this solution was stirred for 1 h. The methanol was then removed under reduced pressure and the product recrystallized from dichloromethane and hexanes to get 10 mg (67% yield) of a blue solid. MALDI-TOF 762.55 (experimental); 762.32 calculated for $C_{48}H_{51}N_8O_3P$.

Absorption spectra, theoretical calculations and dye sensitized solar cells.

The normalized UV-Vis spectra of dyes **6-9** are shown in Figure 10. The energy of the maximum absorption peak correlates well with the energy gap of the HOMO-LUMO calculated by DFT (Figure 11).

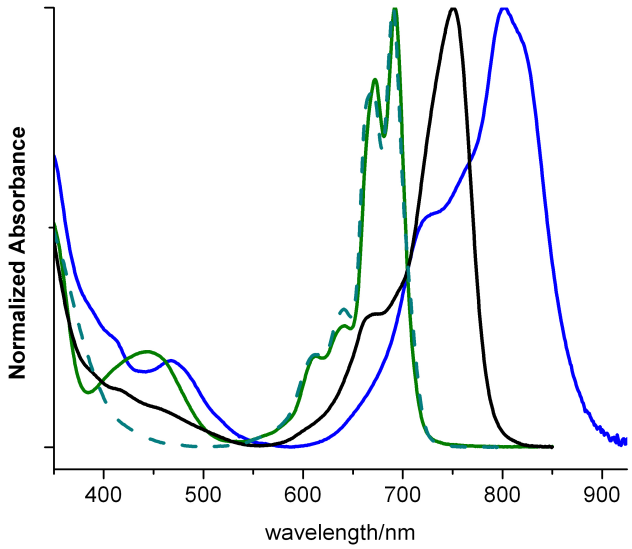

Figure 10. UV-Vis spectra for dyes **6-9**. Blue line corresponds to **6**, black line line corresponds to **7**, green line corresponds to **8**, and cyan dashed line corresponds to **9**.

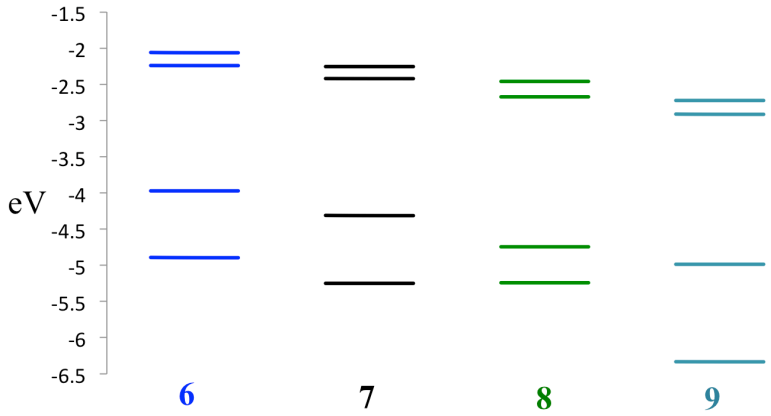

Figure 11. DFT-calculated HOMO-LUMO energies for dyes **6-9**.

Dyes **6** and **8** were tested in DSSCs, and the results are shown on Figure 12 and 13, respectively. Even though **6** aggregates less and absorbs more light than **8**, the efficiency obtained for **6** is two orders of magnitude lower than for **8**. This was rationalized based on the DFT-calculated HOMO-LUMO energies of these dyes (Figure 11). The HOMO energy for **6** is much higher than for **8**. Thus, it is expected that the oxidation potential of **6** is not as positive as the oxidation potential of **8**. Therefore **6** have less driving force to oxidize the I^-/I_3^- redox mediator resulting in slower regeneration of the dye and faster recombination of injected electrons yielding lower efficiencies.

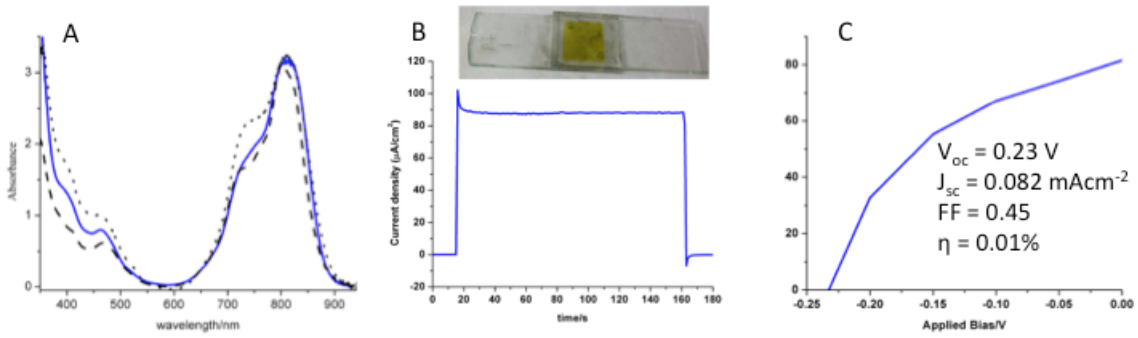

Figure 12. Photocurrents measured for **6**. **A)** UV-Vis spectra for **6** in solution (black dashed line), on TiO_2 without chenodeoxycholic acid (CDCA) (black dotted line) and on TiO_2 co-absorbed with CDCA (blue solid line). **B)** Photocurrent as a function of time obtained for a DSSC made with **6**. **C)** Photocurrent as a function of applied bias obtained for a DSSC made with **6**.

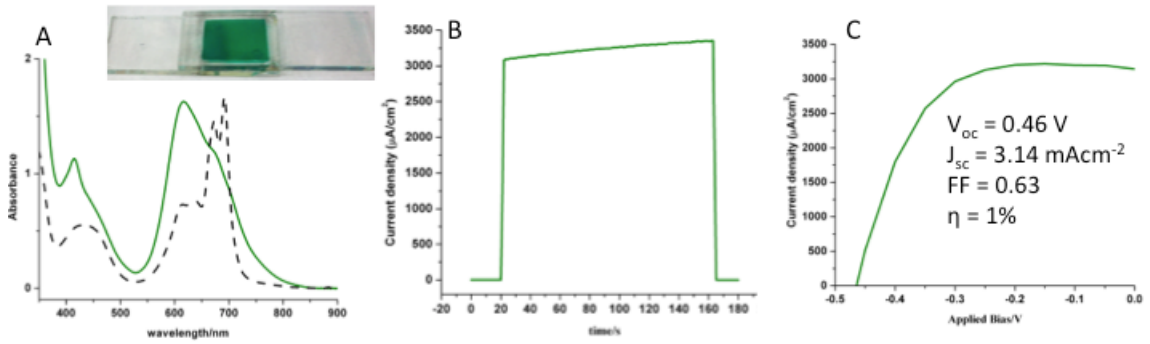

Figure 13. Photocurrents measured for **8**. **A)** UV-Vis spectra for **8** in solution (black dashed line) and on TiO_2 co-absorbed with CDCA (green solid line). **B)** Photocurrent as a function of time obtained for a DSSC made with **8**. **C)** Photocurrent as a function of applied bias obtained for a DSSC made with **8**.

CHAPTER 3

WATER-SPLITTING DYE-SENSITIZED PHOTOELECTOCHEMICAL TANDEM CELLS

Water-splitting dye-sensitized photoanodes (WSDSPAs) can generate about 1 V of photovoltage and because the splitting of water into its constituent elements require on average 1.23 V per electron, a small external bias (about 200 mV) is required for these single junction electrodes to work properly[15,16,19,30]. Water-splitting dye-sensitized photoelectrochemical tandem cells (WSDSPETCs) have the advantage of using more efficiently the energy from more solar photons than does a single junction cell, given that the junctions absorb at complementary wavelengths[8,22] (Figure 2, Chapter 2). The combination of dyes with different absorption spectra provides the ability to absorb in a wider range of the solar spectrum, and thus the tandem design uses light from bluer photons more efficiently as the bias required for the WSDSPAs to work properly is provided by the second junction in the form of a DSSC.

In our tandem system (Figure 1, Chapter 1), high-potential porphyrins or ruthenium dyes were used as the blue absorbing dyes on WSDSPAs. These dyes are co-deposited with a water oxidation catalyst. Phthalocyanines or push-pull porphyrins were used as the red absorbing dyes. These red-absorbing dyes sensitize a DSSC that is connected to the WSDSPAs and a platinum electrode (for proton reduction) providing the extra potential required for the reduction of protons to hydrogen gas. The structures of the dyes and catalysts used on this chapter are shown in Figure 14. The UV-Vis spectra of the dyes adsorbed to TiO_2 are shown in Figure 15.

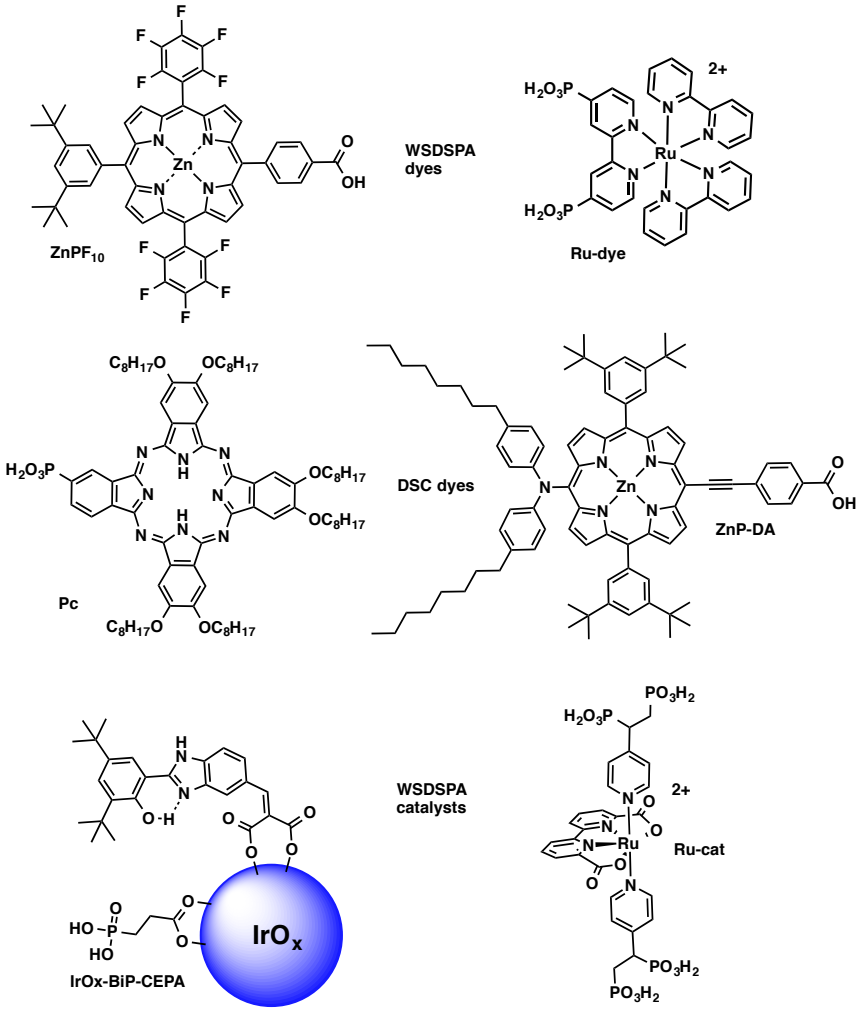

Figure 14. Dyes and catalysts used for WSDSPETCs. **$ZnPF_{10}$** was made by Marely Tejeda, **Ru-dye** and **Ru-cat** was made by Dr. Javier Concepción from Brookhaven National Lab, the synthesis of **Pc** can be found on Chapter 2, **ZnP-DA** was made by Dr. Paul Liddell, **IrOx-BiP-CEPA** was made following a procedure from the literature[16] and the BiP mediator moiety of **IrOx-BiP-CEPA**, 2-((2-(3,5-Di-tert-butyl-2-hydroxyphenyl)-1H-benzo[d]imidazol-5-yl-methylene)malonic acid, was made by Dr. Jackson Megiatto and Marely Tejeda as previously reported[16].

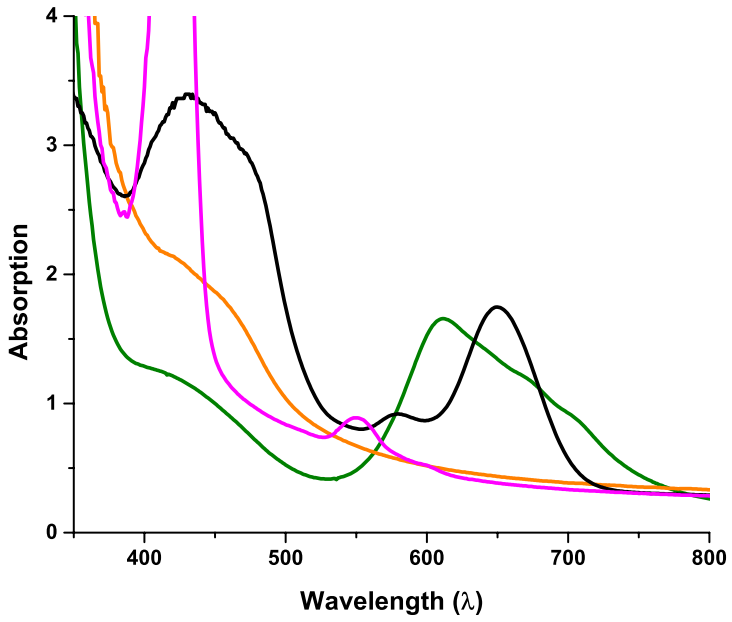

Figure 15. UV-Vis of dyes on TiO_2. **Ru-dye** (orange line), **$ZnPF_{10}$** (pink line), **Pc** (green line) and **ZnP-DA** (black line).

Photocurrents produced by WSDSPETCs

The highest photocurrents measured for WSDSPETCs made with different combinations of the dyes and catalysts in Figure 14 are presented in Figure 16.

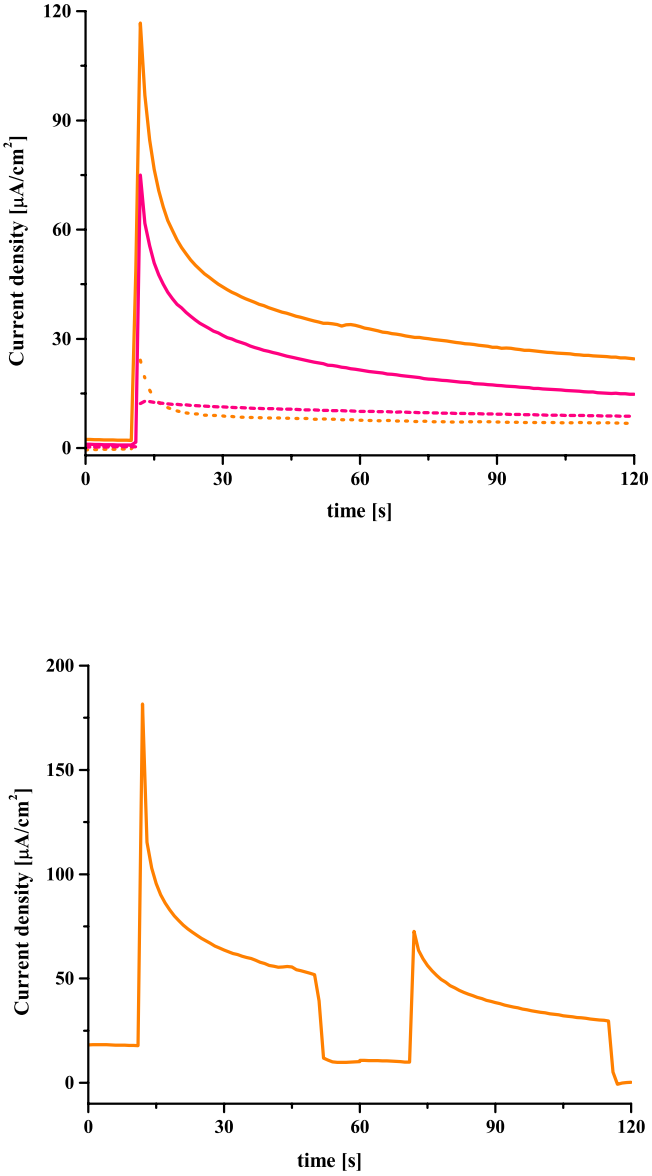

Figure 16. Examples of photocurrents obtained for WSDSPETDs made with different combinations of dyes and catalyst. Top: WSDSPA = **Ru-dye** + **IrOx-BiP-CEPA** and DSSC = **Pc** (orange solid line); without DSSC (dashed orange line). WSDSPA = **ZnPF$_{10}$**,

IrOx-BiP-CEPA and DSSC = **Pc** (pink solid line); without DSSC (dashed pink line). Bottom: WSDSPA = **Ru-dye** + **Ru-cat** and DSSC = **ZnP-DA** (orange line).

The highest WSDSPETCs photocurrents were observed for WSDSPAs that contained **Ru-dye**. The currents for these cells were comparable even though different catalysts and DSSC dyes were used. For WSDSPETCs with $\mathbf{ZnPF_{10}}$ in the WSDSPA currents were a little lower, but in the order of tens of $\mu A/cm^2$. Lower photocurrents were observed when WSDSPAs were not connected to a DSSC (dashed lines in Figure 16) showing the importance of supplying a bias for the WSDSPAs to be able to reduced protons to hydrogen gas. In general the photocurrents obtained for our WSDSPETCs are comparable the photocurrents obtained for similar WSDSPAs under an applied external bias.

Photocurrent as a function of applied bias

Two DSSC (one made with **Pc** and the other with **ZnP-DA**) were connected in series to make a tandem DSSC and the photocurrents as a function of applied bias for this cell and its components is shown in Figure 17. The cell with **ZnP-DA** cell was placed behind the **Pc** cell because it was darker than the **Pc** cell and both cells absorb in the same region of light. It was observed that the photocurrents of the **tandem-DSSC** were limited by the cell with the lowest photocurrent (**ZnP-DA** cell behind **Pc** cell). The open-circuit voltage of the tandem cell is equivalent to the sum of the open-circuit voltage of the component cells.

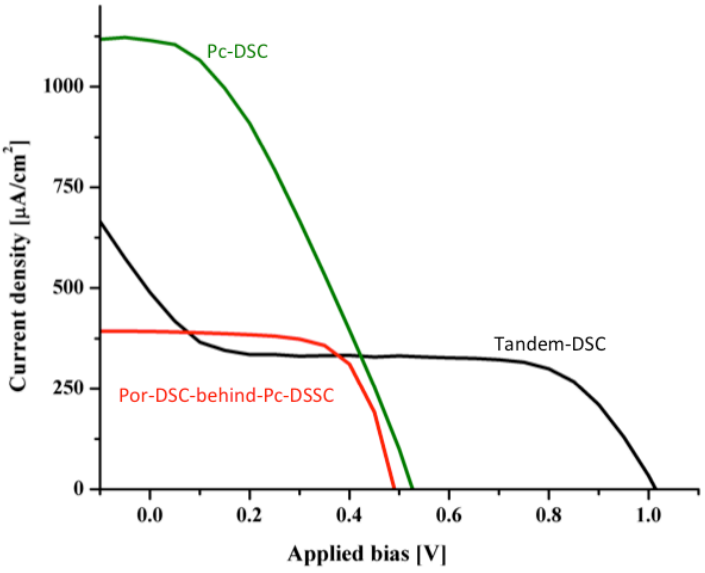

Figure 17. Photocurrent as a function of applied bias for two DSSCs measured independently and connected in series (**tandem-DSSC**). DSSC made with **Pc** dye (green line), DSSC made with **ZnP-DA** measured with the cell behind the **Pc** DSSC (red line), the two cells connected in series one behind the other (black line).

Figure 18 shows photocurrents as a function of applied bias for the **Pc** and **tandem** DSSCs along with WSDSPAs made with **$ZnPF_{10}$** or **Ru-dye** both co-adsorbed with **IrOx-BiP-CEPA**. The crossing of the WSDSPAs and the DSSCs curves can be used to estimate the photocurrents expected when the systems are wired in series.

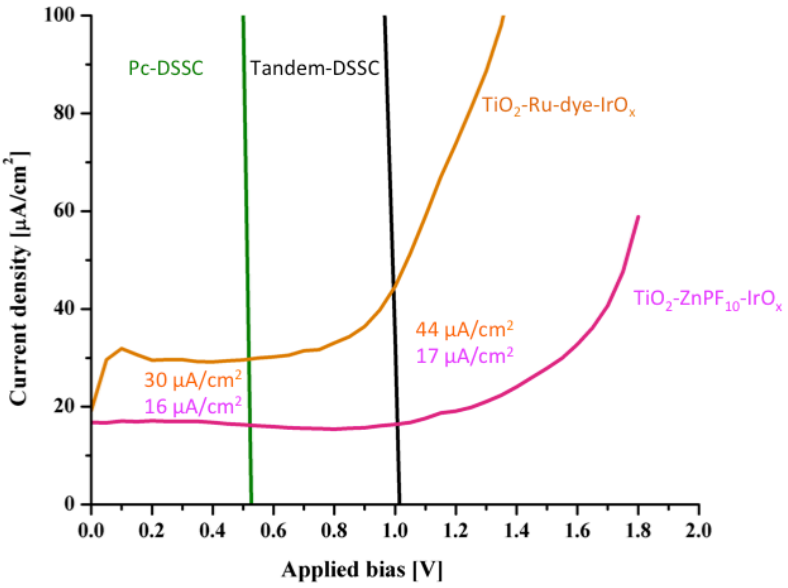

Figure 18. Photocurrent as a function of applied bias for different WSDSPAs and DSSCs.

Figure 19 shows photocurrents as a function of time for three different WSDSPETCs configurations. The first 40 s of illumination corresponds at the WSDSPAs at 0 V not connected to the DSSCs. The next 40 s of illumination corresponds to the WSDSPAs connected in series to the **Pc** DSSC, which provides about 0.5 V to the WSDSPAs. The last 40 s of illumination corresponds to the WSDSPAs connected in series to the tandem DSSC, which provides about 1 V of bias to the WADSPAs.

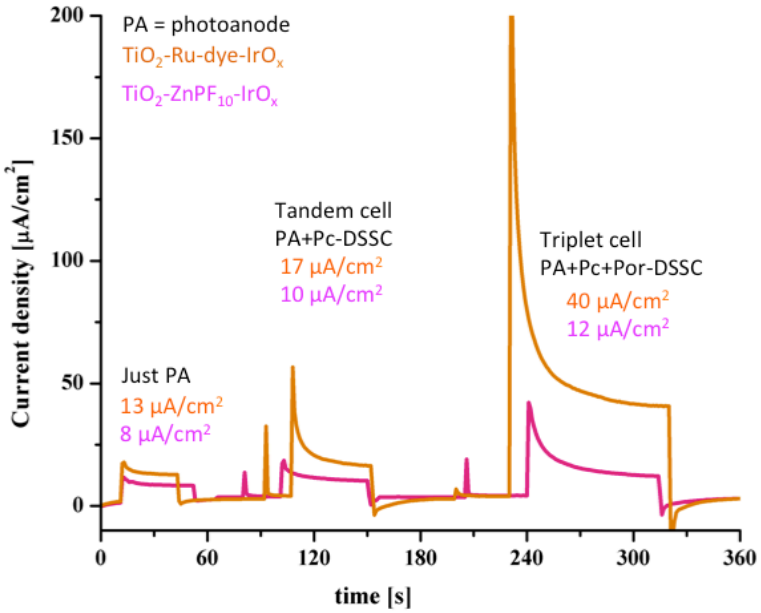

Figure 19. WSDSPETCs photocurrent dependence on potential provided by the DCCSs.

In conclusion, it has been demonstrated that WSDSPETCs can work with an external applied bias. In general the higher the open-circuit voltage of the DSSC connected to the WSDSPAs the higher the photocurrents observed. Present photocurrents produced are limited by the WSDSPA efficiency, which is due to slow hole transfer to the catalyst and fast recombination to both the dyes and catalyst on the surface[15,16]. Current research focuses on increasing the efficiencies of WSDSPETCs by designing and developing better dyes and catalysts for WSDSPAs. Determination of the faradaic efficiencies is also being pursued.

Experimental details

Photoanodes were prepared by spreading TiO_2 nanoparticles on FTO glass by doctor blading. The films were let air-dry, sintered at 450 ºC for 30 minutes, then soaked overnight in a dilute $TiCl_4$ aqueous solution, washed with water, let air-dry and sintered again at 450 C for 30 minutes. After sintering, the electrodes were left to cool down to about 40 ºC and then soak in the corresponding dye, catalyst or dye-catalyst solutions. After absorption of dyes and/or catalyst the electrodes for WSDSPAs were rinsed with water and then let air-dry and the electrodes for DSSCs were rinsed with dichloromethane and the let air-dry in the dark.

WSDSPETCs testing: illumination was obtained using a 450 W xenon arc lamp with added 400 nm long-pass filter (Thorlabs FGL400S). The lamp output was calibrated to 100 mW/cm^2 using a Daystar Solar Meter. Current-Voltage and current-time measurements were obtained using a Keithley 2400 Sourcemeter.

UV–Visible spectroscopy was performed using a Shimadzu UV-2550 UV–Visible spectrophotometer.

CHAPTER 4

COMPUTATIONAL TOOLS FOR MOLECULAR DESIGN

4.1 Simple and accurate correlation of experimental redox potentials and DFT-calculated HOMO/LUMO energies of polycyclic aromatic hydrocarbons.

Citation:

Journal of Molecular Modeling

July 2013, Volume 19, Issue 7, pp 2845-2848

DOI: 10.1007/s00894-012-1694-7

Publisher: Springer-Verlag

Dalvin D. Méndez-Hernández, Pilarisetty Tarakeshwar, Devens Gust, Thomas A. Moore, Ana L. Moore and Vladimiro Mujica

Department of Chemistry and Biochemistry, Arizona State University, Tempe, Arizona 85287-1604

E-mail: ddmendez@asu.edu; tpilaris@asu.edu; gust@asu.edu, tmoore@asu.edu, amoore@asu.edu; vmujica@asu.edu

Abstract: The ability to accurately predict the oxidation and reduction potentials of molecules is very useful in various fields and applications. Quantum mechanical calculations can be used to access this information, yet sometimes the usefulness of these calculations can be limited because of the computational requirements for large systems. Methodologies that yield strong linear correlations between calculations and experimental data have been reported, however the balance between accuracy and computational cost is always a major issue. In this work, linear correlations (with an R^2 value of up to 0.9990) between DFT-calculated HOMO/LUMO energies and seventy redox potentials from a series of fifty-one polycyclic aromatic hydrocarbons (obtained from the literature) are presented. The results are compared to previously reported linear correlations that were obtained with a more expensive computational methodology based on a Born-Haber thermodynamic cycle. It is shown in this article that similar or better correlations can be obtained with a simple and cheaper calculation.

Keywords: HOMO, LUMO, reduction, oxidation, linear correlation

I. Introduction

Determination of the reduction and oxidation potentials of a given molecule at an interface is important in many research areas such as dye sensitized solar cells (DSSC), organic photovoltaics (OPV), and artificial photosynthesis, where tuning the thermodynamic properties of every component of a system is essential for it to work in the desired way[43-48]. The perturbation of the HOMO and LUMO energies (HLE) is also of interest in the context of designing both novel and efficient molecules for harnessing

solar energy in artificial photosynthesis and photocatalysis[45-48]. Ideally one would like to know with accuracy the redox properties of a compound of interest before embarking on an often difficult, expensive and time-consuming synthetic procedure.

The simplest way to rationalize an approximate linear relationship between HLE and oxidation/reduction potentials is to consider the Marcus Relation for interfacial electron transfer

$$\Delta G^{\#} = \frac{\left(\Delta_r G^0 + \lambda\right)^2}{4\lambda} \qquad (\mathbf{1})$$

where $\Delta G^{\#}$ is the free energy of activation and $\Delta_r G^o$ and λ are the reaction free energy and the total reorganization energy, respectively. Solving for $\Delta_r G^0$ in equation (**1**) gives

$$\Delta_r G^0 = \sqrt{4\lambda\Delta G^{\#}} - \lambda \qquad (\mathbf{2})$$

Further we introduced the thermodynamic relation between $\Delta_r G^o$ and the electrochemical cell potential

$$\Delta_r G^0 = -nF(E - E^0) \qquad (\mathbf{3})$$

The reorganization energy is generally decomposed into two contributions, λ_i and λ_0, coming from the molecule and from the solvent, respectively

$$\lambda = \lambda_i + \lambda_o \quad (4)$$

This decomposition leads to the following equation

$$\Delta_r G^0 = \sqrt{4(\lambda_i + \lambda_o)\Delta G^{\#}} - \lambda_o - \lambda_i \quad \textbf{(5)}$$

Up to this point equation (**4**) is formally exact. To proceed, one has to invoke that in many reactions $\lambda_i \ll \lambda_o$[49] and that the first two terms in (**5**) are approximately constant within a family of chemically related molecules, while λ_i is proportional to the energy of the HOMO or the LUMO depending on whether oxidation or reduction is considered[50]. Combining these two approximations and using equations (**3**) and (**5**) leads to the linear relationship

$$E_{OX/RED} = a + b\varepsilon_{HOMO/LUMO} \quad \textbf{(6)}$$

where $E_{OX/RED}$ is the experimental redox potentials, $\varepsilon_{HOMO/LUMO}$ the calculated HLE, and a and b are constants.

Maccoll showed for the first time in 1949 that a good correlation could be obtained between Huckel LUMO energies and experimental reduction potentials[51]. Nevertheless, in the computational electrochemistry literature[52-54], efforts to predict redox potentials steer away from this methodology mainly because of the assumptions involved (e.g.

molecular and solvent reorganization energies are not included in the calculation). Instead, a Born-Haber thermodynamic cycle is preferred as the free energies are directly calculated and solvation energies are accounted for, which are significant as has been observed when electrochemistry is done under different solvents and conditions[55]. Unfortunately, the main drawback for this methodology is that when applied to large molecules (e.g. polycyclic aromatic hydrocarbons (PAHs), porphyrins, phthalocyanines) the computations are very expensive.

To resolve this issue, Fry *et al*. have reported a methodology that accurately predicts the redox potentials of PAHs with a simplified approach to the Born-Haber thermodynamic cycle[34]. This methodology involves the optimization of molecules in both the ground state and the reduced or oxidized state (radical anion or radical cation respectively) with a continuum based solvent model in order to account for reorganization energies. This approach removes the optimization step in the gas phase that is part of the Born-Haber thermodynamic cycle, thus decreasing the number of calculations, from six to three (in order to obtain both oxidation and reduction potentials). This methodology was tested with fifty-one PAHs, whose experimental redox potentials (which were obtained from the literature) were measured under similar conditions. They were able to obtain a very strong correlation, up to $R^2 = 0.9981$, between the calculated and the experimental values.

Before Fry, in 2008, Gillmore *et al.* introduced a further simplified methodology. It consists of a molecular energy optimization in gas phase, followed by a single point calculation in the presence of a continuum solvent model[56]. This increases again the

number of calculations to six (in order to obtain both oxidation and reduction potentials), but the computational time is reduced because four of them (the ones that involve the solvent) are single point calculations. They found a very good correlation between the calculated energy difference and the reduction potentials of quinones, cyanoaromatics and N-metyl heteroaromatic cations[56], and later expanded their methodology to PAHs, flexible aromatic molecules and heterocyclic amines[57].

In searching for a methodology to calculated redox potentials accurately and that is computationally less expensive than Gillmore's approach but at least as accurate as Fry's, reported herein is a good correlation between HLE (calculated at the DFT level using the B3LYP/6-31G(d) functional) and experimental redox potentials. This follows Maccoll's methodology and significantly reduces the complexity of the required calculations. The advantage of this approach is that just one optimization calculation is required, thus it can be applied to large molecules with a relatively low computational cost.

II. Computational method

To test this methodology and compare it to previously reported correlations, the library of PAHs collected by Fry *et al.*[34], which include data from six different references, was used. The literature redox potentials were measured in acetonitrile and are reported in V vs. ferrocene/ferrocenium (Fc/Fc^+), which was used as an internal reference.

All PAHs were optimized using Gaussian09[58] at the B3LYP/6-31G(d) level of theory[59-64] in the gas phase and in the presence of acetonitrile simulated using the Conductor-like

Polarizable Continuum Model (CPCM). The calculated HLE were plotted against the experimental oxidation and reduction potentials respectively.

III. Results

Plots for the calculated HLE of a series of fifty-one PAHs against their experimental oxidation and reduction potentials are shown in **Figure 1** and **2**. When using acetonitrile as the solvent a very strong correlation (R^2=0.9989) is observed between the calculated and experimental values. It is noteworthy that there is also a very strong correlation between HLE and redox potentials when the molecules are optimized in the gas phase (R^2=0.9990). The reason why this is true in this specific case is because solvent reorganization energies are very similar for the set of PAHs under study, resulting in a cancelation of the error obtained by not including the solvent in the calculation. A summary of the results obtained from the method used in this work as well as the results obtained by Fry *et al.* can be found in **Table 1.**

The correlations obtained with the method used in this paper are comparable or better than the ones obtained by Fry. When analyzing the oxidation and reduction potentials together Fry obtained a mean absolute deviation (MAD) of 0.056 V while we get a MAD of 0.046 V. When the data is split in two sets (only reduction or oxidation potentials), Fry's correlation is better than ours for both reductions and oxidations, but the error is of the same order of magnitude for both approaches. In general, both methods are in very good agreement with the experimental values, our method having the advantage that it consists of only one optimization rather than three.

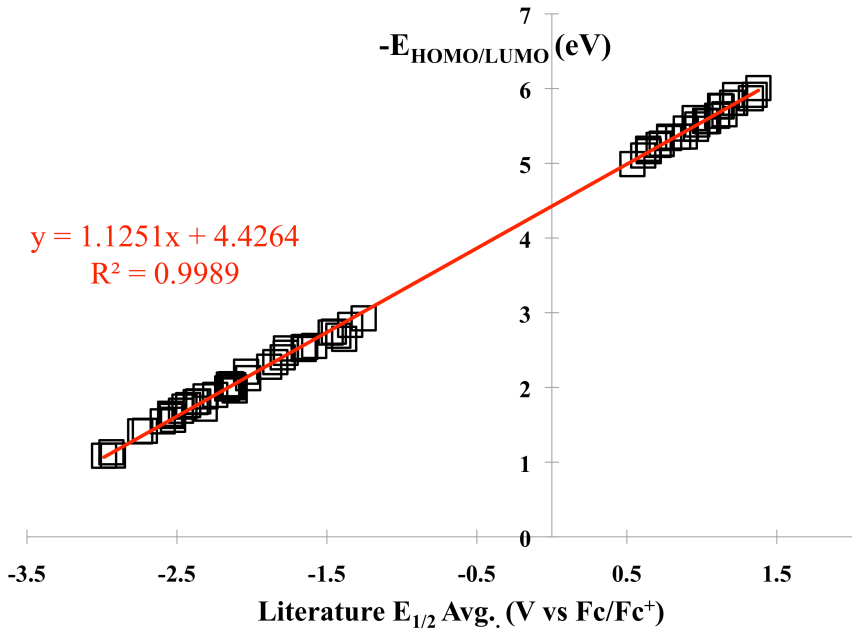

Figure 1. Plot of experimental $E_{1/2}$ avg. obtained from [14] and references therein vs. computed HOMO/LUMO energies (eV) using acetonitrile as the solvent.

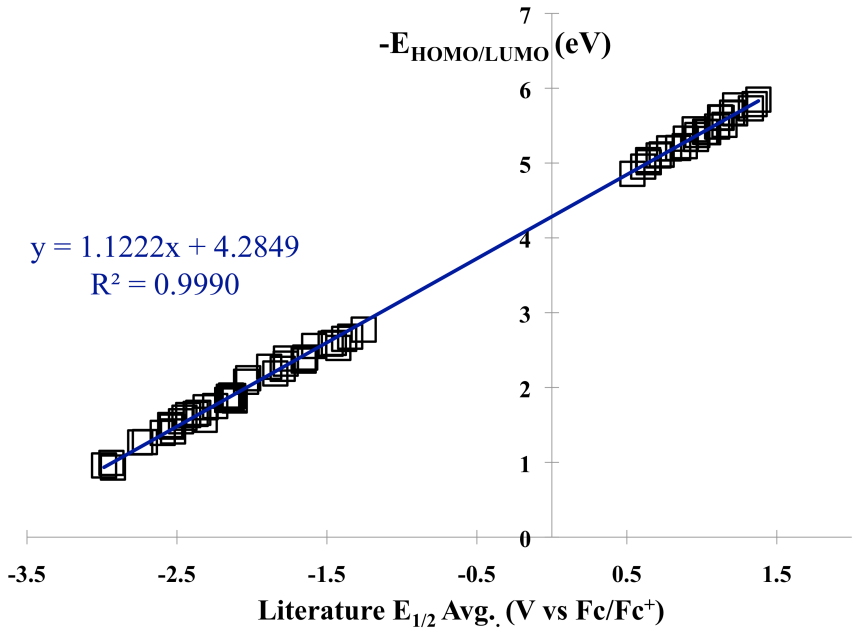

Figure 2. Plot of experimental $E_{1/2}$ avg. obtained from [14] and references therein vs. computed HOMO/LUMO energies (eV) in the gas phase.

This work		**slope *a* (eV/V)**	**y-intercept *b* (eV)**	**R^2**	**MAD (eV)**	**RMSD[a] (eV)**	**x-intercept[b] (V)**
acetonitrile	All	1.1251	4.4264	0.9989	0.046	0.058	-3.93
	Oxidation	1.1288	4.4311	0.9700	0.037	0.047	-3.93
	Reduction	1.0444	4.2499	0.9882	0.039	0.053	-4.07
gas phase	All	1.1222	4.2849	0.9990	0.046	0.056	-3.82
	Oxidation	1.1318	4.2813	0.9740	0.035	0.043	-3.78
	Reduction	1.0658	4.1616	0.9864	0.044	0.058	-3.90
Reference [14]							
	All	0.8591	4.442	0.9981	0.056	---	-5.17
	Oxidation	1.073	4.227	0.9847	0.032	---	-3.94
	Reduction	0.947	4.64	0.9924	0.023	---	-4.90

Table 1. Summary of the results from the linear correlations. a) Root-mean-square deviation b) calculated with x-intercept = $-b/a$.

IV. Conclusions

A very strong linear correlation of DFT-calculated HLE and redox potentials of PAHs is shown. It is important to emphasize that only one optimization calculation per molecule is required to obtain both HLEs. In contrast, at least three (and up to six) optimizations per molecule are required to obtain a theoretical approximation of the potentials by the other methods described above. This can be a powerful tool to use when one needs to quickly and accurately predict oxidation and reduction potentials of new compounds given that one have a series of similar compounds whose redox potential are already known.

The strong correlation obtained from HLE and redox potentials of PAHs was independent of whether the solvent model was included in the calculations. This may not be the case when including in the correlation other groups of molecules that have different solvent reorganization energies. For future work this methodology will be extended to quinones, cyanoaromatics, porphyrins, phthalocyanines and perylenes.

V. Acknowledgements

We would like to thank Dr. Jason G. Gillmore for very useful discussions and suggestions. Thanks to John J. Tomlin and all the members of the Gust-Moore-Moore research group for inspirational conversations.

DDMH is supported by the National Science Foundation Graduate Research Fellowship Program (NSF-GRFP) under Grant No. DGE-0802261 and by the More Graduate Education at Mountain States Alliance (MGE@MSA) Alliance for Graduate Education and the Professoriate (AGEP) National Science Foundation (NSF) Cooperative Agreement No. HRD-0450137.

This work was supported as part of the Center for Bio-Inspired Solar Fuel Production, an Energy Frontier Research Center funded by the U.S. Department of Energy, Office of Science, Office of Basic Energy Sciences under Award Number DE-SC0001016.

Calculations were performed using the ASU Advance Computer Center Saguaro system.

4.2 Building and Testing Correlations for the Estimation of One-electron Reduction Potentials of a Broad Range of Organic Molecules.

Manuscript submitted for publication.

Dalvin D. Méndez-Hernández*,[1] Jason G. Gillmore*,[1,2] Luis A. Montano,[1] Devens Gust,[1] Thomas A. Moore,[1] Ana L. Moore,[1] and Vladimiro Mujica[1]

1) Center for Bio-Inspired Solar Fuel Production, Department of Chemistry and Biochemistry, Arizona State University, Tempe, Arizona 85287-1604

2) Department of Chemistry, Hope College, 35 E. 12th Street, Holland, Michigan 49423

*Authors to whom correspondence should be addressed.

E-mail: ddmendez@asu.edu; gillmore@hope.edu

TOC Graphic / Graphical Abstract

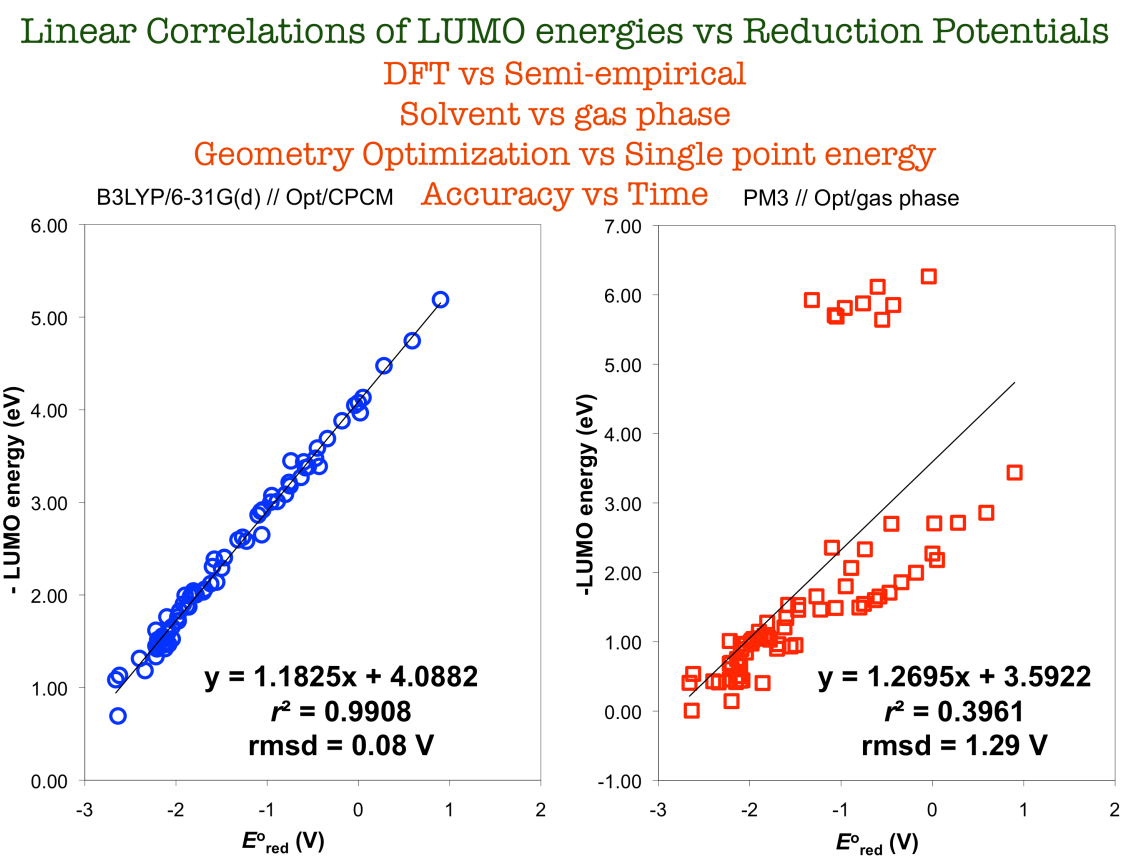

Abstract

We expand upon the computational methodology of linearly correlating calculated frontier molecular orbital energies to ground state redox potentials. A wide range of molecules (74 compounds belonging to six different families) was used to build the correlations between their experimental reduction potential and their calculated LUMO energy. These compounds are important in electrochemically active systems of relevance to a variety of materials and in energy applications including photovoltaic cells and solar fuels generation. This methodology is computationally inexpensive compared with other approaches and it permits the prediction of redox potentials of molecules not

included in the families used to determine the correlation parameters. The effects of varying the level of theory used in the electronic structure calculation and the including a solvent compared to calculations in gas phase were also examined. Some of the best correlations were tested to predict the reduction potentials of seven structurally diverse chromophores that were not included in the correlation data set.

Introduction

Computational chemistry has become an invaluable tool that can used in concert with experiment to enable experimental chemists to identify targets and minimize time and material expenses in numerous areas of research.[43-45,47,48,65-70]Testing large families of molecules for a specific property often proves impractical and very expensive in the laboratory, but under certain approximations can become a fruitful exercise in computational chemistry. In this context, the role of theory is to construct models that allow the evaluation of the relevant properties and provide guidance to experimentalists. The ability to predict the first redox potentials of the compounds is very useful when designing new molecules intended to participate in charge transfer reactions. State-of-the-art calculations to estimate redox potentials using the Born-Haber cycle[34,35,48,66,67,71-75] involve substantial computational work because of multiple open-shell electronic structure optimizations where the molecules are radical anions or cations. These open-shell calculations can be computationally expensive especially for large molecules. In previous work[9,56,57] the Gillmore group has explored the accuracy of this type of calculation using a simplified version of the Born-Haber cycle where the geometry optimizations of the structures (singlet and radical anion) were performed in the gas

phase, followed by a single point energy calculation of each structure in the presence of a continuum solvent model. This simplified method did not specifically calculate a reduction potential, but something more akin to an electron affinity (albeit in solution). The method reduces computational cost by avoiding geometry optimization in the presence of a continuum solvent model and results in strong correlations between experimentally measured reduction potentials and the calculated energy difference between the molecule and its one-electron reduced product. With proper calibration with known compounds, good predictive abilities were achieved.

As an alternative to the Born-Haber cycle methods, linear relationships between molecular orbital energies and the ability of a molecule to accept or donate electron are among the earliest relationships that were considered in the literature.[15-17,19,20,29,30,51,76] The use of a linear correlation of HOMO-LUMO energies of the singlet ground state molecules with their experimentally measured redox potentials is an even simpler way to estimate the redox potentials of unknown molecules starting from theoretical calculations.[32,33,43-48,77-90] The advantage of this approach is that, in principle, only a single geometry optimization of the molecule of interest in the singlet state is required to predict both the experimental first one-electron reduction and oxidation potentials.

In our recent work,[33,43-48,65-70] this strategy was tested with fifty-one polycyclic aromatic hydrocarbons (PAHs) of known oxidation and/or reduction potentials measured in acetonitrile. With the purpose of expanding this methodology and verifying its applicability to a much broader range of structurally diverse organic molecules, in this contribution we examine the effects of varying the level of the theoretical description and the inclusion of a dielectric solvent model on the accuracy of linear correlations between

calculated LUMO energies and the reduction potential of PAHs and five other families of compounds for a total of seventy-four structurally and functionally diverse molecules (Table 1) over a range of 3.5 V. The resulting correlations were used to accurately predict experimental reduction potentials of additional molecules not used in the calibration and determinations of the correlation parameters.

Table 1. List of compounds (by family), and their experimental reduction potentials,[34,35,49,57,66,67,71-75,91] used to build correlations 1-24.

Family/compound number	Compound name	Reduction potential (V vs SCE)
Cyanoaromatics		
1	tetramethyl-*p*-dicyanobenzene	-1.9
2	*p*-dicyanobenzene	-1.6
3	tetrafluoro-*p*-dicyanobenzene	-1.1
4	tetrachloro-*p*-dicyanobenzene	-0.95
5	1,2,4,5-tetracyanobenzene	-0.74
6	2-cyanonaphthalene	-1.98
7	1-cyano-4-methylnaphthalene	-1.96
8	1-cyanonaphthalene	-1.88
9	1,4-dicyanonaphthalene	-1.27
10	9-cyanoanthracene	-1.58
11	9-cyano-10-phenylanthracene	-1.47
12	9,10-dicyanoanthracene	-0.89
13	3,7,9,10-tetracyanoanthracene	-0.45
Quinones		
14	tetramethyl-*p*-quinone	-0.8
15	trimethyl-*p*-quinone	-0.75
16	2,6-dimethyl-*p*-quinone	-0.63

17	2-methyl-*p*-quinone	-0.58
18	*p*-quinone	-0.47
19	2-chloro-*p*-quinone	-0.34
20	2,6-dichloro-*p*-quinone	-0.18
21	tetrabromo-*p*-quinone	0
22	tetrafluoro-*p*-quinone	0.02
23	tetrachloro-*p*-quinone	0.05
24	2,3-dicyano-*p*-quinone	0.28
25	5,6-dichloro-2,3-dicyano-*p*-quinone	0.59
26	tetracyano-*p*-quinone	0.9
_N_-Methyl Heteroaromatic Cations		
27	*N*-methylpyridinium	-1.32
28	4-methyl-*N*-methylquinolinium	-1.07
29	2-methyl-*N*-methylquinolinium	-1.05
30	*N*-methylquinolinium	-0.96
31	3-bromo-*N*-methylquinolinium	-0.76
32	3-cyano-*N*-methylquinolinium	-0.6
33	9-phenyl-*N*-methylacridinium	-0.55
34	*N*-methylacridinium	-0.43
35	9-cyano-*N*-methylacridinium	-0.04
Flexible Pi Molecules		
36	diethyl fumarate	-1.5
37	diethyl terephthalate	-1.78
38	benzophenone	-1.86
39	acetophenone	-2.1
40	propiophenone	-2.15
41	*trans*-stilbene	-2.2
42	4-methylacetophenone	-2.2

43	methyl benzoate	-2.22
44	ethyl benzoate	-2.4
Polycyclic Aromatic Hydrocarbons		
45	naphthalene	-2.66
46	acenaphthylene	-1.8
47	cyclopent[fg]acenaphthylene	-1.06
48	anthracene	-2.1
49	phenanthrene	-2.62
50	aceanthrylene	-1.47
51	acephenanthrylene	-1.81
52	fluoranthene	-1.92
53	pyrene	-2.22
54	benzo[ghi]fluoranthene	-1.84
55	dibenzo[ghi,mno]fluoranthene	-1.99
56	perylene	-1.81
Heterocyclic amines		
57	benzo[c]cinnoline	-1.554
58	cinnoline	-1.686
59	phthalazine	-1.976
60	phenanthridine	-2.118
61	pyridazine	-2.12
62	pyrimidine	-2.34
63	benzo[f]quinoline	-2.14
64	benzo[h]quinoline	-2.208
65	isoquinoline	-2.22
66	*o*-phenanthroline	-2.042
67	*m*-phenanthroline	-2.092
68	*p*-phenanthroline	-2.044
69	pyridine	-2.636

70	quinoline	-2.105
71	acridine	-1.62
72	pyrazine	-2.08
73	phenazine	-1.227
74	quinoxaline	-1.702

Results and discussion

Linear correlations were constructed by plotting the negative of the calculated LUMO energy (eV) of each molecule as a function of its corresponding experimental reduction potential (V vs SCE) measured in acetonitrile. The LUMO energies were obtained by three different means: 1) a geometry optimization of the molecules in the gas phase alone, followed by 2) a single point energy calculation in the presence of the solvent, or 3) a geometry optimization in the presence of the solvent. These calculations were performed at four different levels of theory. A summary of the resulting parameters for the correlations studied can be found in Tables 2 and 3.

Table 2. Correlations of Calculated LUMO Energies with Experimental Reduction Potentials for Compounds 1−74, Varying Computational Methodology.

[a]Opt = optimization, Sp = single point, gas = gas phase calculations, CPCM = calculation using the Conductor-like Polarizable Continuum Model. [b]Root mean square deviation, taken from individual residuals for each compound as predicted by each trend line (as reported in the Supporting Information). [c]Mean average deviation, taken from individual residuals for each compound as predicted by each trend line (as reported in the Supporting Information).

Corr. #	Method/ basis set	Calculation type/ solvent model[a]	slope *m* (eV/V)	*y*-intercept *b* (eV)	r^2	rmsd[b] residuals (V)	MAD[c] residuals (V)	*x*-intercept (V)
1	B3LYP/ 6-31G(d)	Opt/gas	1.7213	5.2616	0.6276	0.6333	0.3985	-3.0568
2	B3LYP/ 6-311+G(2d,p)	Opt/gas	1.6615	5.5212	0.6277	0.6331	0.3967	-3.3230
3	Semi-empirical PM3	Opt/gas	1.2695	3.5922	0.3961	1.2887	0.8120	-2.8296
4	Semi-empirical PM6	Opt/gas	1.3448	3.7973	0.4918	1.1124	0.7110	-2.8237
5	B3LYP/ 6-31G(d)	Sp/CPCM	1.1844	4.0873	0.9903	0.0815	0.0644	-3.4509
6	B3LYP/ 6-311+G(2d,p)	Sp/CPCM	1.1291	4.3340	0.9917	0.0753	0.0579	-3.8385
7	Semi-empirical PM3	Sp/CPCM	0.7160	2.3999	0.8246	0.2715	0.2292	-3.3518
8	Semi-empirical PM6	Sp/CPCM	0.7988	2.6775	0.9404	0.1653	0.1318	-3.3519
9	B3LYP/ 6-31G(d)	Opt/CPCM	1.1825	4.0882	0.9908	0.0791	0.0614	-3.4573
10	B3LYP/ 6-311+G(2d,p)	Opt/CPCM	1.1275	4.3372	0.9918	0.0749	0.0589	-3.8467
11	Semi-empirical PM3	Opt/CPCM	0.7163	2.4012	0.8285	0.2680	0.2253	-3.3522
12	Semi-empirical PM6	Opt/CPCM	0.8004	2.6826	0.9427	0.1623	0.1282	-3.3516

Table 3. Correlations of Calculated LUMO Energies with Experimental Reduction Potentials for Compounds 1−26 and 36-74 (Excluding the *N*-Methyl Heteroaromatic Cations family 27-35) Varying Computational Methodology.

[a]Opt = optimization, Sp = single point, gas = gas phase calculations, CPCM = calculation using the Conductor-like Polarizable Continuum Model. [b]Root mean square deviation, taken from individual residuals for each compound as predicted by each trend line (as reported in the Supporting Information). [c]Mean average deviation, taken from individual residuals for each compound as predicted by each trend line (as reported in the Supporting Information).

Corr. #	Method	Calculation type/ solvent model[a]	slope *m* (eV/V)	*y*-intercept *b* (eV)	r^2	rmsd[b] residuals (V)	MAD[c] residuals (V)	*x*-intercept (V)
13	B3LYP/ 6-31G(d)	Opt/gas	1.3415	4.3129	0.9776	0.1252	0.0935	-3.2150
14	B3LYP/ 6-311+G(2d,p)	Opt/gas	1.2947	4.6055	0.9748	0.1330	0.0994	-3.5572
15	Semi-empirical PM3	Opt/gas	0.8086	3.4539	0.8640	0.2652	0.2173	-3.0348
16	Semi-empirical PM6	Opt/gas	0.9462	2.8105	0.9173	0.2348	0.1789	-2.9703
17	B3LYP/ 6-31G(d)	Sp/CPCM	1.1837	4.0825	0.9901	0.0826	0.0641	-3.4489
18	B3LYP/ 6-311+G(2d,p)	Sp/CPCM	1.1399	4.3583	0.9923	0.0729	0.0580	-3.8234
19	Semi-empirical PM3	Sp/CPCM	0.6531	2.2524	0.8377	0.2376	0.1945	-3.4488
20	Semi-empirical PM6	Sp/CPCM	0.7869	2.6540	0.9344	0.1724	0.1390	-3.3727
21	B3LYP/ 6-31G(d)	Opt/CPCM	1.1840	4.0887	0.9907	0.0801	0.0618	-3.4533
22	B3LYP/ 6-311+G(2d,p)	Opt/CPCM	1.1411	4.3679	0.9928	0.0702	0.0559	-3.8278
23	Semi-empirical PM3	Opt/CPCM	0.6567	2.2612	0.8378	0.2388	0.1833	-3.4433
24	Semi-empirical PM6	Opt/CPCM	0.7911	2.6651	0.9367	0.1700	0.1360	-3.3689

For the correlations that include all seventy-four compounds (Table 1), the correlations obtained from purely gas phase geometry optimizations (1-4) resulted in very low r^2, whereas when the solvent was included either in a single point energy calculation (5-8) or a full geometry optimization (9-12) the r^2 approached the optimal value of 1. This is due primarily to underestimation of the LUMO energies for the *N*-methyl heteroaromatic cations family calculated in the gas phase. Figure 1 illustrates some of the correlations from Table 2.

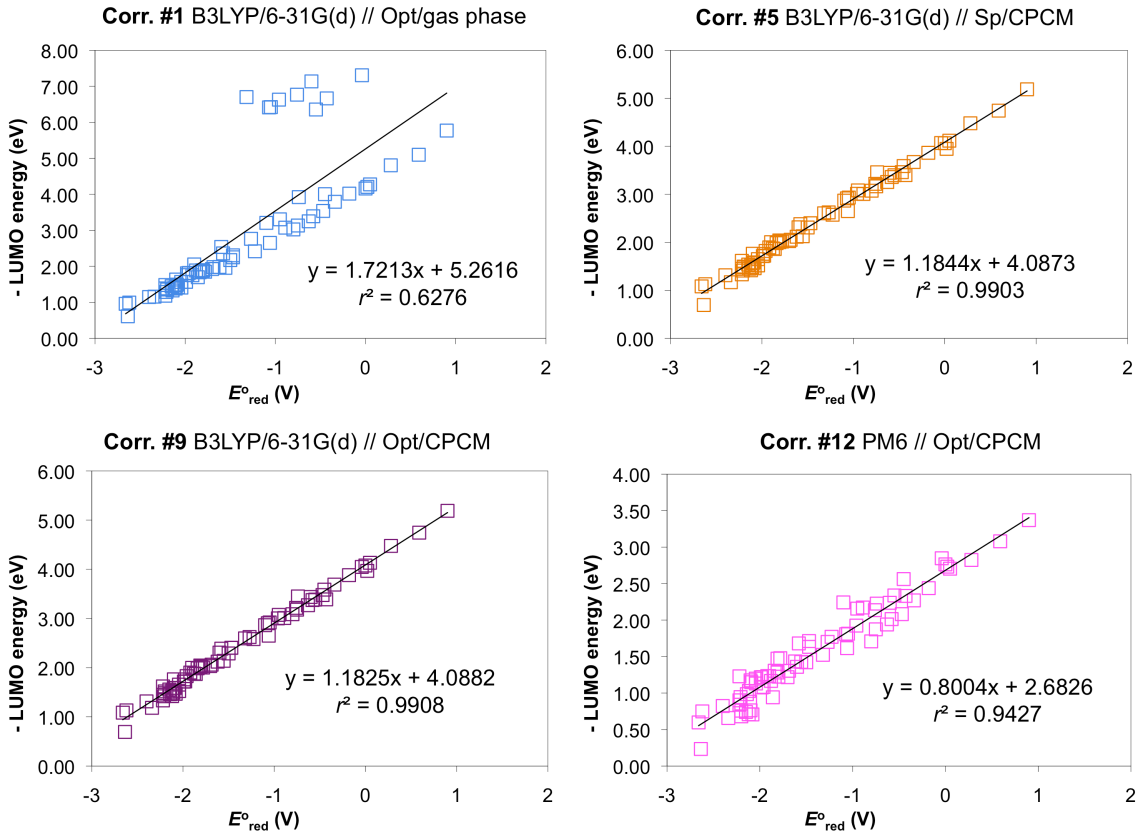

Figure 1. Plots of Selected Correlations from Table 2.

In order to fairly compare the three approaches, the correlations were built with only sixty-three of the seventy-four compounds by omitting the *N*-methyl heteroaromatic cations, and the results are shown in Table 3. As expected, the r^2 improved for all the correlations in Table 3 (13-24) when compared to the correlations in Table 2 (1-12), especially for correlations based upon gas phase energies (13-16 vs. 1-4). As with correlations 1-12, the r^2 for correlations 13-24 increased when the solvent was included either in a single point energy calculation (17-20) or a full geometry optimization (21-24). It was also observed that the rmsd for individual families was in general a little better than for the global correlations (see Supporting Information).

Intercept of *x*-axis

The correlations in Tables 2 and 3 were built with the experimental reduction potentials on the *x*-axis because this was the control variable and also to keep consistency with our previous work.[33,43-45,47,48,50,56,57,65-70] In the Gillmore group's prior methodology, the energy difference between the ground and one-electron reduced states was used as an analog to an electron affinity in a dielectric continuum rather than the gas phase. Thus to the extent that this was equivalent to a reduction potential, the slope should have approached unity and the *x*-intercept the reference potential of the SCE reference electrode relative to which the literature reduction potentials were reported. Even in this previous (more computationally expensive) methodology, deviation from both a slope of 1.0 and an *x*-intercept of -4.12 V was observed in the best predictive correlations, indicative of the fitting parameters accommodating systemic error while preserving good correlation and accurate predictive ability. In the present work, we move yet further from this equivalence to reduction potential to make gains in both predictive ability and

computational efficiency, and the slope and *x*-intercepts diverge yet further while MAD, rmsd, and r^2 all continue to improve and computation time decreases. This is not a concern but rather indicative of the gains in both efficiency and accuracy that simply highlight the advantages of our correlation methodology over strictly trying to compute an actual reduction potential.

Testing the correlations

After building the correlations 1-24, some of the best correlations were tested to see how well they would predict the reduction potential of seven additional compounds that were not included in the correlations data set, in order to provide a true test of the predicting ability of the methodology: two perimidinespirohexadienone (PSHD) photochromes and their long-wavelength quinonimine isomers (**75-78**)[34,35,51,57,66,67,71-75,91], and three perylene dianhydrides (**79-81**)[52-54,56,57,92]. These compounds are examples of chromophores our groups have previously explored as potential photo-induced charge transfer initiators.

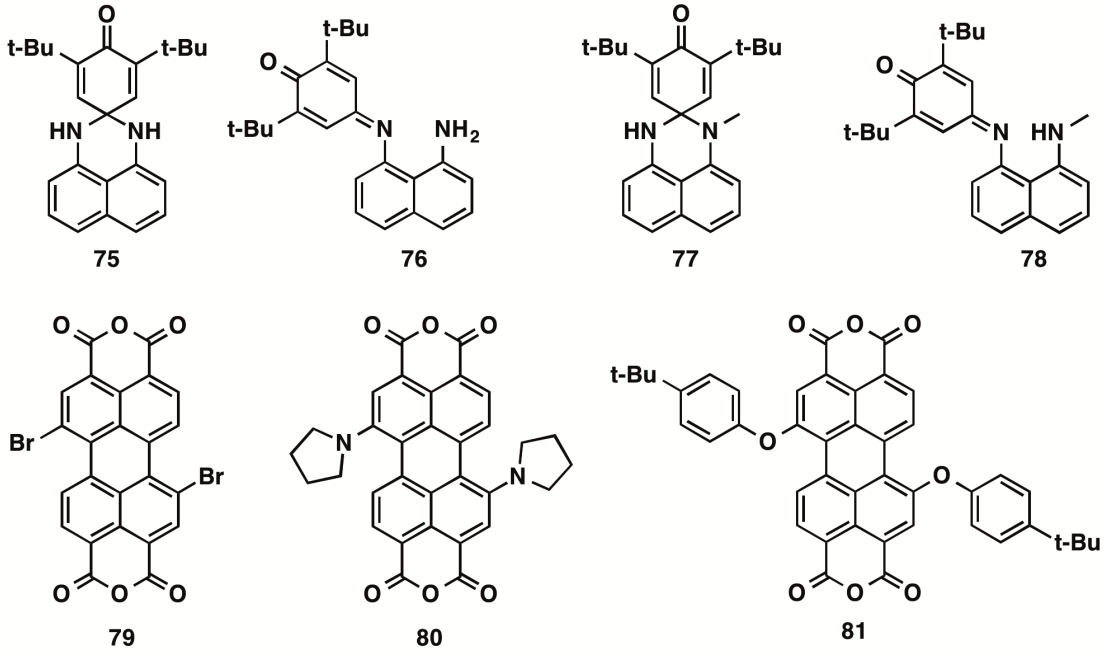

It can be seen from both Tables 2 and 3 that correlations performed with density functional theory (DFT) resulted in an improved r^2 and in a lower rmsd and MAD than the correlations performed with semi-empirical methods. Therefore, only the DFT correlations were tested further with molecules **75-81**. Table 4 shows the reduction potentials calculated by linear extrapolation from the DFT correlations for these seven compounds. In general, correlations and 6 and 9 yielded better results (~ 10 mV lower rmsd) than correlation 5. Therefore, geometry optimization in the presence of the solvent or using a higher-level basis set seems to be modestly beneficial, but would results on an increase of the overall computation time. Correlation 10 yielded only similar rmsd to correlations 6 and 9, while being a more expensive calculation by involving both geometry optimization in the presence of the solvent and the use of a higher-level basis set.

Table 4. Comparison of Experimental Reduction Potentials of Four PSHD Photochromes and Two Perylenes to Those Predicted Using Selected Correlations.

[a]Root mean square deviation, taken from individual residuals for each compound as predicted by each trend line (as reported in the Supporting Information). [b]Mean average deviation, taken from individual residuals for each compound as predicted by each trend line (as reported in the Supporting Information).

Compound	Exptl E^{o}_{red} (V vs SCE)	Predicted E^{o}_{red} (V vs SCE)			
		Corr. 5	Corr. 6	Corr. 9	Corr. 10
75	-1.74	-1.69	-1.76	-1.68	-1.77
76	-0.94	-0.89	-0.96	-0.89	-0.97
77	-1.68	-1.68	-1.76	-1.67	-1.77
78	-0.94	-0.89	-0.95	-0.89	-0.97
79	-0.25	-0.33	-0.32	-0.30	-0.28
80	-0.72	-0.78	-0.78	-0.77	-0.75
81	-0.51	-0.55	-0.54	-0.53	-0.51
rmsd[a]	-	0.05	0.04	0.04	0.04
MAD[b]	-	0.05	0.04	0.04	0.03

Correlations with all 81 compounds

The correlations of the experimental one-electron reduction potential of all eighty-one compounds with their calculated LUMO energy determined with different methodologies are shown in Table 5. It is important to note that for the correlations on this table the axes have been switch by plotting experimental reduction (V vs SCE) vs. LUMO energies (eV), thus transposing the x- and y-axes of our correlations, as the predicted redox potential is now the value of interest. These correlations (25-28) are illustrated in Figure 2.

Corr. #	Method	Calculation type/ solvent model[a]	slope *m* (V/eV)	*y*-intercept *b* (V)	r^2	rmsd[b] residuals (V)	MAD[c] residuals (V)

Table 5. Correlations of Experimental Reduction Potential with calculated LUMO Energies for Compounds 1−81, Varying Computational Methodology.

25	B3LYP/ 6-31G(d)	Sp/CPCM	0.8386	-3.4364	0.9905	0.0791	0.0628
26	B3LYP/ 6-311+G(2d,p)	Sp/CPCM	0.8807	-3.8209	0.9919	0.0731	0.0562
27	B3LYP/ 6-31G(d)	Opt/CPCM	0.8395	-3.4426	0.9911	0.0764	0.0594
28	B3LYP/ 6-311+G(2d,p)	Opt/CPCM	0.8805	-3.8263	0.9921	0.0722	0.0562

[a]Opt = optimization, Sp = single point, gas = gas phase calculations, CPCM = calculation using the Conductor-like Polarizable Continuum Model. [b]Root mean square deviation, taken from individual residuals for each compound as predicted by each trend line (as reported in the Supporting Information). [c]Mean average deviation, taken from individual residuals for each compound as predicted by each trend line (as reported in the Supporting Information).

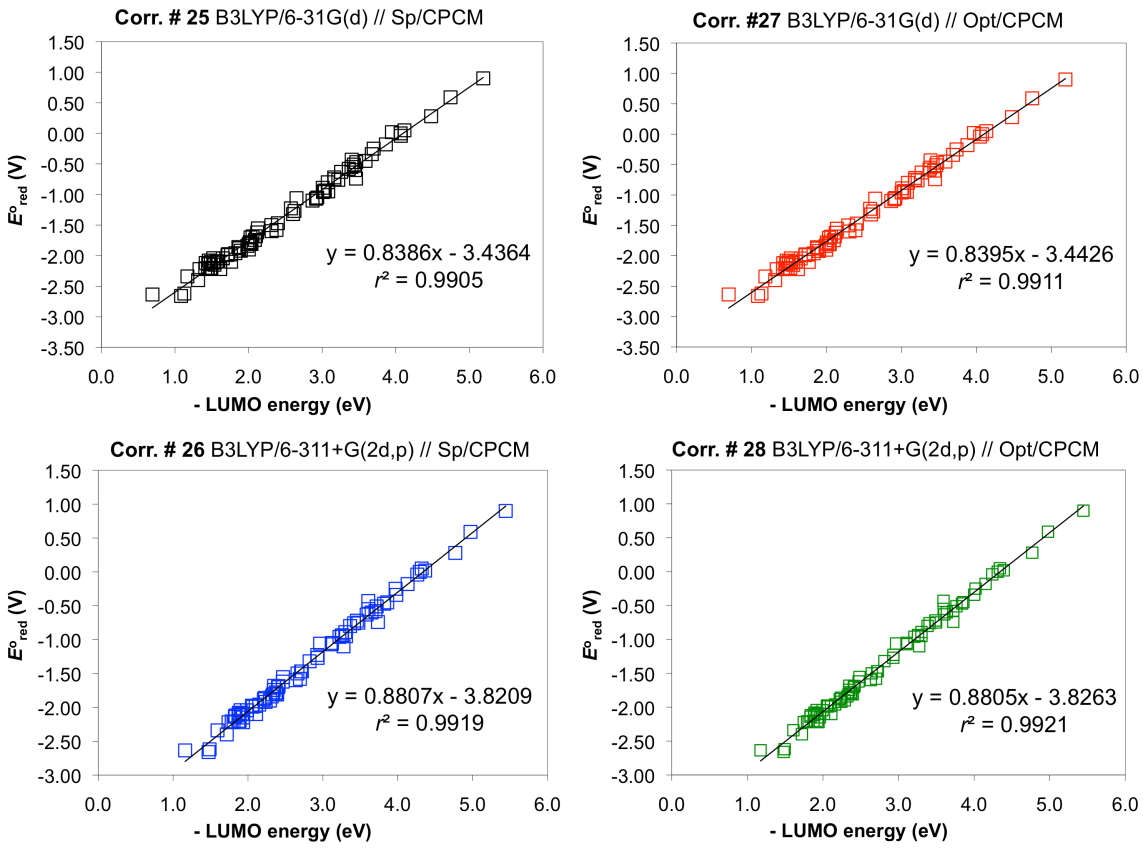

Figure 2. Plots of Selected Correlation from Table 5.

Conclusions

We have shown that a strong linear correlation between computed LUMO energies and experimental reduction potentials can be obtained for a large series of diverse organic compounds with very different structures and substituents spanning a range of more than 3.5 V of reduction potentials. Among all the correlations established employing varying levels of theory, the ones that involved DFT calculations resulted in better correlations than the less computer intensive semi-empirical methods. The presence of a solvent model in the calculations (either in the full geometry optimization, or as a single point calculation on the gas-phase optimized geometries) significantly improved the quality of correlation resulting in lower rmsd values than for the gas phase correlations. This was particularly true when the *N*-methyl heteroaromatic cations were included in the correlations (1-12).

The main drawback of this methodology is the need to construct a linear correlation previous to being able to make predictions. However the correlations (25-28) reported herein appear sufficiently robust to allow prediction of the first reduction potential of molecules structurally and functionally distinct from those used to calibrate the correlation, including those like the PSHDs that do not neatly fit into any of the typical families of structures. Additional benchmark correlations in different solvents or based upon different families of compounds can be developed by individual users or by the broader community, as there is need or interest. These will of course depend on the availability (or measurement) of appropriate experimental redox potential data for those compounds in those solvents.

A comparison of the best correlation that includes all seventy-four compounds from Gillmore's previous work (r^2 = 0.9889, rmsd = 0.0829 V) with the best correlation from this work (r^2 = 0.9918, rmsd = 0.0749 V) shows a slight improvement. As mentioned in the Introduction, the main advantage of the methodology used in this work is that it requires only closed-shell calculations reducing the number of calculations required, while prior work required gas-phase geometry optimizations of two different species, and then their single point energies with solvent. The present work can be completed with a single geometry optimization (with or without solvent), and the energy of the gas-phase geometry can be improved by a single point energy calculation with solvent. Based on our results, performing gas phase optimizations followed by single point energy calculations in the presence of a continuum solvent model is recommended for a good balance of accuracy and calculation time when building MO-redox correlations. The methodology studied in this work is useful for predicting reduction potentials when designing new molecules, and is computationally less expensive than Gillmore's previous method.[51,55-57,76] Moreover, based on our prior work,[32-34,77-90] it is expected that this approach should be generalizable to correlations of HOMO energies to oxidation potentials. Future work in our group will include using the present correlations to predict reduction potentials of porphyrins and phthalocyanines, as well as developing additional correlations in different solvents and with additional calibration molecules (perhaps including porphyrins and phthalocyanines) as well as of correlations of HOMO energies with oxidation potentials.

Computational Methodology

A series of seventy-four compounds (listed on the SI) were submitted to the following procedure:

1) Geometry optimization in gas phase (Corr. 1-4 and 13-16), followed by
2) Single point energy calculation in solvent model (Corr. 5-8 and 17-20) or
3) Geometry optimization in solvent model (Corr. 9-12 and 21-24)

Four different computational levels of theory were tested:

1) DFT: [33,56,59,62,63,93,94]
    a. B3LYP/6-31G(d)
    b. B3LYP/6-311+G(2d,p)
2) Semi-empirical: [56,57,95-97]
    a. PM-3
    b. PM-6

All compounds were geometry optimized using *Gaussian 09*.[57,58] For the calculations that involved the presence of solvent (acetonitrile) the Conductor-like Polarizable Continuum Model (CPCM)[34,98,99] was used. The calculated LUMO energy for each molecule was plotted against the experimental one-electron reduction potential. The experimental reduction potentials were taken from the literature[57,58]. The literature potentials were measured in acetonitrile and are reported in V vs. SCE, after correction from other reference electrodes if need be.

Supporting Information

An Excel workbook with separate tabbed worksheets for each basis set and methodology combination, providing additional graphs and correlations by family of molecules as well

as all correlations reported herein, and including complete data of the individual computed LUMO energies for each molecule at each level of theory, along with the literature reduction potentials to which they were correlated and a separate document with the Cartesian coordinates of molecules 1-81 optimized at the B3LYP/6-311+G(2d,p) level of theory using CPCM to simulate acetonitrile. This material is available free of charge via the Internet at http://pubs.acs.org.

Acknowledgements

This work was supported as part of the Center for Bio-Inspired Solar Fuel Production, an Energy Frontier Research Center funded by the U.S. Department of Energy, Office of Science, Office of Basic Energy Sciences under Award Number DE-SC0001016. Calculations were performed using the ASU Advance Computer Center Saguaro system. DDMH was supported by the National Science Foundation Graduate Research Fellowship Program (NSF-GRFP) under Grant No. DGE-0802261 and by the More Graduate Education at Mountain States Alliance (MGE@MSA) Alliance for Graduate Education and the Professoriate (AGEP) National Science Foundation (NSF) Cooperative Agreement No. HRD-0450137. JGG was supported by NSF CAREER CHE-0952768 and LAM was supported by the Western Alliance to Expand Student Opportunities (WAESO) Louis Stokes Alliance for Minority Participation (LSAMP) National Science Foundation (NSF) Cooperative Agreement No. HRD-1101728.

CHAPTER 5

ELECTRON PARAMAGNETIC RESONANCE CALCULATIONS

5.1 A bioinspired redox relay that mimics radical interactions of the Tyr-His pairs of photosystem II

Citation:

Nature Chemistry

Advance online publication

Published online on February 9, 2014

DOI: 10.1038/nchem.1862

Publisher: Nature Publishing Group

Jackson D. Megiatto, Jr.[1#], Dalvin D. Méndez-Hernández[1], Marely E. Tejeda-Ferrari[1], Anne-Lucie Teillout[1,3], Manuel J. Llansola Portolés[1], Gerdenis Kodis[1], Oleg G. Poluektov[2]*, Tijana Rajh[2]*, Vladimiro Mujica[1], Thomas L. Groy[1], Devens Gust[1]*, Thomas A. Moore[1]* and Ana L. Moore[1]*

[1]Department of Chemistry and Biochemistry, Arizona State University, Tempe, AZ 85287-1604, USA E-mail: tmoore@asu.edu ; gust@asu.edu ; amoore@asu.edu

[2] NanoBio Interface Group, Center for Nanoscale Materials and Chemistry Division, Argonne National Laboratory Argonne, IL 60439, USA E-mail: rajh@anl.gov; oleg@anl.gov

[3] Laboratoire de Chimie Physique, Groupe d'Electrochimie et de Photoélectrochimie, UMR 8000, CNRS, Université Paris-Sud, Batiment 350, 91405 Orsay Cedex, France.

Current address: Institute of Chemistry, Campinas State University (UNICAMP), P.O. Box 6154, Campinas, SP, 13084-861, Brazil.

In water oxidizing photosynthetic organisms light absorption generates a powerfully oxidizing chlorophyll complex ($P680^{\bullet+}$) in the photosystem II (PSII) reaction center. In all known cases, the pathway for electron transfer from the water oxidizing catalyst to $P680^{\bullet+}$ includes an electron transfer relay comprising a tyrosine (Tyr) / histidine (His) pair with a short phenol to imidazole group H-bond. By rapidly reducing $P680^{\bullet+}$, the relay probably mitigates recombination reactions thereby ensuring a high quantum yield of water oxidation. Here we show that in artificial reaction centers equipped with a benzimidazole-phenol (BiP) model of the Tyr/His pair, the artificial relay mimics the short internal H-bond and the relaxation observed by EPR accompanying proton coupled electron transfer (PCET) in PSII. This artificial system is much less complex than the natural one and theory suggests that it captures the essential features that are important in the function of the relay.

Photosystem II (PSII), the enzyme that uses sunlight to oxidize water to molecular oxygen, contains two redox-active tyrosines called Tyrosine Z (Tyr_Z) and Tyrosine D (Tyr_D) that are located in positions related by approximately 2-fold rotational symmetry in the D1 and D2 core proteins, respectively.[38,59-64,100,101] According to the recent PSII crystal structure,[38,43-45,47,48,65-70] Tyr_D is located in a relatively hydrophobic domain with its phenolic proton forming a short hydrogen bond with the imidazole nitrogen atom of a nearby histidine, D2-His189. In contrast, Tyr_Z is in a more hydrophilic environment,

forming an even shorter hydrogen bond with the corresponding D1-His190. Photo-oxidation of both tyrosines during PSII activity is coupled to the transfer of their phenolic protons, most likely to their respective hydrogen bonded histidine partners. The resulting neutral tyrosyl radicals $Tyr_Z^{\bullet}$ and $Tyr_D^{\bullet}$ have different functional roles in the enzyme. $Tyr_Z^{\bullet}$ is directly involved in the water oxidation process, while $Tyr_D^{\bullet}$ is not.[34,35,48,66,67,71-75,102-108]

Because of the extraordinarily long lifetime (several hours under some conditions) of $Tyr_D^{\bullet}$ radical it has been possible to study it by a number of techniques.[37,109-112] Using high field electron paramagnetic resonance Faller *et al.* demonstrated[37] that oxidation of Tyr_D in OEC-depleted PSII reaction centers occurs through a high-energy radical intermediate that can be trapped at 1.8 K. The initial radical, formed at 1.8 K, relaxes at 77 K to yield a phenoxyl radical with a longer hydrogen bond to the histidine.

Designing synthetic models able to mimic intricate protein/radical interactions that ultimately allow generation of highly energetic but long-living radicals through proton coupled electron transfer reactions (PCET) is a challenging step in the development of artificial photosynthetic devices[113] and could also lead to a deeper understanding of the more complex natural system.[114] A bio-inspired organic/inorganic hybrid system, **triad-1**, consisting of ca. 3 to 4 dyads of benzimidazole phenol porphyrin moieties ($BiP–PF_{10}$) attached to a nanoparticle of TiO_2 has been constructed. While it is not structurally a triad it functions as such. Excitation of the porphyrin is followed by electron transfer to the nanoparticle and a second electron transfer from BiP to the porphyrin radical cation ensues. The second electron transfer is coupled to an associated proton transfer process to yield a final charge separated state characterized by an electron

in the semiconducting TiO_2 nanoparticle, a benzimidazolium cation and a neutral phenoxyl radical which is thermodynamically competent to oxidize water[115] (Fig. 1).

Using EPR spectroscopy, herein we provide evidence that formation of the phenoxyl radical species in **triad-1** at 13 K results in an energetic intermediate radical state, which at 100 K undergoes a change that can be interpreted in terms of solvation and conformational reorganization to yield a relatively more stable phenoxyl radical. This relaxation mimics that observed for D2-Tyr_D-His189 pair in PSII[37] and suggests a key role of PCET in mediating electron transfer between natural and artificial reaction centers and water oxidizing catalysts.

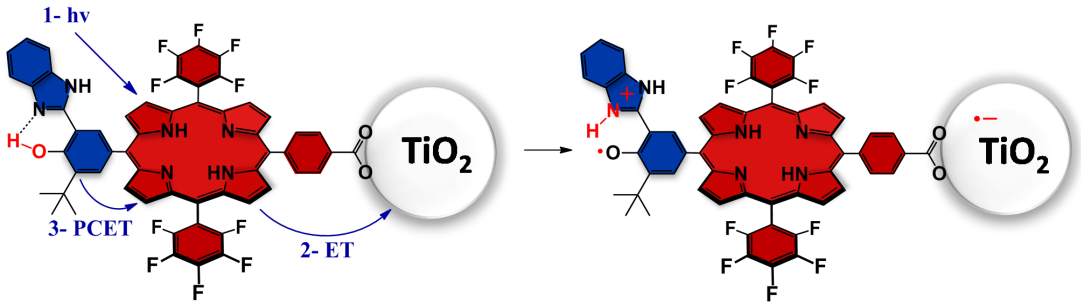

Figure 1. Bioinspired **triad-1** consisting of three covalently-linked redox subunits. Upon irradiation (1- hn), the system is able to undergo a primary electron transfer reaction (2- ET) and a proton-coupled electron transfer (3- PCET) reaction.

Results

Formation of a charge separated state in **triad-1** is unambiguously verified by the X-band (9.5 GHz) EPR spectrum (Supplementary Fig. S1) that shows an axially symmetric signal with $g_{\parallel} = 1.961$ and $g_{\perp} = 1.989$, corresponding to electrons in the TiO_2 interior, and an isotropic signal at $g = 2.0043$, corresponding to holes localized on the organic part of the

construct. Importantly, this spectrum clearly indicates an approximately equal number of injected electrons in the TiO_2 nanoparticles and holes in the organic moiety, confirming that excitation of the porphyrin (PF_{10}) is followed by charge separation via electron transfer from PF_{10} to the semiconductor.[41,116] The EPR signals observed with **dyad-2** (see structure in Fig. 4), which lacks the primary electron acceptor (TiO_2), is approximately 1% of the signal obtained with **triad-1** (Supplementary Fig. S2).

Following the initial charge separation, a secondary electron transfer from the phenol moiety of BiP to $PF_{10}^{\bullet+}$ is expected to form a phenoxyl radical. Evidence for such a process comes from transient absorption studies with a molecular triad system, where in place of the TiO_2 nanoparticle of **triad-1**, a high potential tetracyano porphyrin was used as the primary electron acceptor.[115]

Any change in the local environment of the initially formed phenoxyl radical of **triad-1** upon annealing can be determined from high-resolution, temperature dependent EPR measurements by following the change of the *g*-tensor component oriented along the phenolic C–O bond (g_x). For phenoxyl radicals, spin-orbit coupling interaction between the unpaired electron in the singly occupied molecular orbital (SOMO) and the nonbonding electron pairs of the oxygen atom induces a magnetic moment, which results in a deviation of the g_x component of the *g*-tensor from the free electron *g*-value (g_e = 2.0023). Hydrogen bonding with the lone pair of the oxygen atom in the oxygen centered radicals and/or delocalization of the unpaired spin density are known to decrease this deviation, yielding radicals with lower g_x values.[117,118]

When a suspension of **triad-1** in acetonitrile at 13 K is irradiated with a 532 nm laser, the D-Band (130 GHz) EPR spectrum (Fig. 2, red trace) is dominated by the

resolved *g* anisotropic coupling tensors (g_x = 2.0056; g_y = 2.0042; g_z = 2.00215). Annealing the sample at 100 K in the dark for 10 min and returning to 13 K (see Methods) results in a significant increase in the g_x value from 2.0056 to 2.0061, while the other two *g*-tensor components remain unchanged (Fig. 2, blue trace). These observations clearly indicate the thermally activated conversion of the initially formed phenoxyl radical species to another in which structural and solvent reorganization have taken place.[119-125] This temperature dependence of the g_x values was not observed in a construct related to triad-**1** in which the benzimidazole was the linker between PF_{10} and the phenol group,[41] and has not been reported in any other BiP system or artificial system that mimics PSII.

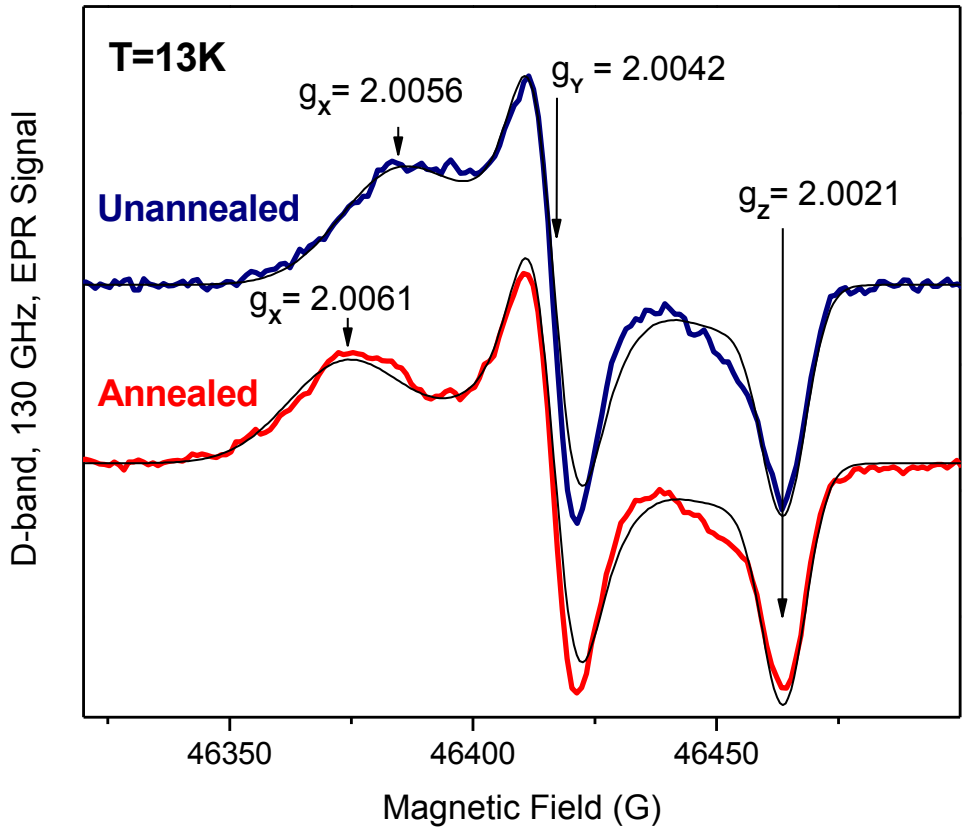

Figure 2. Photoinduced D-band (130 GHz) EPR spectra of an acetonitrile suspension of **triad-1** recorded at 13 K. Red: immediately after sample illumination in the cavity of the spectrometer. Blue: after illuminated sample has been annealed at 100 K in the dark for 10 minutes and cooled back to 13 K.

Extensive theoretical and experimental EPR investigations of proteins and model compounds have established that the g_x values for non-interacting tyrosyl and phenoxyl radicals in nonpolar environments are larger than 2.0080, whereas those radicals engaged

in hydrogen bonds range from 2.0064 to 2.0075.[119,124] A protonated phenoxyl radical can be understood as an extreme case where one of the oxygen lone pairs is engaged in a covalent bond with the proton; therefore a very low g_x value is expected for such radical. From Density Functional Theory (DFT) calculations, the g_x value for a protonated phenoxyl radical in a benzimidazole-phenol model compound has been estimated to be as low as 2.004.[119,121]

The g_x values determined at low temperature (2.0056) and after annealing and returning to 13 K (2.0061) for the phenoxyl radicals in **triad-1** are lower than those reported in the literature for such radicals interacting exclusively through hydrogen bonds,[41,119-124] suggesting spin delocalization between the phenoxyl radical and the high-potential porphyrin (*vide infra*), but are significantly higher than the g_x value calculated for a protonated phenoxyl radical (2.004).[121] The fact that the g_x values are higher than that of the protonated phenoxyl radical strongly indicates that both phenoxyl radicals detected in the present study are formally neutral radicals. This supports the hypothesis that the oxidation of the phenol in **triad-1** occurs with transfer of the phenolic proton to the benzimidazole group even at 13 K.

Spin delocalization over the porphyrin core in the radical of **triad-1** is supported by DFT calculations on the organic component of **triad-1** (Supplementary Fig. S4), which reveal non-negligible spin density over the porphyrin moiety. Data from electrochemical experiments in acetonitrile on the methyl ester derivative of the organic component of **triad-1** (**dyad-2**, chemical structure in Fig. 4) corroborate delocalization of the spin and cationic charge of the phenolic radical onto the porphyrin. The first porphyrin oxidation in **dyad-2** occurs at a much higher potential (about 1.65 V, *vs.* SCE)

than that of a porphyrin model compound lacking the benzimidazole-phenol group (1.29 V *vs.* SCE), whereas the phenol oxidation potential is roughly the same (1.00 V *vs.* SCE) in **dyad-2** and in a benzimidazole-phenol model compound lacking the porphyrin group (1.04 V *vs.* SCE) (Supplementary Table S3). Because in **dyad-2** the phenol electrochemical oxidation **occurs** at about 1 V and formation of the porphyrin radical cation is the second electrochemical oxidation, the increase of the porphyrin oxidation potential from 1.29 V to 1.65 V is clear evidence that the hole of the benzimidazole-phenol residue is partially delocalized over the porphyrin core making it harder to oxidize.

Formation of a neutral phenoxyl radical in **triad-1** at 13 K, where nuclear motions are restricted, implies that very little energy, probably only zero-point motion, is required for the proton to move to a new potential minimum during the oxidation of the phenol residue. This finding indicates that the phenol-benzimidazole group is well-oriented to form a strong intramolecular hydrogen bond, which creates a coordinate for proton motion that facilitates its transfer even at very low temperatures.[111,119,120,126-129] Structural investigation of **dyad-2** confirms the formation of a strong intramolecular hydrogen bond. The crystal structure of **dyad-2** (Fig. 3, CCDC deposition number: 949079) reveals that the phenol and benzimidazole moieties are nearly coplanar with a dihedral angle of 14.6^{o}, which is significantly smaller than those between 29^{o}–33^{o} observed for similar systems in the absence of intramolecular hydrogen bonds.[119] This relatively small dihedral angle between the two H-bonded partners in **dyad-2** results in a short O$\cdots$N distance of 2.58 Å, indicating the presence of a strong electrostatic interaction between the phenolic proton and the lone pair of the nitrogen atom on the BiP.[130]

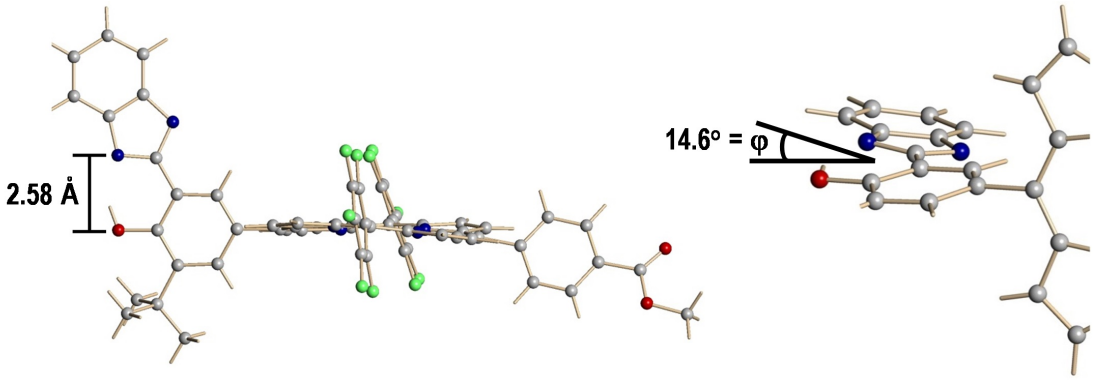

Figure 3. Crystal structure of **dyad-2**. Gray, carbon; red, oxygen; blue, nitrogen; green, fluorine. On the right, a partial structure of **dyad-2** is shown where the *t*-butyl group *ortho* to the phenol and part of the porphyrin have been deleted in order to visualize better the dihedral angle between the phenol and the imidazole groups.

The strong hydrogen bond in **dyad-2** is also observed in solution. The ^{1}H NMR spectrum of **dyad-2** in chloroform (Fig. 4) shows the presence of a sharp signal at 14.23 ppm, which is unambiguously attributed to the phenolic proton.[40] Such a downfield shift from the usual 5–6 ppm region indicates that the phenolic proton is relatively far from the shielding effects of the electrons on the oxygen atom and the sharpness of the peak is strong evidence that the phenolic proton is not exchanging on the NMR time scale, which is ensured by the strong intramolecular H-bond.[124,130] The ^{1}H NMR spectra in more polar media (deuterated acetonitrile, -O<u>H</u> resonance at 14.47 ppm and deuterated acetone, -O<u>H</u> resonance at 14.58 ppm) lead to similar conclusions.

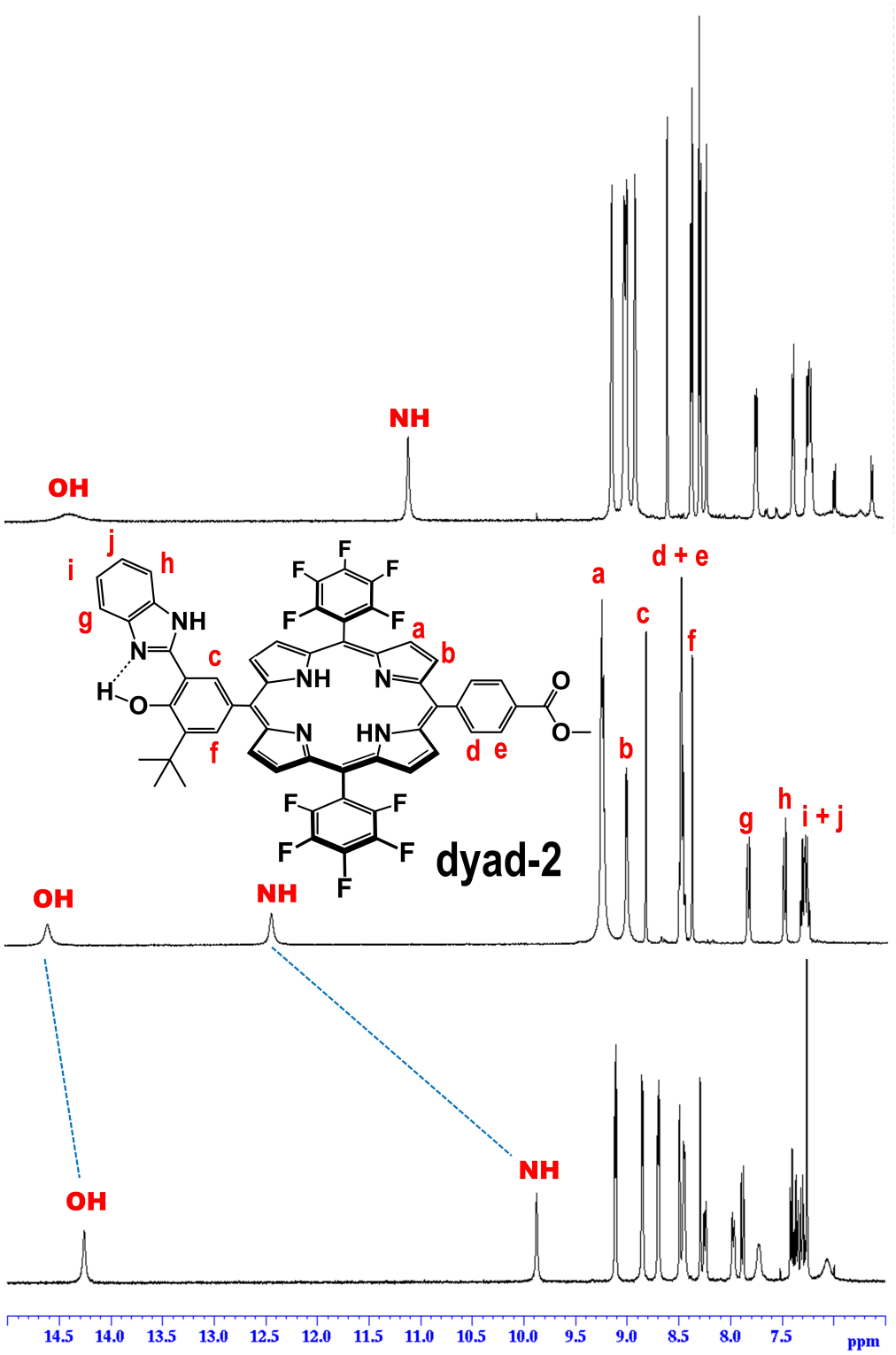

Figure 4. Partial ^{1}H NMR spectra (500 MHz, 298 K) of **dyad-2** in three different deuterated solvents: acetonitrile (top), acetone (middle) and chloroform (bottom).

Furthermore, when comparing the ^{1}H NMR spectrum of **dyad-2** in deuterated acetonitrile with that of a simple benzimidazole phenol model,[41] the –OH resonance in **dyad-2** is found 0.8 ppm farther downfield. This is evidence for a stronger hydrogen bond in **dyad-2**. We propose that the strong electron withdrawing effect of the fluorinated porphyrin bonded to the phenol residue renders the phenolic group significantly more acidic, reducing its p*Ka* to a value closer to that of the benzimidazolium ion. This inductive effect promotes a better match of the proton affinities of the two H-bond partners in **dyad-2**, hence accounting for the observed strong hydrogen bond.[126] Turning to the distal proton of the benzimidazole group, its NMR resonance in **dyad-2** is shifted downfield from 9.88 ppm in the nonpolar chloroform to 11.09 ppm in acetonitrile to 12.43 ppm in acetone (Fig. 4) indicating increasing hydrogen bond formation with the solvent.

Discussion

As mentioned above, the high g_x values for the phenoxyl radicals of **triad-1** (2.0056 and 2.0061) compared to that of a protonated phenoxyl radical (2.004) provide clear evidence that the electron transfer from the phenol to the radical cation of the porphyrin in **triad-1** occurs with transfer of the phenolic proton to the benzimidazole group. The presence of a strong hydrogen bond between the phenol and the benzimidazole moiety leads to the possibility that the electron and proton transfer reactions occur through a single step in a concerted mechanism. The concerted mechanism is supported by thermodynamic considerations. Electrochemical investigation in acetonitrile (Supplementary Table S3) reveals that a porphyrin model compound lacking the benzimidazole-phenol group shows a standard potential of 1.29 V (*vs.* SCE),

while a non-hydrogen bonded phenol model has oxidation potential of 1.36 V (*vs.* SCE, irreversible). Therefore, the photo-generated fluorinated porphyrin radical cation ($PF_{10}^{\bullet+}$) should not be thermodynamically competent to oxidize the phenol residue in **triad-1** without transfer of the proton to the benzimidazole moiety, rendering the stepwise electron transfer followed by proton transfer (ET-PT) mechanism unlikely although it cannot be absolutely excluded with the present information.[115] A proton transfer followed by electron transfer (PT-ET) stepwise mechanism is also unlikely in the case of **triad-1**, as the benzimidazolium cation (p*Ka* ~17) is a stronger acid than the phenol group (p*Ka* ~ 27) in acetonitrile,[126,131] even after taking into consideration the inductive effect of the electron deficient PF_{10} on the phenol.[131,132]

The observation that both electron and proton transfer processes occur at 13 K strongly suggests that either the proton tunnels from a site near the phenolic oxygen to one near the imidazole nitrogen or its zero-point energy is higher than the proton transfer barrier.[124,129] Although tunneling usually has a distinct kinetic isotope effect (KIE) signature, a negligible (or slightly inverted) KIE was observed in electrochemical experiments of **dyad-2** (0.96 ± 0.2) (Supplementary Fig. S8). Theory predicts that under certain circumstances a vanishingly small KIE would be observed for PCET reactions involving proton tunneling.[133] Additional electrochemical measurements with model systems and theoretical calculation are being conducted to clarify this issue.

Focusing on the temperature-induced relaxation process observed in the EPR experiments, DFT calculations were performed in an effort to elucidate the cause/s responsible for the thermal relaxation of the phenoxyl radicals initially generated upon illumination of **triad-1** at 13 K. Following literature methodology,[121] the *g*-values for

different structures of the radical cation of the organic component of **triad-1** were calculated (Supplementary Fig. S5, Table S1).

The calculated g_x-value for structure $\mathbf{A}^{\bullet+}$ (Fig. 5) is consistent with the experimental g_x-value at 13 K. The main features of structure $\mathbf{A}^{\bullet+}$ are that the phenolic proton resides on the benzimidazole group, the benzimidazole distal proton is hydrogen bonded with a water molecule and a second water molecule is hydrogen bonded to the phenoxyl oxygen. These features are consistent with the tentative conclusion that the PCET process at the BiP moiety occurs in a concerted single step and the observation that the distal proton is hydrogen bonded with solvent molecules. At 13 K, neither solvent molecule has enough energy to reorganize, resulting in a high-energy state with a g_x of 2.0056.

Upon warming the solution to 100 K, the energy available for solvent reorganization increases and hydrogen bond formation involving the solvent and the newly formed N–H site is possible, resulting in structure $\mathbf{B}^{\bullet+}$. Compared to $\mathbf{A}^{\bullet+}$, $\mathbf{B}^{\bullet+}$ (which has a new bifurcated hydrogen bond with a water molecule) shows an increase in both the BiP dihedral angle and in the O–H and O−N distances, which would result in an increase of the g_x-value. Indeed, the calculated g_x-value for $\mathbf{B}^{\bullet+}$ is in agreement with the g_x-value observed after annealing at 100 K, indicating that $\mathbf{B}^{\bullet+}$ or similar structures are plausible (Supplementary Table S1). Calculations performed using acetonitrile as the hydrogen bonding solvent yielded similar results (Supplementary Fig. S5 and Table S1).

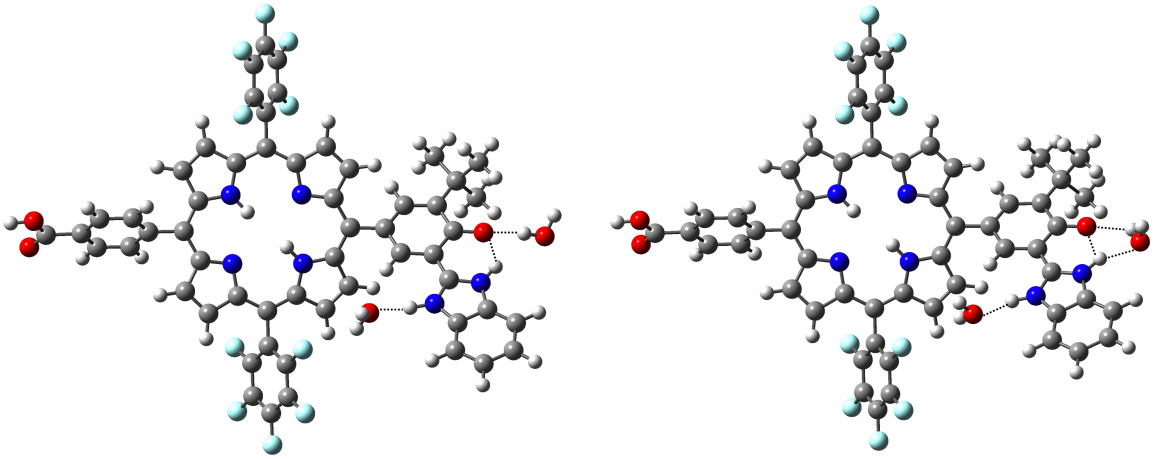

Figure 5. Calculated structures of the radical cation of the organic component of triad-**1** before thermal relaxation (**Structure A**$^{\bullet+}$) and after thermal relaxation (**Structure B**$^{\bullet+}$). **A**$^{\bullet+}$ includes water molecules hydrogen bonded to the distal N–H and the phenoxyl oxygen and **B**$^{\bullet+}$ includes water molecules hydrogen bonded at both distal and proximal N–H sites (see text). Carbon (gray), hydrogen (white), nitrogen (blue), fluorine (cyan) and oxygen (red).

The inclusion of explicit solvent molecules in a continuum model for the calculated *g*-values results in a better match to the values observed experimentally in the case of *o*-semiquinones in protic solvents.[134,135] In our model, the water molecule around the proximal N–H bond of **B**$^{\bullet+}$ is acting as a hydrogen bond acceptor with the newly formed N–H and as a hydrogen bond donor to the phenoxyl oxygen. Interestingly, this

water molecule is similarly positioned to the water molecule hydrogen bonded to $Tyr_D^{\bullet}$ proposed for the multiple proton pathway mechanism of Barry *et al.,* for the reduction of $Tyr_D^{\bullet}$ to Tyr_D.[125,136,137] We also note that several ordered water molecules are present around Tyr_Z His 190 in the water oxidizing branch of PSII.[38]

In summary, a hybrid construct comprising ca. 3 to 4 molecular dyads attached to a semiconductor nanoparticle has been found to model functional and structural aspects of a PCET process thought to be central to water oxidation in PSII. In this construct, just as in PSII,[37,138] high field EPR clearly detects the formation of phenoxyl radicals in two different states, a higher energy state formed at 13 K and a relaxed state observed when the sample is warmed to 100 K. DFT calculations indicate that solvent molecules solvating the initial O–H$^{\cdots}$N site must reorganize to solvate the newly formed O$^{\cdots}$H–N site. This reorganization is blocked at 13 K resulting in a higher-energy state with a g_x value of 2.0056. After warming to 100 K, the solvent molecules around the new O$^{\cdots}$H–N site reorganize to form a bifurcated hydrogen bond. Such solvent reorganization and structural rearrangements around the BiP result in the relaxed final structure with a g_x value of 2.0061. Thermodynamic considerations suggest that the PCET in the case of **triad-1** likely occurs by a concerted mechanism.

The thermal relaxation observed by high field EPR in these systems is not ubiquitous. A construct similar to **triad-1**, but having a weaker intramolecular hydrogen bond and the benzimidazole group as part of the linkage between the porphyrin and phenol moieties, did not demonstrate such relaxation.[41] Thus, it is significant that **triad-1** mimics the thermal relaxation observed in the natural system. The simplicity of the structure allows us to identify the unusually strong intramolecular hydrogen bond

between the phenol and the benzimidazole moiety, as the structural parameter that is responsible for the biomimetic behavior.

It has been postulated that the PCET within the D1-Tyr_z-His190 group, which acts as a redox mediator/relay in PSII, plays a role in the high quantum efficiency of water oxidation by $P680^+$ by providing a kinetic coupling between the fast initial electron transfer events and the slower process of water oxidation. In this connection, incorporation of a BiP redox mediator/relay in an artificial system did significantly improve the quantum yield for transfer of electrons from a water oxidizing catalyst to an oxidized dye in a nanoparticulate TiO_2 based photoanode in which the dye radical cation plays a role analogous to that of $P680^+$.[16]

Methods

Synthesis. Porphyrin model (S6, Supplementary Table S3),[40] benzimidazole-phenol model[41] and **dyad-2**[40,115] were prepared following procedures previously reported.

TiO_2 colloidal preparation. Transparent TiO_2 nanoparticle colloidal aqueous solutions were prepared by the dropwise addition of titanium(IV) chloride to cooled water. The temperature and rate of component mixing of reactants were controlled by an apparatus developed for automatic colloid preparation.[139] The pH of the solution was between 0 and 1, depending on the $TiCl_4$ concentration. Slow growth of the particles was achieved by using dialysis at 4°C against water until the pH of the solution reached 3.5, indicating particle growth was complete. The final concentration was 0.17 M TiO_2 with particle size of 4.5 ±1 nm. The solution was mixed with 0.6 mM of the carboxylic acid form of **dyad-2**, which was dissolved in THF and the resulting solution dried under

nitrogen atmosphere. The dried particles were redispersed in acetonitrile solution. Each solution contains on average 3.5 molecules of the carboxylic acid form of **dyad-2** per TiO_2 nanoparticle.

Electron Paramagnetic Resonance (EPR). High-frequency EPR spectra were recorded at D-band (130 GHz/4.6 T) with a continuous wave/pulsed EPR spectrometer described previously.[140] A cylindrical single-mode cavity TE011 was used, having slits on the cylindrical side of the cavity to allow for optical excitation and field modulation. Samples were illuminated in the cavity of the EPR spectrometer. Light excitation was achieved with an optical parametric oscillator (Opotek) pumped by a Nd:YAG laser (Quantel). The output of the laser was coupled to a fiber optic in order to deliver light to the cavity (1 mJ per pulse). The excitation wavelength was 520 nm. The sample temperature was regulated by an Oxford temperature controller (ITC 503) coupled to an Oxford continuous-flow cryostat (CF 1200). The simulation program SIMFONIA from Bruker Instruments Inc. was used for simulations of the spectra.

The annealing was tried at different temperatures. At $T < 70K$ the signal transformation was negligible at reasonable annealing times (~20 min). At $T > 120$ K a substantial decay of the EPR signal (which was recorded after freezing back to 13 K) was observed. Annealing at 100 K for 10 minutes lead to the spectra transformation without large change in the EPR intensity.

X-ray structures. CCDC deposition number for **dyad-2** is 949079.

Acknowledgements

This work was supported as part of the Center for Bio-Inspired Solar Fuel Production, an Energy Frontier Research Center funded by the US Department of Energy, Office of Science, Office of Basic Energy Sciences under Award DE-SC0001016. D.D.M.H. was supported by the National Science Foundation Graduate Research Fellowship Program (NSF-GRFP) under Grant No. DGE-0802261 and by the More Graduate Education at Mountain States Alliance (MGE@MSA) Alliance for Graduate Education and the Professoriate (AGEP) National Science Foundation (NSF) Cooperative Agreement No. HRD-0450137. The high-frequency EPR work was supported by the U.S. Department of Energy, Office of Basic Energy Sciences, Division of Chemical Sciences, Geosciences, and Biosciences, under Contract DE-AC02-06CH11357 (O.G.P.). The work performed at the Center for Nanoscale Materials was supported by the U. S. Department of Energy, Office of Science, Office of Basic Energy Sciences, under Contract No. DE-AC02-06CH11357.

Author contributions

J.D.M.J., D.G., T.A.M. and A.L.M. designed research and experiments. J.D.M.J. and M.E.T.J. synthesized and characterized all chemical compounds. J.D.M.J and T.L.G are responsible for the crystal structure. D.D.M.H. and V.M. conducted theoretical calculations. O.G.P. and T.R. performed EPR experiments. A.L.T. executed electrochemical measurements. M.J.L.P. and G.K. performed photophysical characterizations. J.D.M.J., D.D.M.H., M.J.L.P., G.K., O.G.P., T.R., V.M., D.G., T.A.M.,

A.L.M. analyzed and interpreted the data. J.D.M.J., D.D.M.H., D.G., T.A.M. and A.L.M. wrote the manuscript.

The authors declare no competing financial interest.

Additional information

Supplementary information is available in the online version of the paper. Reprints and permissions information is available online at www.nature.com/reprints. Correspondence and requests for materials should be addressed to A.L.M.

5.2 Supplementary Theoretical Calculations

The theoretical structures were optimized with Gaussian 09[58] at the B3LYP/6-31G(d,p)[59-64] level of theory using the Conductor-like Polarizable Continuum Model (CPCM)[98,99] for the acetonitrile environment. The g-values for all the structures were obtained with ORCA[141] at the B3LYP/EPR-II[142] level of theory using the Conductor-Like Screening Model (COSMO)[143] to simulate the acetonitrile environment.

The spin-density population of the structure that corresponds to the carboxylic acid form of **dyad-2** depicted as a radical cation after the proton transfer from the phenol to the benzimidazole is shown in Supplementary Fig. S4. In agreement with the experimental data, a very strong intra-molecular hydrogen bond can be inferred from the small dihedral angle (less than 2°) between the phenol and imidazole planes of the BiP moiety in the optimized structure. The spin-density distribution reveals that the unpaired electron is delocalized to some extent between both the porphyrin and the phenol rings. The ratio of the unpaired spin populations (PF_{10}:BiP) is approximately 35:65. This explains the observation that the g_x-value of **dyad-2** is lower than those reported for other BiP systems.[119,121]

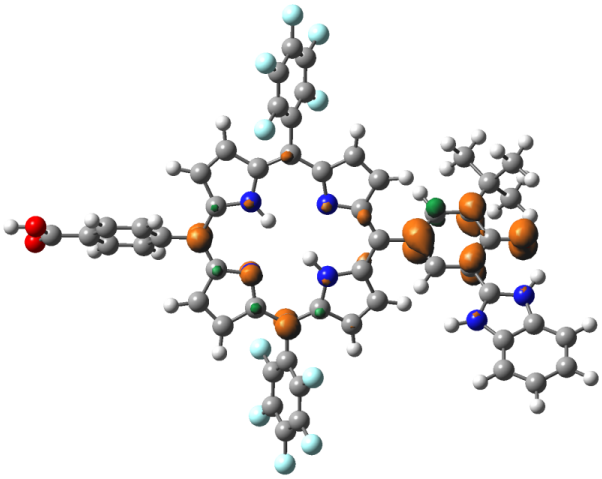

Supplementary Figure S4. Spin density (the orange and green colors show positive and negative spin densities, respectively) for a structure of the carboxylic acid form of **dyad-2** as a radical cation after PCET geometry optimized using Gaussian 09 at the B3LYP/6-31G(d,p) level of theory and the Conductor-like Polarizable Continuum Model (CPCM) to include the acetonitrile environment in the calculations. Carbon (grey), hydrogen (white), nitrogen (blue), fluorine (cyan) and oxygen (red).

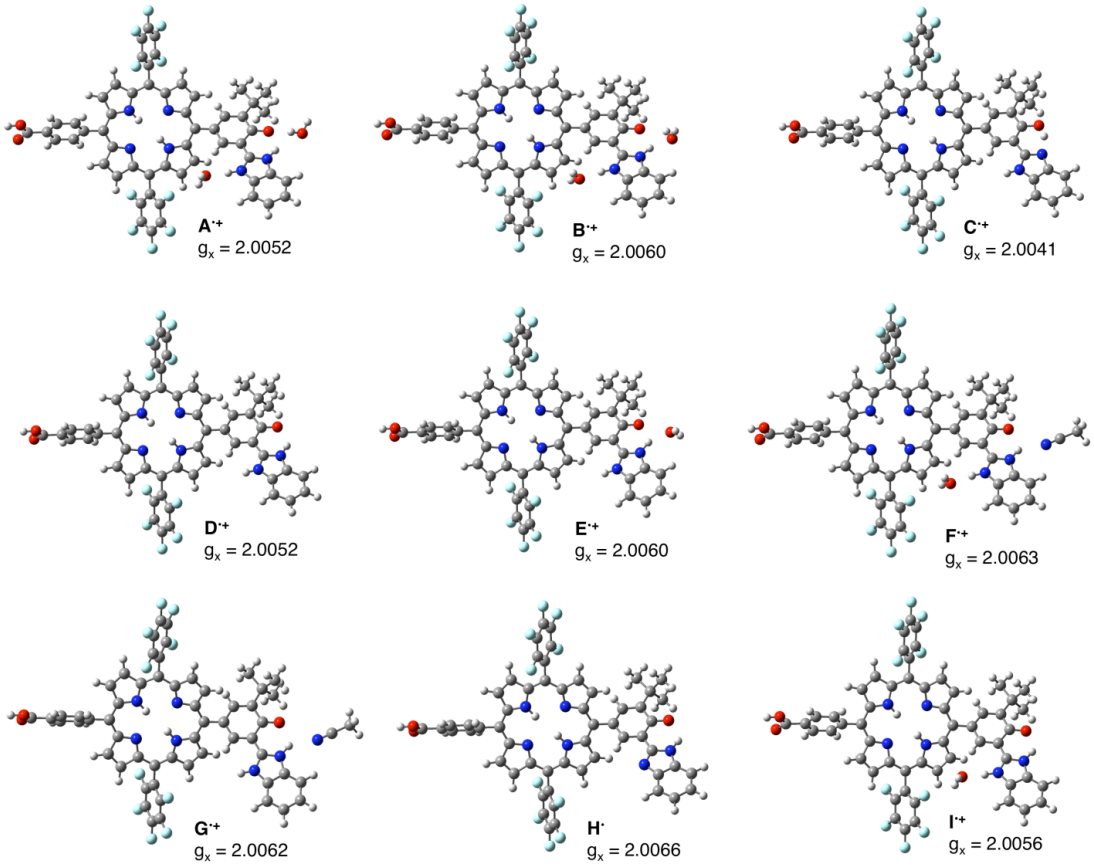

Supplementary Figure S5. Structures of the carboxylic acid form of **dyad-2**, as a radical cation after PCET, geometry optimized with Gaussian 09 at the B3LYP/6-31G(d,p) level of theory and the Conductor-like Polarizable Continuum Model (CPCM) to include the acetonitrile environment in the calculations. Explicit water and/or acetonitrile molecules are included where indicated in calculated structures.

Calculations of the anisotropic g-values for the series of radical cation structures presented in Supplementary Fig. S5 and Supplementary Table S1 were performed following methodology from the literature.[121] Structures with solvent molecules involved in hydrogen bonds with N–H sites were based on the fact that the distal N–H proton interacts strongly with solvent molecules as revealed by ^{1}H-NMR studies. Solvent molecules binding to the newly formed N–H bond were chosen based on the expectation

of that this new N–H site would behave similarly to the distal N–H (See Fig. 4 and Fig. 5 in the manuscript and discussion therein).

Supplementary Table S1. Comparison between experimental *g* values for the carboxylic acid form of **dyad-2**, as a radical cation, initially formed at 13 K and after annealing at 100 K and returned to 13 K for the measurement in two states and the calculated *g* values for structures $\mathbf{A}^{\bullet+}$–$\mathbf{I}^{\bullet+}$ obtained with ORCA at the B3LYP/EPRII level of theory and using COSMO to simulate the acetonitrile environment.

	g_x	g_y	g_z
Exp. at 13 K	2.0056	2.0042	2.0022
Exp. after annealing at 100 K	2.0061	2.0042	2.0022
Theoretical Structure $\mathbf{A}^{\bullet+}$	2.0052	2.0041	2.0024
Theoretical Structure $\mathbf{B}^{\bullet+}$	2.0060	2.0044	2.0023
Theoretical Structure $\mathbf{C}^{\bullet+}$	2.0041	2.0032	2.0025
Theoretical Structure $\mathbf{D}^{\bullet+}$	2.0052	2.0040	2.0024
Theoretical Structure $\mathbf{E}^{\bullet+}$	2.0060	2.0045	2.0023
Theoretical Structure $\mathbf{F}^{\bullet+}$	2.0063	2.0044	2.0023
Theoretical Structure $\mathbf{G}^{\bullet+}$	2.0062	2.0044	2.0023
Theoretical Structure $\mathbf{H}^{\bullet}$	2.0066	2.0047	2.0024
Theoretical Structure $\mathbf{I}^{\bullet+}$	2.0056	2.0042	2.0024

It is important to clarify that in our model we take into account explicitly two solvent molecules and the solvent reorganization is defined in the following way. For example, in the case of $\mathbf{A}^{\bullet+}$ reorganizing to form $\mathbf{B}^{\bullet+}$, we start with a structure in which the two explicit water molecules are near the positions shown in $\mathbf{A}^{\bullet+}$ and then run the geometry optimization program to yield the actual structure shown as $\mathbf{A}^{\bullet+}$. We then relocate the water molecule near the newly formed N–H site and run the geometry optimization program again to yield structure $\mathbf{B}^{\bullet+}$. The change in solvent structure between the two geometry-optimized systems is the reorganization of the explicit water (solvent). The remaining solvent effect is included using the conventional dielectric model. Other reorganizations in the system include a change in the BiP dihedral angle and concomitant changes in the distance between phenoxyl O and N–H site.

The calculated *g*-values for the radical cation of the carboxylic acid form of **dyad-2** without taking into account hydrogen bond formation involving the new (proximal) N–H site and an explicit solvent molecule yields results that are very close to the experimental g-values observed at 13 K (Supplementary Table S1 and Supplementary Fig. S5, $\mathbf{A}^{\bullet+}$, $\mathbf{D}^{\bullet+}$ and $\mathbf{I}^{\bullet+}$). This agreement supports the interpretation that at 13 K the solvent molecules do not have enough energy to reorganize to form a hydrogen bond with the newly formed (proximal) N–H site. Upon warming of the solution to 100 K the energy available for solvent reorganization increases and hydrogen bond formation involving the newly formed (proximal) N–H site is possible resulting in an increase of the g_x-value. The calculated g-values for radical cations including this new hydrogen bond with solvent molecules are in excellent agreement with those observed at 100 K (Supplementary Table S1 and Supplementary Fig. S5, $\mathbf{B}^{\bullet+}$, $\mathbf{E}^{\bullet+}$, $\mathbf{F}^{\bullet+}$ and $\mathbf{G}^{\bullet+}$). The

calculated g_x-value for a structure before proton transfer ($\mathbf{C}^{\bullet+}$) results in a value much lower than that observed experimentally even at 13 K. For the case where the distal N–H proton is deprotonated by a base yielding a neutral radical ($\mathbf{H}^{\bullet}$) the calculated g_x-value is much higher than that observed experimentally even after annealing at 100 K.

Supplementary Table S2. Comparison between calculated structural parameters for structures $\mathbf{A}^{\bullet+}$–$\mathbf{I}^{\bullet+}$. The structures are geometry optimized with Gaussian 09 at the B3LYP/6-31G(d,p) level of theory and the Conductor-like Polarizable Continuum Model (CPCM) to include the acetonitrile environment in the calculations. (For structures see Supplementary Fig. S5).

Structure	Charge, multiplicity	Number of explicit water molecules	Number of explicit acetonitrile molecules	BiP O–H distance (Å)	BiP N–H distance (Å)	BiP N–O distance (Å)	BiP dihedral angle (°)	ΔE relative to structure $\mathbf{C}^{\bullet+}$ (kcal/mol)[a]
$\mathbf{A}^{\bullet+}$	1,2	2	0	1.88	1.02	2.62	1.82	-19.05
$\mathbf{B}^{\bullet+}$	1,2	2	0	2.14	1.03	2.72	7.12	-21.93
$\mathbf{C}^{\bullet+}$	1,2	0	0	1.02	1.58	2.53	-0.05	Reference
$\mathbf{D}^{\bullet+}$	1,2	0	0	1.84	1.02	2.60	-1.69	-2.76
$\mathbf{E}^{\bullet+}$	1,2	1	0	2.34	1.04	2.80	24.4	-10.15
$\mathbf{F}^{\bullet+}$	1,2	1	1	2.01	1.02	2.67	3.87	-17.85
$\mathbf{G}^{\bullet+}$	1,2	0	1	1.99	1.02	2.66	2.80	-5.79
$\mathbf{H}^{\bullet}$	0,2	0	0	1.94	1.02	2.65	-0.04	-
$\mathbf{I}^{\bullet+}$	1,2	1	0	1.86	1.02	2.62	1.55	-14.45

a) ΔE relative to structure $\mathbf{C}^{\bullet+}$ (kcal/mol) was calculated by the following equation:

$\Delta E = E(\text{Structure}) - E(\mathbf{C}^{\bullet+}) - (E(\text{explicit solvent}) \times \text{number explicit solvent molecules})$.

The structure with the highest energy is **C**$^{\bullet+}$**,** corresponding to BiP–$PF_{10}$$^{\bullet+}$ before the proton is transferred from the phenol to the benzimidazole. The energy of this structure (**C**$^{\bullet+}$) was used as the reference to calculate ΔE. Upon proton transfer to the benzimidazole (**D**$^{\bullet+}$), the energy decreases. Adding a hydrogen bond acceptor to the distal N–H of the BiP further lowers the energy (**I**$^{\bullet+}$). Addition of a water molecule hydrogen bonded to the nearby the N–H$^{\cdots}$O bond of the BiP stabilizes the system further (**A**$^{\bullet+}$ and **B**$^{\bullet+}$), but the g_x-value increases only when a bifurcated hydrogen bond involving the newly formed N–H site is formed (**B**$^{\bullet+}$). Structure **E**$^{\bullet+}$ shows the effect of water hydrogen bonded to the newly formed N–H site without the distal water, and structures **F**$^{\bullet+}$ and **G**$^{\bullet+}$ show the effect of acetonitrile hydrogen bonded to the newly formed N–H site with and without the distal water. Notice that acetonitrile is not hydrogen bonded to the distal N–H in any of the structures. Due to steric considerations when an acetonitrile molecule is included at this site the structures cannot be geometry optimized without a serious distortion of the porphyrin macrocycle.

CHAPTER 6

CONCLUSIONS

Recent progress towards the design of WSDSPECTCs was presented in this dissertation. The synthesis and characterization of functional dye sensitizers for both junctions of the tandem cells was reported. One of the advantages of these dyes is that they can be synthetized in only three steps. Photocurrents measured for WSDSPETCs demonstrate that these cells can work without and external bias. Some of these cells incorporated a benzimidazole phenol (BiP) moiety that mimics the tyrosine histidine pairs of Photosystem II. Photocurrents of present WSDSPECTCs were found to be limited by the performance of the WSDSPAs. Design of more efficient dyes and catalyst for WSDSPAs is being pursued.

With the desire of using computational chemistry as a tool in design of new dyes for WSDSPECTCs, correlations between HOMO-LUMO energies and redox potentials were built and tested[33]. It was found that the inclusion of a continuum solvent model in the calculations was required for accurate results and that density functional theory (DFT) methods perform better than semi-empirical methods. This methodology is useful for the design of new molecules capable of participating in electron transfer reactions.

The inclusion of explicit water molecules in DFT calculations was found to be mandatory to elucidate the thermal relaxation mechanism of an artificial triad capable of mimicking the proton coupled electron transfer (PCET) observed in the tyrosine-histidine pairs of photosystem II[36]. DFT calculations that take in consideration the reorganization of solvent molecules nearby the proton donor and acceptor sites to hydrogen bond the

new N-H site that forms after PCET were found to yield g-values that are in good agreement with the experimental results. These results highlight the importance of water clusters around the tyrosine-histidine pairs of Photosystem II and suggest a new mechanism for the thermal relaxation observed by Faller *et. al*[37] in the catalyst-depleted natural system.

REFERENCES

(1) Turner, J. A. Science 2004, 305, 972–974.

(2) Berardi, S.; Drouet, S.; Francàs, L.; Gimbert-Suriñach, C.; Guttentag, M.; Richmond, C.; Stoll, T.; Llobet, A. Chem Soc Rev 2014.

(3) BOCKRIS, J.; DANDAPANI, B.; COCKE, D.; GHOROGHCHIAN, J. International Journal of Hydrogen Energy 1985, 10, 179–201.

(4) Moore, T. A.; Moore, A. L.; Gust, D. AIP, 2013; Vol. 1519, pp. 68–72.

(5) Graetzel, M. Acc. Chem. Res. 1981, 14, 376–384.

(6) Calvin, M. Photochemistry and Photobiology 1983, 37, 349–360.

(7) Sherman, B. D.; Vaughn, M. D.; Bergkamp, J. J.; Gust, D.; Moore, A. L.; Moore, T. A. Photosyn. Res. 2013.

(8) Blankenship, R. E. R.; Tiede, D. M. D.; Barber, J. J.; Brudvig, G. W. G.; Fleming, G. G.; Ghirardi, M. M.; Gunner, M. R. M.; Junge, W. W.; Kramer, D. M. D.; Melis, A. A.; Moore, T. A. T.; Moser, C. C. C.; Nocera, D. G. D.; Nozik, A. J. A.; Ort, D. R. D.; Parson, W. W. W.; Prince, R. C. R.; Sayre, R. T. R. Science 2011, 332, 805–809.

(9) Nocera, D. G. D. Acc. Chem. Res. 2012, 45, 767–776.

(10) Bard, A. J.; Fox, M. A. Acc. Chem. Res. 1995, 28, 141–145.

(11) Rocheleau, R. E.; Miller, E. L.; Misra, A. Energy Fuels 1998, 12, 3–10.

(12) Mor, G. K.; Varghese, O. K.; Wilke, R. H. T.; Sharma, S.; Shankar, K.; Latempa, T. J.; Choi, K.-S.; Grimes, C. A. Nano Lett. 2008, 8, 1906–1911.

(13) Khaselev, O.; Turner, J. Science 1998, 280, 425–427.

(14) Khaselev, O.; Bansal, A.; Turner, J. A. International Journal of Hydrogen … 2001.

(15) Youngblood, W. J.; Lee, S.-H. A.; Kobayashi, Y.; Hernandez-Pagan, E. A.; Hoertz, P. G.; Moore, T. A.; Moore, A. L.; Gust, D.; Mallouk, T. E. J. Am. Chem. Soc. 2009, 131, 926–927.

(16) Zhao, Y.; Swierk, J. R.; Megiatto, J. D.; Sherman, B.; Youngblood, W. J.; Qin, D.; Lentz, D. M.; Moore, A. L.; Moore, T. A.; Gust, D.; Mallouk, T. E. Proc. Natl. Acad. Sci. U.S.A. 2012, 109, 15612–15616.

(17) Alibabaei, L.; Brennaman, M. K.; Norris, M. R.; Kalanyan, B.; Song, W.; Losego, M. D.; Concepcion, J. J.; Binstead, R. A.; Parsons, G. N.; Meyer, T. J. Proc. Natl. Acad. Sci. U.S.A. 2013, 110, 20008–20013.

(18) Gao, Y.; Zhang, L.; Ding, X.; Sun, L. Phys. Chem. Chem. Phys. 2014.

(19) Gao, Y.; Ding, X.; Liu, J.; Wang, L.; Lu, Z.; Li, L.; Sun, L. J. Am. Chem. Soc. 2013, 135, 4219–4222.

(20) Zhao, J.; Yang, X.; Hao, Y.; Cheng, M.; Tian, J.; Sun, L. ACS Appl Mater Interfaces 2014, 6, 3907–3914.

(21) Fujishima, A.; Honda, K. Nature 1972.

(22) Brillet, J.; Yum, J.-H.; Cornuz, M.; Hisatomi, T.; Solarska, R.; Augustynski, J.; Graetzel, M.; Sivula, K. Nature Photon 2012, 6, 824–828.

(23) McKone, J. R.; Lewis, N. S.; Gray, H. B. Chem. Mater. 2014, 26, 407–414.

(24) Swierk, J. R.; Mallouk, T. E. Chem Soc Rev 2013, 42, 2357–2387.

(25) Faunce, T.; Styring, S.; Wasielewski, M. R.; Brudvig, G. W.; Rutherford, A. W.; Messinger, J.; Lee, A. F.; Hill, C. L.; deGroot, H.; Fontecave, M.; MacFarlane, D. R.; Hankamer, B.; Nocera, D. G.; Tiede, D. M.; Dau, H.; Hillier, W.; Wang, L.; Amal, R. Energy Environ. Sci. 2013, 6, 1074–1076.

(26) Faunce, T. A.; Lubitz, W.; Rutherford, A. W. B.; MacFarlane, D.; Moore, G. F.; Yang, P.; Nocera, D. G.; Moore, T. A.; Gregory, D. H.; Fukuzumi, S.; Yoon, K. B.; Armstrong, F. A.; Wasielewski, M. R.; Styring, S. Energy Environ. Sci. 2013, 6, 695–698.

(27) Cowan, A. J.; Durrant, J. R. Chem Soc Rev 2013, 42, 2281–2293.

(28) Tachibana, Y.; Vayssieres, L.; Durrant, J. R. Nature Photon 2012, 6, 511–518.

(29) Youngblood, W. J.; Lee, S.-H. A.; Maeda, K.; Mallouk, T. E. Acc. Chem. Res. 2009, 42, 1966–1973.

(30) Moore, G. F.; Blakemore, J. D.; Milot, R. L.; Hull, J. F.; Song, H.-E.; Cai, L.; Schmuttenmaer, C. A.; Crabtree, R. H.; Brudvig, G. W. Energy Environ. Sci. 2011, 4, 2389–2392.

(31) Grätzel, M. Nature 2001, 414, 338–344.

(32) Fry, A. J.; Fox, P. C. 1986, 42, 5255.

(33) Méndez-Hernández, D. D.; Tarakeshwar, P.; Gust, D.; Moore, T. A.; Moore, A. L.; Mujica, V. J Mol Model 2012, 19, 2845–2848.

(34) Davis, A. P.; Fry, A. J. J. Phys. Chem. A 2010, 114, 12299–12304.

(35) Reynolds, C. A.; King, P. M.; Richards, W. G. Nature 1988, 334, 80–82.

(36) Megiatto, J. D., Jr; Méndez-Hernández, D. D.; Tejeda-Ferrari, M. E.; Teillout, A.-L.; Llansola Portolés, M. J.; Kodis, G.; Poluektov, O. G.; Rajh, T.; Mujica, V.; Groy, T. L.; Gust, D.; Moore, T. A.; Moore, A. L. Nature Chem 2014.

(37) Faller, P.; Goussias, C.; Rutherford, A. W.; Un, S. Proc. Natl. Acad. Sci. U.S.A. 2003, 100, 8732–8735.

(38) Umena, Y.; Kawakami, K.; Shen, J.-R.; Kamiya, N. Nature 2011, 473, 55–60.

(39) Muthukumaran, K.; Loewe, R. S.; Ambroise, A.; Tamaru, S.-I.; Li, Q.; Mathur, G.; Bocian, D. F.; Misra, V.; Lindsey, J. S. J. Org. Chem. 2004, 69, 1444–1452.

(40) Megiatto, J. D.; Patterson, D.; Sherman, B. D.; Moore, T. A.; Gust, D.; Moore, A. L. Chem. Commun. 2012, 48, 4558.

(41) Moore, G. F.; Hambourger, M.; Gervaldo, M.; Poluektov, O. G.; Rajh, T.; Gust, D.; Moore, T. A.; Moore, A. L. J. Am. Chem. Soc. 2008, 130, 10466–10467.

(42) Moore, G. F.; Konezny, S. J.; Song, H.-E.; Milot, R. L.; Blakemore, J. D.; Lee, M. L.; Batista, V. S.; Schmuttenmaer, C. A.; Crabtree, R. H.; Brudvig, G. W. J. Phys. Chem. C 2012, 116, 4892–4902.

(43) Hagberg, D. P.; Marinado, T.; Karlsson, K. M.; Nonomura, K.; Qin, P.; Boschloo, G.; Brinck, T.; Hagfeldt, A.; Sun, L. J. Org. Chem. 2007, 72, 9550–9556.

(44) Hagberg, D. P.; Yum, J.-H.; Lee, H.; De Angelis, F.; Marinado, T.; Karlsson, K. M.; Humphry-Baker, R.; Sun, L.; Hagfeldt, A.; Grätzel, M.; Nazeeruddin, M. K. J. Am. Chem. Soc. 2008, 130, 6259–6266.

(45) Scharber, M. C.; Mühlbacher, D.; Koppe, M.; Denk, P.; Waldauf, C.; Heeger, A. J.; Brabec, C. J. Adv. Mater. 2006, 18, 789–794.

(46) Gust, D.; Moore, T. A.; Moore, A. L. Acc. Chem. Res. 2001, 34, 40–48.

(47) Lee, C.-W.; Lu, H.-P.; Lan, C.-M.; Huang, Y.-L.; Liang, Y.-R.; Yen, W.-N.; Liu, Y.-C.; Lin, Y.-S.; Diau, E. W.-G.; Yeh, C.-Y. Chem. Eur. J. 2009, 15, 1403–1412.

(48) Meisner, J. S.; Sedbrook, D. F.; Krikorian, M.; Chen, J.; Sattler, A.; Carnes, M. E.; Murray, C. B.; Steigerwald, M.; Nuckolls, C. Chem. Sci. 2012, 3, 1007–1014.

(49) Previtali, C. M. Pure and applied chemistry 1995, 67, 127–134.

(50) Lowe, J. P. Academic Press. 1993, 273–275.

(51) Maccoll, A. Nature 1949, 163, 178–179.

(52) Winget, P.; Weber, E. J.; Cramer, C. J.; Truhlar, D. G. Phys. Chem. Chem. Phys. 2000, 2, 1231–1239.

(53) Baik, M.-H.; Friesner, R. A. J. Phys. Chem. A 2002, 106, 7407–7412.

(54) Schmidt am Busch, M.; Knapp, E.-W. J. Am. Chem. Soc. 2005, 127, 15730–15737.

(55) Cardona, C. M.; Li, W.; Kaifer, A. E.; Stockdale, D.; Bazan, G. C. Adv. Mater. 2011, 23, 2367–2371.

(56) Speelman, A. L.; Gillmore, J. G. J. Phys. Chem. A 2008, 112, 5684–5690.

(57) Lynch, E. J.; Speelman, A. L.; Curry, B. A.; Murillo, C. S.; Gillmore, J. G. J. Org. Chem. 2012, 77, 6423–6430.

(58) Frisch, M. J.; al, E. Gaussian 09, Revision A. 02 2009.

(59) Lee, C.; Yang, W.; Parr, R. G. Phys. Rev. B 1988, 37, 785–789.

(60) Becke, A. D. Phys. Rev. A 1988, 38, 3098–3100.

(61) Becke, A. D. J. Chem. Phys. 1996.

(62) Francl, M. M. J. Chem. Phys. 1982, 77, 3654–3665.

(63) Hariharan, P. C.; Pople, J. A. Theoret. Chim. Acta 1973, 28, 213–222.

(64) Rassolov, V. A.; Pople, J. A.; Ratner, M. A.; Windus, T. L. J. Chem. Phys. 1998, 109, 1223–1229.

(65) Evans, D. H. Chem. Rev. 2008, 108, 2113–2144.

(66) Konezny, S. J.; Doherty, M. D.; Luca, O. R.; Crabtree, R. H.; Soloveichik, G. L.; Batista, V. S. J. Phys. Chem. C 2012, 116, 6349–6356.

(67) Crespo-Hernández, C. E.; Close, D. M.; Gorb, L.; Leszczynski, J. J. Phys. Chem. B 2007, 111, 5386–5395.

(68) Arslan, T.; Kandemirli, F.; Ebenso, E. E.; Love, I.; Alemu, H. Corrosion Science 2009, 51, 35–47.

(69) Ma, R.; Guo, P.; Cui, H.; Zhang, X.; Nazeeruddin, M. K.; Grätzel, M. J. Phys.

Chem. A 2009, 113, 10119–10124.

(70) Olivares-Amaya, R.; Amador-Bedolla, C.; Hachmann, J.; Atahan-Evrenk, S.; Sánchez-Carrera, R. S.; Vogt, L.; Aspuru-Guzik, A. Energy Environ. Sci. 2011, 4, 4849.

(71) Roy, L. E.; Jakubikova, E.; Guthrie, M. G.; Batista, E. R. J. Phys. Chem. A 2009, 113, 6745–6750.

(72) Namazian, M.; Coote, M. L. J. Phys. Chem. A 2007, 111, 7227–7232.

(73) Shi, J.; Zhao, Y.-L.; Wang, H.-J.; Rui, L.; Guo, Q.-X. Journal of Molecular Structure: THEOCHEM 2009, 902, 66–71.

(74) Villegas, J. M.; Stoyanov, S. R.; Huang, W.; Rillema, D. P. Inorg Chem 2005, 44, 2297–2309.

(75) Tugsuz, T. J. Phys. Chem. B 2010, 114, 17092–17101.

(76) Koopmans, T. Physica 1934, 1, 104–113.

(77) Sereda, G.; Van Heukelom, J.; Koppang, M.; Ramreddy, S.; Collins, N. Beilstein J Org Chem 2006, 2, 26–26.

(78) Casado, J.; Ruiz Delgado, M. C.; Rey Merchán, M. C.; Hernández, V.; López Navarrete, J. T.; Pappenfus, T. M.; Williams, N.; Stegner, W. J.; Johnson, J. C.; Edlund, B. A.; Janzen, D. E.; Mann, K. R.; Orduna, J.; Villacampa, B. Chem. Eur. J. 2006, 12, 5458–5470.

(79) Jameh-Bozorghi, S.; Mansouri, A.; Dadpou, B. Int J Electrochem … 2010, 5, 867–879.

(80) Kuhn, A.; Eschwege, Von, K. G.; Conradie, J. Electrochimica Acta 2011, 56, 6211–6218.

(81) Eschwege, Von, K. G.; Conradie, J. South African Journal of … 2011, 64, 203–209.

(82) Koper, C.; Sarobe, M.; Jenneskens, L. W. Phys. Chem. Chem. Phys. 2004, 6, 319–327.

(83) Okazaki, S.; Oyarna, M.; Nomura, S. Electroanalysis 1997, 9, 1242–1246.

(84) Donzello, M. P.; Ercolani, C.; Kadish, K. M.; Ricciardi, G.; Rosa, A.; Stuzhin, P. A. Inorg Chem 2007, 46, 4145–4157.

(85) Suzuki, T.; Maruyama, Y.; Akasaka, T. Journal of the … 1994, 116, 1359–1363.

(86) Kumar, M.; Galezowski, W.; Kozlowski, P. M. Int. J. Quantum Chem. 2012, 113, 479–488.

(87) Xue, Z. M.; Liu, B.; Chen, C. H. Electrochimica Acta 2006, 51, 4554–4561.

(88) Morvillo, P. Solar Energy Materials and Solar Cells 2009, 93, 1827–1832.

(89) Seto, K.; Nakayama, T.; Uno, B. J. Phys. Chem. B 2013, 117, 10834–10845.

(90) Kawakami, Y.; Hopfinger, A. J. Chem. Res. Toxicol. 1990, 3, 244–247.

(91) Li, X.-L.; Fu, Y. Journal of Molecular Structure: THEOCHEM 2008, 856, 112–118.

(92) Hernández, L. I.; Godin, R.; Bergkamp, J. J.; Llansola Portolés, M. J.; Sherman, B. D.; Tomlin, J.; Kodis, G.; Méndez-Hernández, D. D.; Bertolotti, S.; Chesta, C. A.; Mariño-Ochoa, E.; Moore, A. L.; Moore, T. A.; Cosa, G.; Palacios, R. E. J. Phys. Chem. B 2013, 117, 4568–4581.

(93) Becke, A. D. J. Chem. Phys. 1993, 98, 5648.

(94) Hariharan, P. C.; Pople, J. A. Chemical Physics Letters 1972, 16, 217–219.

(95) Stewart, J. J. P. J. Comput. Chem. 1989, 10, 209–220.

(96) Stewart, J. J. P. J. Comput. Chem. 1989, 10, 221–264.

(97) Stewart, J. J. P. J Mol Model 2007, 13, 1173–1213.

(98) Barone, V.; Cossi, M. J. Phys. Chem. A 1998, 102, 1995–2001.

(99) Cossi, M.; Rega, N.; Scalmani, G.; Barone, V. J. Comput. Chem. 2003, 24, 669–681.

(100) Babcock, G. T.; Barry, B. A.; Debus, R. J.; Hoganson, C. W.; Atamian, M.; McIntosh, L.; Sithole, I.; Yocum, C. F. Biochemistry 1989, 28, 9557–9565.

(101) Zouni, A.; Jordan, R.; Schlodder, E.; Fromme, P.; Witt, H. T. Biochim. Biophys. Acta 2000, 1457, 103–105.

(102) Barry, B. A.; Babcock, G. T. Proc. Natl. Acad. Sci. U.S.A. 1987, 84, 7099–7103.

(103) Mamedov, F.; Sayre, R. T.; Styring, S. Biochemistry 1998, 37, 14245–14256.

(104) Hays, A. M.; Vassiliev, I. R.; Golbeck, J. H.; Debus, R. J. Biochemistry 1998, 37, 11352–11365.

(105) Meyer, T. J.; Huynh, M. H. V.; Thorp, H. H. Angew. Chem. Int. Ed. 2007, 46, 5284–5304.

(106) Barry, B. A. J. Photochem. Photobiol. B, Biol. 2011, 104, 60–71.

(107) Hammarström, L.; Styring, S. Energy Environ. Sci. 2011, 4, 2379.

(108) Styring, S.; Sjöholm, J.; Mamedov, F. Biochim. Biophys. Acta 2012, 1817, 76–87.

(109) Faller, P.; Debus, R. J.; Brettel, K.; Sugiura, M.; Rutherford, A. W.; Boussac, A. Proc. Natl. Acad. Sci. U.S.A. 2001, 98, 14368–14373.

(110) Rappaport, F.; Boussac, A.; Force, D. A.; Peloquin, J.; Brynda, M.; Sugiura, M.; Un, S.; Britt, R. D.; Diner, B. A. J. Am. Chem. Soc. 2009, 131, 4425–4433.

(111) Stubbe, J.; van der Donk, W. A. Chem. Rev. 1998, 98, 705–762.

(112) Faller, P.; Rutherford, A. W.; Debus, R. J. Biochemistry 2002, 41, 12914–12920.

(113) Gust, D.; Moore, T. A.; Moore, A. L. Faraday Discuss. 2012, 155, 9–26–discussion103–14.

(114) Gust, D.; Moore, T. A.; Moore, A. L. Acc. Chem. Res. 1993, 26, 198–205.

(115) Megiatto, J. D.; Antoniuk-Pablant, A.; Sherman, B. D.; Kodis, G.; Gervaldo, M.; Moore, T. A.; Moore, A. L.; Gust, D. Proc. Natl. Acad. Sci. U.S.A. 2012, 109, 15578–15583.

(116) Rajh, T.; Nedeljkovic, J. M.; Chen, L. X.; Poluektov, O.; Thurnauer, M. C. J. Phys. Chem. B 1999, 103, 3515–3519.

(117) Stone, A. J. Molecular Physics 1963, 6, 509–515.

(118) Smirnova, T. I.; Smirnov, A. I.; Paschenko, S. V.; Poluektov, O. G. J. Am. Chem. Soc. 2007, 129, 3476–3477.

(119) Orio, M.; Jarjayes, O.; Baptiste, B.; Philouze, C.; Duboc, C.; Mathias, J.-L.; Benisvy, L.; Thomas, F. Chem. Eur. J. 2012, 18, 5416–5429.

(120) Thomas, F.; Jarjayes, O.; Jamet, H.; Hamman, S.; Saint-Aman, E.; Duboc, C.; Pierre, J.-L. Angew. Chem. Int. Ed. Engl. 2004, 43, 594–597.

(121) Benisvy, L.; Bittl, R.; Bothe, E.; Garner, C. D.; McMaster, J.; Ross, S.; Teutloff, C.; Neese, F. Angew. Chem. Int. Ed. Engl. 2005, 44, 5314–5317.

(122) Un, S.; Atta, M.; Fontecave, M.; Rutherford, A. W. J. Am. Chem. Soc. 1995, 117, 10713–10719.

(123) Un, S.; Gerez, C.; Elleingand, E.; Fontecave, M. J. Am. Chem. Soc. 2001, 123, 3048–3054.

(124) Saito, K.; Shen, J.-R.; Ishida, T.; Ishikita, H. Biochemistry 2011, 50, 9836–9844.

(125) Sibert, R.; Josowicz, M.; Porcelli, F.; Veglia, G.; Range, K.; Barry, B. A. J. Am. Chem. Soc. 2007, 129, 4393–4400.

(126) Markle, T. F.; Rhile, I. J.; Dipasquale, A. G.; Mayer, J. M. Proc. Natl. Acad. Sci. U.S.A. 2008, 105, 8185–8190.

(127) Costentin, C.; Robert, M.; Savéant, J.-M. J. Am. Chem. Soc. 2006, 128, 8726–8727.

(128) Fecenko, C. J.; Thorp, H. H.; Meyer, T. J. J. Am. Chem. Soc. 2007, 129, 15098–15099.

(129) Hammes-Schiffer, S. Acc. Chem. Res. 2009, 42, 1881–1889.

(130) Perrin, C. L.; Nielson, J. B. Annu. Rev. Phys. Chem. 1997, 48, 511–544.

(131) Nurminen, E. J.; Mattinen, J. K.; LÃ nnberg, H. J. Chem. Soc., Perkin Trans. 2 2001, 2159–2165.

(132) Moore, G. F.; Hambourger, M.; Kodis, G.; Michl, W.; Gust, D.; Moore, T. A.; Moore, A. L. J. Phys. Chem. B 2010, 114, 14450–14457.

(133) Edwards, S. J.; Soudackov, A. V.; Hammes-Schiffer, S. J. Phys. Chem. A 2009, 113, 2117–2126.

(134) Witwicki, M.; Jezierska, J. Chemical Physics Letters 2010, 493, 364–370.

(135) Witwicki, M.; Jezierska, J.; Ozarowski, A. Chemical Physics Letters 2009, 473, 160–166.

(136) Barry, B. A.; Chen, J.; Keough, J.; Jenson, D.; Offenbacher, A.; Pagba, C. J.

Phys. Chem. Lett. 2012, 3, 543–554.

(137) Jenson, D. L.; Barry, B. A. J. Am. Chem. Soc. 2009, 131, 10567–10573.

(138) Chatterjee, R.; Coates, C. S.; Milikisiyants, S.; Lee, C.-I.; Wagner, A.; Poluektov, O. G.; Lakshmi, K. V. Biochemistry 2013, 52, 4781–4790.

(139) Rajh, T.; Ostafin, A. E.; Micic, O. I.; Tiede, D. M.; Thurnauer, M. C. J. Phys. Chem. 1996, 100, 4538–4545.

(140) Lakshmi, K. V.; Reifler, M. J.; Brudvig, G. W.; Poluektov, O. G.; Wagner, A. M.; Thurnauer, M. C. J. Phys. Chem. B 2000, 104, 10445–10448.

(141) Neese, F. … -Planck Institut für Bioanorganische Chemie: Mülheim 2004.

(142) Chong, D. P. Recent Advances in Density Functional Methods; World Scientific, 1997.

(143) Klamt, A.; Sch rmann, G. J. Chem. Soc., Perkin Trans. 2 1993, 799–805.